Digital Quantum Simulation of Quantum Many-Body Systems

Thesis by

Shi-Ning Sun

In Partial Fulfillment of the Requirements for the
Degree of
Doctor of Philosophy

CALIFORNIA INSTITUTE OF TECHNOLOGY
Pasadena, California

2024
Defended March 6, 2024

Shi-Ning Sun
ORCID: 0000-0002-5984-780X

ACKNOWLEDGEMENTS

It has been over five and a half years since I first arrived on Caltech campus as a graduate student. I still remember the day, July 5, 2018, when the intense heat and scorching sun, unusually harsh even for a Southern California summer, gave me the first taste of the place I would be living and studying in for the coming years. Five and a half years later, as the magnolia trees start blooming, signaling the end of a rainy winter season, I am preparing to graduate from my PhD and embark on a new adventure in the technology industry in the San Francisco Bay Area. Looking back, I cannot imagine completing this challenging and arduous intellectual journey without the support I received along the way.

I would like to start by thanking my advisor, Professor Austin J. Minnich, for his support and guidance throughout this journey. During the summer of 2019, when I was still looking for a research group, he was the one who encouraged me to pursue the direction of quantum computing and officially accepted me into the group at the end of the summer. Over the years, he has provided me the resources, mentorship, and freedom for the pursuit of my research. I am profoundly thankful for these opportunities, as this unique combination of guidance and independence I have experienced may be hard to find elsewhere.

My sincerest appreciation goes to Professor Garnet Kin-Lic Chan, Professor Andrei Faraon and Professor Xie Chen for serving on my PhD thesis committee as well as my candidacy committee three years ago. Their combined expertise in quantum chemistry, quantum engineering and condensed matter physics virtually covers all aspects of my thesis. I must particularly express my gratitude to Professor Garnet Chan, whose research group was the original reason I came to this institution. Although my rotation in his group did not proceed as expected, I am deeply grateful for what I learned from his technical expertise and fortunate enough to collaborate with his group on a few works subsequently.

My heartfelt appreciation extends to my research collaborators, whose effort and dedication have significantly enriched this thesis. First of all, I am grateful to Dr. Mario Motta for introducing me to the quantum imaginary time evolution algorithm he originally developed. I can still remember those two-hour long video calls during Covid where he mentored me through the technical details I need for my first PhD project. Secondly, I would like to thank Brian Marinelli's unrelenting efforts

in working on the quantum hardware at Berkeley. His dedication to calibrating the quantum device we used to run our experiment was what brought our work to fruition. I would also like to thank my other research collaborators: Dr. Jong Yeon Lee, Dr. Adrian Teck Keng Tan, Dr. Ruslan Tazhigulov, Dr. Peishi Cheng, Dr. Hirsh Kamakari, and Jin Ming Koh. Without their help, I would not have learned and explored so much during my PhD.

Throughout my time at Caltech, I have been involved in various communities, even though the advent of Covid has certainly added a challenging dimension to this aspect of my graduate school experience. All along the way were my group colleagues. I would like to mention Adrian Tan again, with whom I shared many academic and personal interests, for our friendship and his constant encouragement. I would also like to thank my office mates Nachiket Naik, Tomi Esho and Hirsh Kamakari for making B151 a lively place to work in and exchange ideas. Outside my research group, I would like to thank the Caltech Korean Graduate Student Association, especially Gunho Kim, who first introduced me into the community, and Sujin Kim, who helped me with my Korean speaking when I was barely able to make a conversation. I also appreciate the personal conversations with many other friends in the Korean student community, including Sanghyun Yi, Jihoon Ahn, Soonho Kwon, Gihwan Kim, Hyunjin Kim, Jihong Min, Jin Mo Koo, Yae-Chan Lim and Hyeoksu Lee. I would also like to thank friends from the badminton community for all the fun badminton games and hangouts, especially Jim Zhang, Masami Hazu, and Forte Shinko. Additionally, I appreciate all those nights spent in Gates-Thomas grinding through the spreadsheet engine with Carter Cocke and Victor Zendejas Lopez.

I express my sincere gratitude to the friends that are now in the vibrant technology community in the Bay Area, who have been instrumental in shaping my career path. Special thanks to Yang Gao, He Ma, Tomoyuki Oniyama, and Yalu Chen for their invaluable career advice when I barely had any idea on what career path to take. I am also appreciative of the friendships formed within the Chinese and Japanese student communities at Caltech that have transcended our academic years into our career years, in particular the friendships with Lue (Leo) Wu, Cheng Shen, Michelle Chan-Mei Shao, and Kai Matsuka. Additionally, I extend my thanks to Peter Zu and Mei Gong, whose wisdom and insights have not only enriched my professional pursuits but also fostered a broader perspective on life and career. There are other connections and friendships I made in the Bay Area toward the end of my PhD who

have helped me in the transition from academia to industry, both professionally and personally. Even though I am not mentioning them here, I would like to express my gratitude and certainly look forward to deepening our relations in the coming years.

I extend my heartfelt gratitude to the friends who I met before my PhD but have nonetheless been a vital part of this journey. Special thanks to Hiroki Fukuda for the joyous reunions twice in Japan and twice in Los Angeles; to Dae Heun Koh, whose shared experiences with me since our UChicago days have sparked so many interesting conversations; to Yunbo (Robert) Chen, for easing my uncertainty about navigating my first industry internship; to Cheuk To Tsui, for letting me stay in his apartment at Stanford even after I stayed in his apartment so many times back in Chicago; to Sifei Chen for spending time together around Peking University while reminiscing about our childhood memories. I was also fortunate to reunion with Kevin Cheng, Steven Ren and Edward Huh from the Asian American Intervarsity community at UChicago. These friendships, spanning continents and years, reminded me that the bonds of friendship are a timeless treasure even when we are on completely different paths in our lives.

Finally, I extend my deepest gratitude to my parents, whose unwavering support has profoundly shaped both my personal character and my academic pursuits. My father, Hao Sun, a distinguished Ph.D. himself, has always been an intellectual inspiration to me. Despite the limited time spent with him while growing up, his scholarly achievements have consistently motivated me to strive for excellence in my own intellectual journey. Lastly, I would like to honor the person to whom I am most grateful in my life: my mother, Jinghua Xu, whose resilience, stamina, and unyielding work ethic have been a guiding force for my own personality, ultimately giving me the strength to face any challenges in this intellectual journey. During times of difficulty, her voice at the other end of the phone has always been a source of solace. Without either of them, I could not have become the person I am today.

ABSTRACT

Quantum computing has emerged as a promising technology, heralding a new era of computational capabilities, with the simulation of quantum many-body systems as one of its primary objectives. Although fault-tolerant quantum computers are still years away, noisy intermediate-scale quantum (NISQ) devices have been fabricated and leveraged to perform small-scale quantum simulations. In this thesis, we demonstrate simulations of quantum many-body systems on these near-term quantum computers. We specifically focus on physical quantities pertaining to the linear-response framework, which include two-point correlation functions and Green's functions, of small-scale spin and molecular models. Additionally, as quantum hardware increases in qubit count, simulation of these quantum algorithms on classical computers that closely resemble those planned for execution on quantum hardware becomes increasingly critical. The final part of this thesis examines such a simulation using tensor network algorithms on classical computers.

We first present the study of finite-temperature physics of spin models on quantum hardware. Employing the quantum imaginary time evolution (QITE) algorithm, we demonstrate the computation of diverse finite-temperature observables, including energy, static and dynamical correlation functions, and excitation spectra of the Heisenberg model and the transverse-field Ising model of up to four sites on five-qubit IBM Quantum devices. Accurate determination of these finite-temperature properties on quantum computers is made possible by several algorithmic improvements, including a method to exploit symmetries that reduces the quantum resources required by QITE, circuit optimization procedures to reduce circuit depth, and error-mitigation techniques to improve the quality of raw hardware data. This work demonstrates that the ansatz-independent QITE algorithm is capable of computing diverse finite-temperature observables on near-term quantum devices.

The second work implements an algorithm for frequency-domain response properties of diatomic molecules using a novel high-fidelity three-qubit iToffoli gate. Although it is natural to compute response properties in the time domain due to the natural ability of quantum computers to apply unitary time evolutions, obtaining the frequency-domain properties from the time-domain properties typically requires a time duration that results in quantum circuits exceeding the circuit depth limitations of near-term quantum computers. In this work, we carry out computations of the response properties directly in the frequency domain using the linear combination

of unitaries (LCU) algorithm. Execution of the LCU-based protocol on quantum hardware is enabled by the iToffoli gate, which enables a $\sim 50\%$ reduction in circuit depth and $\sim 40\%$ reduction in circuit execution time in the LCU circuits compared to the traditional gate set. We show that the molecular properties obtained with the iToffoli gate exhibit comparable or better agreement with analytical results than those obtained when CZ gates are the only multi-qubit gates. This work is among the first demonstrations of the practical usage of a native multi-qubit gate in quantum simulation, with diverse potential applications to near-term quantum computation.

Finally, this thesis conducts a tensor network simulation of measurement-induced state preparation on classical computers. Specifically, we simulate the phase transition in random-bond Ising models (RBIM) by performing measurements on the cluster states. The simulation is carried out on NVIDIA H100 graphical processing units (GPUs) using the cuQuantum library. We present simulation of correlation functions in one dimension (1D) and ferromagnetic susceptibilities in two dimensions (2D), observing a phase transition from the ferromagnetic phase to spin-glass phase in the 2D model. The tensor network simulation incorporates up to 176 qubits on the 2D lattice. This work paves the way for future explorations of tensor network simulations of measurement-induced quantum computation protocols with GPU-accelerated tensor network libraries.

PUBLISHED CONTENT AND CONTRIBUTIONS

[1]S.-N. Sun, B. Marinelli, J. M. Koh, Y. Kim, L. B. Nguyen, L. Chen, J. M. Kreikebaum, D. I. Santiago, I. Siddiqi, and A. J. Minnich, "Quantum computation of frequency-domain molecular response properties using a three-qubit iToffoli gate", npj Quantum Inf. **10**, 55 (2024),
Contribution: S.N.S. conceptualized the project, contributed to the codebase used for running experiments and analyzing data. S.N.S. wrote the theoretical portion of the paper.

[2]J. M. Koh, S.-N. Sun, M. Motta, and A. J. Minnich, "Measurement-induced entanglement phase transition on a superconducting quantum processor with mid-circuit readout", Nat. Phys. **19**, 1314–1319 (2023),
Contribution: S.N.S. contributed to conceptualizing the project.

[3]A. T. K. Tan, S.-N. Sun, R. N. Tazhigulov, G. K.-L. Chan, and A. J. Minnich, "Realizing symmetry-protected topological phases in a spin-1/2 chain with next-nearest-neighbor hopping on superconducting qubits", Phys. Rev. A **107**, 032614 (2023),
Contribution: S.N.S. contributed to the codebase in the initial phase of the work.

[4]P. S. Cheng, J. Sun, S.-N. Sun, A. Y. Choi, and A. J. Minnich, "High-field transport and hot-electron noise in gaas from first-principles calculations: role of two-phonon scattering", Phys. Rev. B **106**, 245201 (2022),
Contribution: S.N.S. contributed to the codebase and discussion for analyzing effects of two-phonon scattering.

[5]H. Kamakari, S.-N. Sun, M. Motta, and A. J. Minnich, "Digital quantum simulation of open quantum systems using quantum imaginary–time evolution", PRX Quantum **3**, 010320 (2022),
Contribution: S.N.S. implemented the code to perform real time and imaginary time evolutions simultaneously.

[6]R. N. Tazhigulov, S.-N. Sun, R. Haghshenas, H. Zhai, A. T. Tan, N. C. Rubin, R. Babbush, A. J. Minnich, and G. K.-L. Chan, "Simulating Models of Challenging Correlated Molecules and Materials on the Sycamore Quantum Processor", PRX Quantum **3**, 040318 (2022),
Contribution: S.N.S. contributed to the codebase in the initial phase of the work.

[7]S.-N. Sun, M. Motta, R. N. Tazhigulov, A. T. Tan, G. K.-L. Chan, and A. J. Minnich, "Quantum Computation of Finite-Temperature Static and Dynamical Properties of Spin Systems Using Quantum Imaginary Time Evolution", PRX Quantum **2**, 010317 (2021),
Contribution: S.N.S. conceptualized the project, implemented the algorithm on quantum computers and performed data analysis. S.N.S. wrote the paper.

TABLE OF CONTENTS

LIST OF ILLUSTRATIONS

Number *Page*

LIST OF TABLES

Chapter 1

INTRODUCTION

Quantum computers have emerged as a promising technology, undergoing a significant transformation over the past decade. Although quantum computers were originally proposed in 1982 as a tool to simulate quantum systems [1], the landscape of quantum computing has witnessed remarkable progress in hardware development [2, 3], algorithmic advancements [4, 5], and practical applications [6] during this timeframe. Quantum hardware based on various platforms has been developed, including superconducting circuits [2], ion traps [3], and neutral atoms [7]. On the application side, quantum computers have been employed to simulate complex quantum systems [8], optimize combinatorial problems [9], and solve certain mathematical equations [10]. Another significant advancement is in the simulation of quantum computers using classical computers, especially through the utilization of tensor networks [11], enabling researchers to model and analyze quantum algorithms more efficiently [12]. This multifaceted progress underscores the growing potential and versatility of quantum computing across both theoretical and practical domains.

One of the main applications of quantum computers is to simulate quantum many-body systems, which are physical systems composed of a large number of interacting particles [13]. These systems have been the subjects of study in various fields, such as condensed matter physics, materials science and quantum chemistry. Quantum computers provide a unique approach of investigating the complex physical phenomena in these systems without the exponential resource requirement to represent quantum many-body systems on classical computers. In particular, this thesis focuses on simulating the quantities encountered in the linear-response framework, including two-point correlation functions and Green's functions [14]. The foundation of computing such physical quantities on quantum computers has been developed in the early 2000s [15, 16], but not until recently have quantum computers reached the ability of executing these circuits with adequate fidelities.

The first work in this thesis is the computation of finite-temperature static and dynamical properties of spin systems. We use the quantum imaginary time evolution (QITE) algorithm [17] to simulate the effect of finite temperature, and obtain the

energy, static and dynamic correlation functions, and excitation spectra of Heisenberg models and transverse-field Ising models on up to five qubits on IBM Quantum devices. The excessive quantum resources required in the original QITE algorithm are reduced by exploiting symmetry using the stabilizer formalism in quantum error correction [18], so that the circuits are within the constraints of near-term quantum devices. Various error mitigation techniques, including post-selection, readout error mitigation and phase-and-scale correction are exploited to improve the quality of the raw experimental data. This work demonstrates that computing finite-temperature observables of few-qubit spin models is achievable on current quantum devices with the efficient use of quantum resources and error mitigation.

The second work explores using a novel three-qubit iToffoli gate [19] to compute molecular Green's functions. The quantum simulation experiments, along with the implementation of the iToffoli gate, are performed on a superconducting quantum processor hosted at University of California, Berkeley. We use the iToffoli gate to reduce the depths of the circuits in the linear combination of unitaries (LCU) framework [20] used to calculate Green's functions on quantum computers [21, 22]. The molecular models are diatomic molecules in minimal basis with only highest occupied molecular orbital (HOMO) and lowest unoccupied molecular orbital (LUMO) so that the quantum circuits fit into the quantum resource constraints of the quantum devices. The observables computed directly from the quantum circuits are the transition amplitudes between the ground state and N- or $(N \pm 1)$-electron excited states, which are then combined with ground- and excited-state energies to obtain frequency-domain Green's functions and response functions. Two particular error mitigation techniques, randomized compiling and McWeeny purification, are applied to the circuit construction and data postprocessing stages respectively and exhibit significant improvements in the physical observables of the molecular models.

The last contribution of this thesis is the simulation of properties of 1D and 2D random-bond Ising models (RBIMs) using a measurement-based state preparation protocol. The protocol, originally developed in ref. [23], prepares a cluster state on a Lieb lattice and obtains the phase transition properties of RBIMs through measurement and decoding. Specifically, the lattice is divided into two sublattices, which are odd and even sublattices in 1D, and vertex and edge sublattices in 2D. In 1D, we study the correlation function $\langle Z_1 Z_{2n+1} \rangle$ on the odd sublattice, extract the correlation length from the correlation functions and compare it to the exact result

in the thermodynamic limit. In 2D, we compute the ferromagnetic susceptibility and observe a divergence of its variance at the measurement angle that corresponds to the phase transition temperature. This work uses the cuQuantum library [24] to carry out the tensor network simulation on graphical processing units on up to 176 qubits, paving the way for larger-scale implementations of measurement-based quantum computing protocols with tensor network methods.

This organization of this thesis unfolds as follows. The initial segment, spanning Chapters 2 to 4, delves into foundational knowledge of the research contents. Chapter 2 elucidates the fundamentals of quantum computation, encompassing definitions of quantum gates, measurements, and essential techniques used in practical implementations of quantum circuits on quantum hardware; Chapter 3 navigates through the components of quantum information that are relevant to this thesis, including stabilizer formalism in quantum error correction, noise in quantum hardware, and metrics for entanglement in quantum states; Chapter 4 focuses on the target of quantum simulation: quantum many-body systems, including spin systems and molecular systems. The latter portion of this thesis embarks on an exploration of my original research contributions. Chapter 5 explores the computation of finite-temperature static and dynamical properties of spin models using the QITE algorithm; Chapter 6 elaborates on the computation of frequency-domain Green's function of molecular models using the LCU algorithm; Chapter 7 focuses on large-scale classical simulations of the properties of RBIMs by measurements on the cluster states. At the end, Chapter 8 concludes this thesis by presenting outlook for future exploration in the dynamic field of quantum computing especially pertaining to quantum simulation.

Chapter 2

QUANTUM COMPUTATION

This chapter introduces concepts from quantum computation that are relevant to the contents of this thesis. We start by reviewing quantum gates, followed by quantum measurements, and lastly special quantum circuits used in quantum simulation experiments. In Sec. 2.1, we review in the order of single-qubit gates, two-qubit gates, and multi-qubit gates. Special gates like parameterized gates and Clifford gates will be introduced in the specific subsections corresponding to the number of qubits they act on. Section 2.2 is on quantum measurements, where we first introduce the positive operator-valued measure (POVM) measurement formalism and then move on to reduced density matrices. Section 2.3 is on special quantum circuits for quantum simulation, including circuits relevant to quantum simulation and to quantum measurements. Throughout this chapter, we also introduce certain platform-dependent gates, specifically gates on the devices at IBM Quantum and Google Quantum AI.

2.1 Quantum Gates

Single-Qubit Gates

Pauli Gates

The single-qubit Pauli gates are

$$X = \begin{bmatrix} 0 & 1 \\ 1 & 0 \end{bmatrix}, \quad Y = \begin{bmatrix} 0 & -i \\ i & 0 \end{bmatrix}, \quad Z = \begin{bmatrix} 1 & 0 \\ 0 & -1 \end{bmatrix}. \tag{2.1}$$

Pauli Rotation Gates

Let $\hat{\mathbf{n}}$ be a unit vector. We have the identity

$$e^{i\theta(\hat{\mathbf{n}}\cdot\boldsymbol{\sigma})} = I\cos\theta + i(\hat{\mathbf{n}}\cdot\boldsymbol{\sigma})\sin\theta. \tag{2.2}$$

Rotation gates are defined by $R_{\hat{\mathbf{n}}}(\theta) = \exp(-iS_{\hat{\mathbf{n}}}\theta/\hbar) = \exp(-i\hat{\mathbf{n}}\cdot\boldsymbol{\sigma}\theta/2)$, so rota-

tions around x, y and z axes by angle θ are

$$R_x(\theta) = e^{-i\theta X/2} = \begin{bmatrix} \cos(\theta/2) & -i\sin(\theta/2) \\ -i\sin(\theta/2) & \cos(\theta/2) \end{bmatrix}, \tag{2.3}$$

$$R_y(\theta) = e^{-i\theta Y/2} = \begin{bmatrix} \cos(\theta/2) & -\sin(\theta/2) \\ \sin(\theta/2) & \cos(\theta/2) \end{bmatrix}, \tag{2.4}$$

$$R_z(\theta) = e^{-i\theta Z/2} = \begin{bmatrix} e^{-i\theta/2} & 0 \\ 0 & e^{i\theta/2} \end{bmatrix}. \tag{2.5}$$

Pauli rotation gates can also be thought of as powers of the Pauli gates. For example,

$$Z^r = e^{ir\log Z} = e^{ir\log Z} \sim e^{-ir\pi Z/2} = R_z(r\pi) \tag{2.6}$$

(where $\sim$ denotes equal up to a phase factor) since

$$\log Z = \begin{bmatrix} 0 & 0 \\ 0 & i\pi \end{bmatrix} \sim -i\frac{\pi}{2}Z \tag{2.7}$$

up to a constant. Note that here we need to make the choice that $\log(-1) = i\pi$. Since X and Y have the same eigenspectra as Z, similarly we have

$$X^r = R_x(r\pi), \tag{2.8}$$

$$Y^r = R_y(r\pi). \tag{2.9}$$

Clifford Gates

Other single-qubit gates that are Clifford gates, which convert Pauli gates to Pauli gates under conjugation, but are not included above are the Hadamard gate H and the phase gate S

$$H = \frac{1}{\sqrt{2}}\begin{bmatrix} 1 & 1 \\ 1 & -1 \end{bmatrix}, \tag{2.10}$$

$$S = \begin{bmatrix} 1 & 0 \\ 0 & i \end{bmatrix} \tag{2.11}$$

Note that $S \sim R_z(\pi/2)$. These gates can be verified to satisfy the Clifford property because they satisfy the relations [18]

$$HXH^\dagger = Z, \quad HYH^\dagger = -Y, \quad HZH^\dagger = X,$$
$$SXS^\dagger = Y, \quad SYS^\dagger = -X, \quad SZS^\dagger = Z.$$

Parameterized Single-Qubit Gates

An arbitrary single-qubit gate can be parameterized by three parameters. The exact form of the parameterization is platform-dependent.

In the architecture of IBM Quantum devices, the U_3 gate is the arbitrary parameterized single-qubit gate [25], which is defined as

$$U_3(\theta, \phi, \lambda) = R_z(\phi) R_y(\theta) R_z(\lambda). \tag{2.12}$$

In matrix notation,

$$U_3(\theta, \phi, \lambda) = \begin{bmatrix} \cos(\theta/2) & -e^{i\lambda} \sin(\theta/2) \\ e^{i\phi} \sin(\theta/2) & e^{i(\phi+\lambda)} \cos(\theta/2) \end{bmatrix} \tag{2.13}$$

By Ref. [26], the U_3 gate can be implemented with two $X_{\pi/2}$ pulses and virtual Z gates by

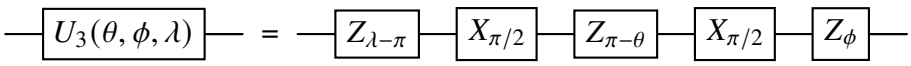

The two sides are equal up to a phase. (Note that the decomposition is different from Eq. (19) in Ref. [26] because the definition of the U_3 gate in Ref. [26] has $\pm i$ on the off-diagonal elements.)

Common single-qubit gates can be written in terms of U_3 gates in the form

$$\begin{aligned} R_x(\theta) &= U_3(\theta, -\pi/2, \pi/2), \\ R_y(\theta) &= U_3(\theta, 0, 0), \\ R_z(\theta) &= U_3(0, 0, \theta), \\ H &= U_3(\pi/2, 0, \pi), \\ S &= U_3(0, 0, \pi/2). \end{aligned}$$

On Google's devices, the PhasedXZ gate is the parameterized arbitrary single-qubit gate [27], which is defined as

$$\text{PhasedXZ}(a, x, z) = Z^{z+a} X^x Z^{-a}. \tag{2.14}$$

In rotation-gate notation, $\text{PhasedXZ}(a, x, z) \sim R_z((z + a)\pi) R_x(x\pi) R_z(-a\pi)$.

Two-Qubit Gates

Standard Gates

A CNOT gate with the first qubit as the control qubit and the second qubit as the target qubit can be expressed as CNOT = $|0\rangle\langle 0| \otimes I + |1\rangle\langle 1| \otimes X$. In matrix notation,

$$\text{CNOT} = \begin{bmatrix} 1 & 0 & 0 & 0 \\ 0 & 1 & 0 & 0 \\ 0 & 0 & 0 & 1 \\ 0 & 0 & 1 & 0 \end{bmatrix}. \tag{2.15}$$

A CZ gate with the first qubit as the control qubit and the second qubit as the target qubit can be expressed as CZ = $|0\rangle\langle 0| \otimes I + |1\rangle\langle 1| \otimes Z$. In matrix notation,

$$\text{CZ} = \begin{bmatrix} 1 & 0 & 0 & 0 \\ 0 & 1 & 0 & 0 \\ 0 & 0 & 1 & 0 \\ 0 & 0 & 0 & -1 \end{bmatrix}. \tag{2.16}$$

A SWAP gate swaps two qubits. In matrix notation,

$$\text{SWAP} = \begin{bmatrix} 1 & 0 & 0 & 0 \\ 0 & 0 & 1 & 0 \\ 0 & 1 & 0 & 0 \\ 0 & 0 & 0 & 1 \end{bmatrix}. \tag{2.17}$$

An iSWAP gate swaps two qubits and adds a phase factor i. In matrix notation,

$$\text{iSWAP} = \begin{bmatrix} 1 & 0 & 0 & 0 \\ 0 & 0 & i & 0 \\ 0 & i & 0 & 0 \\ 0 & 0 & 0 & 1 \end{bmatrix}. \tag{2.18}$$

Fermionic Simulation Gate

Two-qubit gates native to Google's devices include the Sycamore gate, $\sqrt{\text{iSWAP}}$ and CZ. Both the Sycamore gate and $\sqrt{\text{iSWAP}}$ are derived from the two-parameter

fermionic simulation gate [28]

$$\mathrm{FSim}(\theta,\phi) = e^{-i\theta(X\otimes X+Y\otimes Y)/2}e^{-i\phi(I-Z)\otimes(I-Z)/4} = \begin{bmatrix} 1 & 0 & 0 & 0 \\ 0 & \cos\theta & -i\sin\theta & 0 \\ 0 & -i\sin\theta & \cos\theta & 0 \\ 0 & 0 & 0 & e^{-i\phi} \end{bmatrix}. \tag{2.19}$$

where θ is the iSWAP angle and ϕ is the controlled-phase angle.

Two main pre-calibrated gates derived out of the FSim gate are the sycamore gate Syc and the square root iSWAP gate $\sqrt{\mathrm{iswap}}$. The Sycamore gate Syc has the expression

$$\mathrm{Syc} = \mathrm{FSim}(\pi/2,\pi/6) = \begin{bmatrix} 1 & 0 & 0 & 0 \\ 0 & 0 & -i & 0 \\ 0 & -i & 0 & 0 \\ 0 & 0 & 0 & e^{-i\pi/6} \end{bmatrix}. \tag{2.20}$$

The square root iSWAP gate $\sqrt{\mathrm{iSWAP}}$ has the expression

$$\sqrt{\mathrm{iSWAP}} = \mathrm{FSim}(-\pi/4,0) = \begin{bmatrix} 1 & 0 & 0 & 0 \\ 0 & 1/\sqrt{2} & i/\sqrt{2} & 0 \\ 0 & i/\sqrt{2} & 1/\sqrt{2} & 0 \\ 0 & 0 & 0 & 1 \end{bmatrix}. \tag{2.21}$$

2.2 Quantum Measurements

Measurement

Quantum measurements are described by a set of measurement operators $\{M_m\}$ that satisfy the completeness relation:

$$\sum_m M_m^\dagger M_m = I. \tag{2.22}$$

Suppose the state is described by a state vector $|\psi\rangle$ or a density matrix ρ. The probability of obtaining the measurement outcome m is

$$\text{state vector:} \quad p_m = \langle\psi|M_m^\dagger M_m|\psi\rangle\,, \tag{2.23}$$

$$\text{density matrix:} \quad p_m = \mathrm{tr}\Big(M_m^\dagger M_m \rho\Big). \tag{2.24}$$

The state after obtaining the measurement outcome m is

$$\text{state vector:} \quad \frac{M_m |\psi\rangle}{\sqrt{\langle\psi|M_m^\dagger M_m|\psi\rangle}}, \tag{2.25}$$

$$\text{density matrix:} \quad \frac{M_m \rho M_m^\dagger}{\text{tr}\left(M_m^\dagger M_m \rho\right)}. \tag{2.26}$$

A special and perhaps the most common type of measurement is the projective (or von Neumann) measurement, where the measurement operators are orthogonal projectors so that they satisfy $M_m M_{m'} = M_m \delta_{m,m'}$. These orthogonal projectors usually arise from the eigenspaces of an observable, since an observable in quantum mechanics is a Hermitian operator and has orthogonal eigenspaces.

Reduced Density Matrix

A density matrix provides a description of the quantum system whose state is not completely known. Suppose a quantum system is in $|\psi_i\rangle$ with probability p_i.

$$\rho = \sum_i p_i |\psi_i\rangle\langle\psi_i| . \tag{2.27}$$

Alternatively, the density matrix can be interpreted as an ensemble of pure states, where the proportion of $|\psi\rangle$ in the ensemble is p_i. In statistics terms, the first interpretation corresponds to the Bayesian approach and the second interpretation corresponds to the frequentist approach.

Mathematically, a density matrix is defined as the following.

Definition. An operator ρ is associated with some ensemble $\{p_i, |\psi_i\rangle\}$ if and only if it satisfies

1. $\text{Tr}(\rho) = 1$.
2. ρ is positive.

To analyze composite quantum systems, we need the concept of reduced density operator, which is

$$\rho^A = \text{Tr}_B(\rho^{AB}). \tag{2.28}$$

The reduced density matrix has the operational meaning that when an observable only acts on a subsystem, its expectation value is given by the trace of the observable

times the reduced density matrix. Specifically, for an observable O_A that only acts on A, its expectation value on the system is

$$\langle O_A \rangle = \mathrm{Tr}_{AB}(O^A \rho^{AB}) = \mathrm{Tr}_A(O^A \rho^A). \tag{2.29}$$

Another situation where the reduced density matrix arises is when we measure a subsystem and discard the measurement result. In this case, the density matrix of the composite system is

$$\tilde{\rho}^{AB} = \sum_m M_m^B \rho^{AB} M_m^{B\dagger} \tag{2.30}$$

and the density matrix of the subsystem is

$$\tilde{\rho}^A = \mathrm{Tr}_B(\tilde{\rho}^{AB}) = \mathrm{Tr}_B\left(\sum_m M_m^B \rho^{AB} M_m^{B\dagger}\right) = \rho^A. \tag{2.31}$$

2.3 Quantum Circuits

Multi-Qubit Rotation Circuits

To apply a rotation operator of weight more than 1, we usually apply R_z on one of the qubits and use CNOT to extend the weight of the Pauli string. To transform Z to X and Y, one way is to use the Clifford gates H and S so that

$$X = HZH, \qquad \text{—}[H]\text{—}[Z]\text{—}[H]\text{—},$$

$$Y = SHZ(SH)^\dagger = SHZHS^\dagger, \qquad \text{—}[S^\dagger]\text{—}[H]\text{—}[Z]\text{—}[H]\text{—}[S]\text{—} \tag{2.32}$$

Another way is to use the rotation gates

$$X = R_y(\pi/2) Z R_y(-\pi/2), \quad \text{—}[R_y(\pi/2)]\text{—}[Z]\text{—}[R_y(-\pi/2)]\text{—}, \tag{2.33}$$

$$Y = R_x(-\pi/2) Z R_x(\pi/2), \quad \text{—}[R_x(-\pi/2)]\text{—}[Z]\text{—}[R_x(\pi/2)]\text{—}. \tag{2.34}$$

For example, if we want to apply the rotation gate $e^{-i\theta XYZ}$, we can apply the circuit

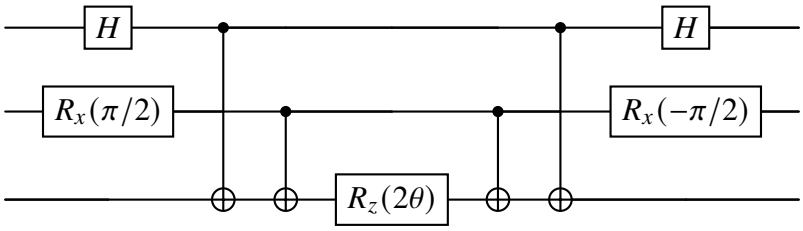

or

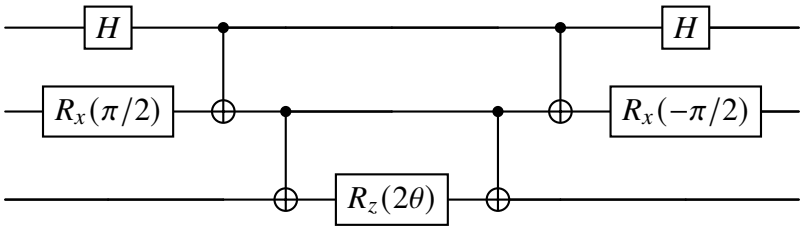

In practice the second circuit is better since we don't need SWAP gates to apply long-range CNOTs [29].

Measurement Circuits

Most quantum hardware can only measure in Z-basis. To measure in X-basis, we need to apply the Hadamard gate before the measurement gate,

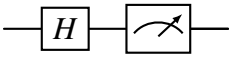

To measure in Y-basis, we need to apply $R_x(\pi/2)$ before the measurement gate,

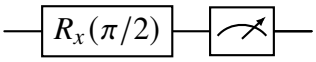

Alternatively, we can apply $S^\dagger$ followed by an H gate, which gives

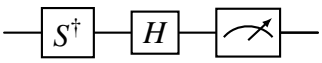

The latter method is used in the construction of tomography circuits in Qiskit.

We can understand measuring in a different basis as changing the stabilizer from X or Y to Z. For example, transforming $|+\rangle$ to $|0\rangle$ is the same as transforming the stabilizer from X to Z, which is achieved by H since $HXH = Z$. Transforming the state $|+\mathbf{y}\rangle$ to $|0\rangle$ is the same as transforming the stabilizer from Y to Z, which is achieved by $R_x(\pi/2)$ since $R_x(\pi/2)YR_x^\dagger(\pi/2) = Z$ or by $HS^\dagger$ since $HS^\dagger YSH = Z$.

Hadamard Test

Suppose we want to calculate time correlation functions of the form

$$C_{UV}(t) = \langle U(t)V \rangle = \langle e^{i\hat{H}t} U e^{-i\hat{H}t} V \rangle, \tag{2.35}$$

where U and V are unitary operators.

Consider the circuit [30, 31]

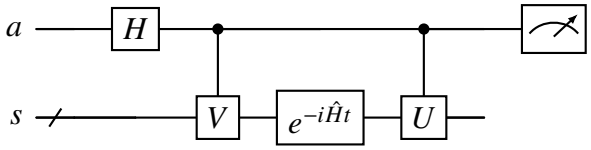

Here a denotes the ancilla qubit and s denotes the system qubits.

Claim 1. Measuring X on the ancilla yields the real part of $C_{UV}(t)$ and measuring Y on the ancilla yields the imaginary part of $C_{UV(t)}$, so that $C_{UV}(t) = \langle X \rangle + i \langle Y \rangle$.

Proof. To derive this result, let the control gates be

$$\tilde{U} = |0\rangle\langle 0| \otimes I_p + |1\rangle\langle 1| \otimes U, \tag{2.36}$$

$$\tilde{V} = |0\rangle\langle 0| \otimes I_p + |1\rangle\langle 1| \otimes V. \tag{2.37}$$

The density matrix after the circuit is

$$\tilde{U}(I_a \otimes e^{-i\hat{H}t})\tilde{V}(\rho_a \otimes \rho_s)\tilde{V}^\dagger(I_a \otimes e^{i\hat{H}t})\tilde{U}^\dagger, \tag{2.38}$$

where ρ_a is the ancilla density matrix after the Hadamard gate

$$\rho_a = \frac{1}{2}\begin{bmatrix} 1 & 1 \\ 1 & 1 \end{bmatrix}. \tag{2.39}$$

The expectation value of X is

$$\begin{aligned} \langle X \rangle &= \mathrm{Tr}\Big((|0\rangle\langle 1| \otimes I_p)\tilde{U}(I_a \otimes e^{-i\hat{H}t})\tilde{V}(\rho_a \otimes \rho_p)\tilde{V}^\dagger(I_a \otimes e^{i\hat{H}t})\tilde{U}^\dagger \Big) \\ &\quad + \mathrm{Tr}\Big((|1\rangle\langle 0| \otimes I_p)\tilde{U}(I_a \otimes e^{-i\hat{H}t})\tilde{V}(\rho_a \otimes \rho_p)\tilde{V}^\dagger(I_a \otimes e^{i\hat{H}t})\tilde{U}^\dagger \Big) \\ &= \frac{1}{2}\Big(\langle U(t)V \rangle + \langle V^\dagger U^\dagger(t) \rangle \Big) = \mathrm{Re}(\langle U(t)V \rangle) \end{aligned} \tag{2.40}$$

The expectation value of Y is

$$\begin{aligned}\langle Y\rangle &= -i\,\mathrm{Tr}\Big((|0\rangle\langle 1|\otimes I_p)\tilde{U}(I_a\otimes e^{-i\hat{H}t})\tilde{V}(\rho_a\otimes\rho_p)\tilde{V}^\dagger(I_a\otimes e^{i\hat{H}t})\tilde{U}^\dagger\Big)\\ &\quad + i\,\mathrm{Tr}\Big((|1\rangle\langle 0|\otimes I_p)\tilde{U}(I_a\otimes e^{-i\hat{H}t})\tilde{V}(\rho_a\otimes\rho_p)\tilde{V}^\dagger(I_a\otimes e^{i\hat{H}t})\tilde{U}^\dagger\Big)\\ &= \frac{1}{2}\Big(-i\langle U(t)V\rangle + i\langle V^\dagger U^\dagger(t)\rangle\Big) = \mathrm{Im}(\langle U(t)V\rangle)\end{aligned} \tag{2.41}$$

Hence

$$C_{UV(t)} = \langle U(t)V\rangle = \langle X\rangle + i\langle Y\rangle. \tag{2.42}$$

□

The original circuit proposed in Ref. [15, 16] is

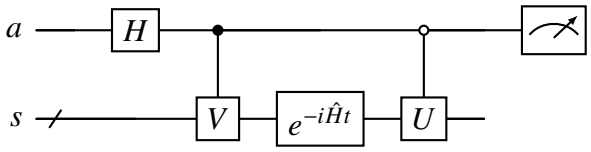

with control on $|0\rangle$ on the controlled-U gate. Equation 2.40 is then changed to

$$\langle X\rangle = \frac{1}{2}(\langle U^\dagger(t)V\rangle + \langle V^\dagger U(t)\rangle) = \mathrm{Re}(\langle U^\dagger(t)V\rangle), \tag{2.43}$$

and Eq. 2.41 becomes

$$\langle Y\rangle = \frac{1}{2}(-i\langle U^\dagger(t)V\rangle + i\langle V^\dagger U(t)\rangle) = \mathrm{Im}(\langle U^\dagger(t)V\rangle). \tag{2.44}$$

The result is measuring the quantity $\langle U^\dagger(t)V\rangle$ instead of $\langle U(t)V\rangle$.

We can also put a different state on the ancilla. For example, the following circuit

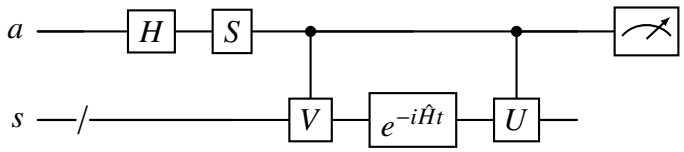

puts the ancilla density matrix in the form

$$\rho_a = \frac{1}{2}\begin{bmatrix}1 & -i\\ i & 1\end{bmatrix} \tag{2.45}$$

The expectation value of X becomes

$$\langle X \rangle = \frac{1}{2}\left(i\langle U(t)V\rangle - i\langle V^{\dagger}U^{\dagger}(t)\rangle \right) = -\,\mathrm{Im}(\langle U(t)V\rangle), \tag{2.46}$$

and the expectation value of Y becomes

$$\langle Y \rangle = \frac{1}{2}\left(\langle U(t)V\rangle + \langle V^{\dagger}U^{\dagger}(t)\rangle \right) = \mathrm{Re}(\langle U(t)V\rangle), \tag{2.47}$$

so that the correlation function is calculated as

$$C_{UV}(t) = \langle U(t)V\rangle = \langle Y\rangle - i\,\langle X\rangle\,. \tag{2.48}$$

Chapter 3

QUANTUM INFORMATION

This chapter reviews concepts from quantum information that are relevant to this thesis. Section 3.1 reviews the stabilizer formalism, which was originally introduced in quantum error correction but has been applied to other areas of quantum computing. Section 3.2 reviews noisy quantum channels, which are important in formulating noise on near-term quantum hardware. Section 3.3 defines special quantum states that are relevant to Chapter 7 of this thesis.

3.1 Stabilizer Formalism

Single-qubit Pauli operators consist of I, X, Y, Z. To turn these operators into a group, we need to attach multiplicative factors $\pm 1, \pm i$ and let

$$\mathcal{P}_1 = \{\pm I, \pm iI, \pm X, \pm iX, \pm Y, \pm iY, \pm Z, \pm iZ\} \tag{3.1}$$

which is the *Pauli group* on a single qubit. Similarly, we can define the *Pauli group on N qubits* by $\mathcal{P}_N = \mathcal{P}_1^{\otimes N}$, which consists of Pauli strings on N qubits with coefficients $\pm 1, \pm i$. By $\overline{\mathcal{P}}_1$ we mean the set of single-qubit Pauli operators with coefficient 1, and similarly by $\overline{\mathcal{P}}_N = \overline{\mathcal{P}}_1^{\otimes N}$ we mean the set of Pauli strings on N qubits with coefficient 1.

Consider a subgroup $\mathcal{S}$ of $\mathcal{P}_n$. Define the *stabilizer subspace* $V_\mathcal{S}$ to be

$$V_\mathcal{S} = \{|\psi\rangle : \boldsymbol{\sigma} |\psi\rangle = |\psi\rangle \text{ for all } \boldsymbol{\sigma} \in \mathcal{S}\}. \tag{3.2}$$

We can check $V_\mathcal{S}$ is indeed a subspace since for any $|\psi\rangle, |\psi'\rangle$ in $V_\mathcal{S}$, $\boldsymbol{\sigma} \in \mathcal{S}$ and a scalar α,

$$\boldsymbol{\sigma}(|\psi\rangle + |\psi'\rangle) = \boldsymbol{\sigma} |\psi\rangle + \boldsymbol{\sigma} |\psi'\rangle = |\psi\rangle + |\psi'\rangle, \tag{3.3}$$

$$\boldsymbol{\sigma}(\alpha |\psi\rangle) = \alpha \boldsymbol{\sigma} |\psi\rangle = \alpha |\psi\rangle. \tag{3.4}$$

A natural question to ask is that for what $\mathcal{S}$ is $V_\mathcal{S}$ nontrivial, i.e. $V_\mathcal{S} \neq \{0\}$. The answer is given in the following proposition.

Proposition 1. If $V_\mathcal{S}$ is nontrivial, $-I \notin \mathcal{S}$.

Proof. Take $|\psi\rangle \in V_{\mathcal{S}}$. Since $-I$ is a stabilizer,

$$-I\,|\psi\rangle = |\psi\rangle \implies -|\psi\rangle = |\psi\rangle \implies |\psi\rangle = 0. \tag{3.5}$$

□

From the proposition, we can derive a few corollaries that give necessary conditions for $V_{\mathcal{S}}$ to be nontrivial. An important property we will use on Pauli strings is that two Pauli strings either commute or anticommute. Moreover, for $\boldsymbol{\sigma}, \boldsymbol{\sigma}' \in \overline{\mathcal{P}}_N$, $\boldsymbol{\sigma}$ and $\boldsymbol{\sigma}'$ commute if $\boldsymbol{\sigma}\boldsymbol{\sigma}'$ has coefficient ± 1, and anticommute if $\boldsymbol{\sigma}\boldsymbol{\sigma}'$ has coefficient $\pm i$.

Corollary 2. Let $\boldsymbol{\sigma} \in \overline{\mathcal{P}}_N$. If $V_{\mathcal{S}}$ is nontrivial, $\pm i\boldsymbol{\sigma} \notin \mathcal{S}$.

Proof. If $\pm i\boldsymbol{\sigma} \in \mathcal{S}$, then $(\pm i\boldsymbol{\sigma})^2 = -I \in \mathcal{S}$, a contradiction. □

Corollary 3. If $V_{\mathcal{S}}$ is nontrivial, $-\boldsymbol{\sigma} \notin \mathcal{S}$ for any $\boldsymbol{\sigma} \in \mathcal{S}$.

Proof. For $\boldsymbol{\sigma} \in \mathcal{S}$, if $-\boldsymbol{\sigma} \in \mathcal{S}$, $\boldsymbol{\sigma}(-\boldsymbol{\sigma}) = -I \in \mathcal{S}$, a contradiction. □

Corollary 4. If $V_{\mathcal{S}}$ is nontrivial, all elements in $\mathcal{S}$ commute with each other.

Proof. If $\boldsymbol{\sigma}, \boldsymbol{\sigma}' \in \mathcal{S}$ don't commute with each other, they anticommute. Now $\boldsymbol{\sigma}\boldsymbol{\sigma}' \in \mathcal{S}$ implies $\boldsymbol{\sigma}\boldsymbol{\sigma}'\boldsymbol{\sigma}\boldsymbol{\sigma}' = -\boldsymbol{\sigma}\boldsymbol{\sigma}'\boldsymbol{\sigma}'\boldsymbol{\sigma} = -\boldsymbol{\sigma}\boldsymbol{\sigma} = -I \in \mathcal{S}$, a contradiction. □

We will call a subgroup $\mathcal{S}$ *stabilizer subgroup* if its stabilizer subspace $V_{\mathcal{S}}$ is nontrivial.

By Corollary 4, $\mathcal{S}$ is an abelian subgroup. Let $s_1, ..., s_L$ be the generators of $\mathcal{S}$, then it follows that any $\boldsymbol{\sigma} \in \mathcal{S}$ can be written as $\boldsymbol{\sigma} = s_1^{a_1} ... s_L^{a_L}$, where $a_1, ..., a_L \in \{0, 1\}$. Given $\mathcal{S} = \langle s_1, ..., s_L \rangle$, we want to know the dimension of $V_{\mathcal{S}}$. This is can be derived from the following theorem.

Theorem 5. Let

$$P_{\mathcal{S}} = \frac{1}{|\mathcal{S}|} \sum_{\boldsymbol{\sigma} \in \mathcal{S}} \boldsymbol{\sigma}. \tag{3.6}$$

Then $P_{\mathcal{S}}$ is the projector onto the subspace $V_{\mathcal{S}}$.

Proof. Observe that if $\boldsymbol{\sigma} \in \mathcal{S}$,

$$\boldsymbol{\sigma} P_{\mathcal{S}} = \frac{1}{|\mathcal{S}|} \sum_{\boldsymbol{\sigma} \in \mathcal{S}} \boldsymbol{\sigma}\boldsymbol{\tau} = \frac{1}{|\mathcal{S}|} \sum_{\boldsymbol{\tau} \in \boldsymbol{\sigma}^{-1}\mathcal{S}} \boldsymbol{\tau} = P_{\mathcal{S}}. \tag{3.7}$$

Hence

$$P_{\mathcal{S}}^2 = \frac{1}{|\mathcal{S}|} \sum_{\boldsymbol{\sigma} \in \mathcal{S}} \boldsymbol{\sigma} P_{\mathcal{S}} = \frac{1}{|\mathcal{S}|} \sum_{\boldsymbol{\sigma} \in \mathcal{S}} P_{\mathcal{S}} = P_{\mathcal{S}}, \tag{3.8}$$

which implies that $P_{\mathcal{S}}$ is a projector.
To show that $P_{\mathcal{S}}$ is the projector onto the subspace $V_{\mathcal{S}}$, for any $|\psi\rangle$ and any $\boldsymbol{\sigma} \in \mathcal{S}$, $\boldsymbol{\sigma} P_{\mathcal{S}} |\psi\rangle = P_{\mathcal{S}} |\psi\rangle$, so $\mathrm{im}(P_{\mathcal{S}}) \subseteq V_{\mathcal{S}}$. Moreover, for any $|\psi\rangle \in V_{\mathcal{S}}$, $|\psi\rangle = P_{\mathcal{S}} |\psi\rangle \in \mathrm{im}(P_{\mathcal{S}})$, which implies $V_{\mathcal{S}} \subseteq \mathrm{im}(P_{\mathcal{S}})$. Therefore $\mathrm{im}(P_{\mathcal{S}}) = V_{\mathcal{S}}$ and the statement is proved. □

The projector $P_{\mathcal{S}}$ can be written in another form:

$$P_{\mathcal{S}} = \frac{1}{|\mathcal{S}|} \sum_{\boldsymbol{\sigma} \in \mathcal{S}} \boldsymbol{\sigma} = \frac{1}{2^l} \sum_{a_1,\ldots,a_l \in \{0,1\}} s_1^{a_1} \ldots s_l^{a_l} = \prod_{i=1}^{l} \frac{(I + s_i)}{2} = \prod_{i=1}^{l} P_{\langle s_i \rangle = 1}. \tag{3.9}$$

That is, the projector onto the stabilizer subspace $V_{\mathcal{S}}$ is a product of projectors onto the +1 eigenspace of s_i. Intuitively, each projector reduces the subspace by half, so we would expect the dimension of the stabilizer subspace to be reduced from 2^N to 2^{N-L}. A rigorous justification is given in the following corollary.

Corollary 6. Let $\mathcal{S}$ be a stabilizer subgroup with L generators on an N-qubit system. Then $\dim(V_{\mathcal{S}}) = 2^{N-L}$, that is, $V_{\mathcal{S}}$ is equivalent to a Hilbert space with $N - L$ qubits.

Proof.

$$\dim(V_{\mathcal{S}}) = \mathrm{tr}(P_{\mathcal{S}}) = \frac{1}{|\mathcal{S}|} \sum_{\boldsymbol{\sigma} \in \mathcal{S}} \mathrm{tr}(\boldsymbol{\sigma}) = \frac{1}{2^L} \sum_{\boldsymbol{\sigma} \in \mathcal{S}} 2^N \delta_{\boldsymbol{\sigma}, I^{\otimes N}} = 2^{N-L}. \tag{3.10}$$

□

$\mathbb{F}_2$-linear algebra perspective

There is a useful representation of the Pauli strings in a stabilizer subgroup as a row vector of length $2N$. For any $\boldsymbol{\sigma} = \pm\sigma_1 \otimes ... \otimes \sigma_N$ in a stabilizer subgroup $\mathcal{S}$, let $r(\boldsymbol{\sigma})$ be its corresponding vector in $\mathbb{F}_2^{2n}$, where the elements are assigned such that

$$r(\boldsymbol{\sigma})_i = 0,\ r(\boldsymbol{\sigma})_{i+n} = 0 \text{ if } \boldsymbol{\sigma}_i = I; \tag{3.11}$$

$$r(\boldsymbol{\sigma})_i = 1,\ r(\boldsymbol{\sigma})_{i+n} = 0 \text{ if } \boldsymbol{\sigma}_i = X; \tag{3.12}$$

$$r(\boldsymbol{\sigma})_i = 0,\ r(\boldsymbol{\sigma})_{i+n} = 1 \text{ if } \boldsymbol{\sigma}_i = Z; \tag{3.13}$$

$$r(\boldsymbol{\sigma})_i = 1,\ r(\boldsymbol{\sigma})_{i+n} = 1 \text{ if } \boldsymbol{\sigma}_i = Y. \tag{3.14}$$

That is, the left N entries of $r(\boldsymbol{\sigma})$ indicate the positions of X or Y in $\boldsymbol{\sigma}$, the right N entries of $r(\boldsymbol{\sigma})$ indicate the positions of Y or Z in $\boldsymbol{\sigma}$. For example, the Pauli string XYZ corresponds to the vector

$$r(XYZ) = \left(\begin{array}{ccc|ccc} 1 & 1 & 0 & 0 & 1 & 1 \end{array}\right) \tag{3.15}$$

By Corollaries 2 and 3, if $\boldsymbol{\sigma} \in \mathcal{S}$, then $-\boldsymbol{\sigma}$ and $\pm i\boldsymbol{\sigma}$ are not in $\mathcal{S}$, so each vector corresponds to a unique element in $\mathcal{S}$.

The $\mathbb{F}_2$-vector representation reveals the products and commutation relations between any Pauli strings as operations on the vectors. For any two Pauli strings $\boldsymbol{\sigma}$ and $\boldsymbol{\sigma}'$ in $\mathcal{S}$, $r(\boldsymbol{\sigma}\boldsymbol{\sigma}') = r(\boldsymbol{\sigma}) + r(\boldsymbol{\sigma}')$. We can use this relation to find the independent generators of the stabilizer subgroup, since removing any generator makes the subgroup smaller. From the relation, finding the independent generators is the same as finding the independent vectors in the $\mathbb{F}_2$ representation.

To relate to the commutation relations between Pauli strings, we need some more tools. Let the inner product between two vectors $r(\boldsymbol{\sigma})$ and $r(\boldsymbol{\sigma})'$ be defined as

$$\langle r(\boldsymbol{\sigma}), r(\boldsymbol{\sigma}')\rangle_\Lambda = r(\boldsymbol{\sigma})\Lambda r(\boldsymbol{\sigma})^T, \qquad \Lambda = \begin{bmatrix} 0 & I_n \\ I_n & 0 \end{bmatrix}, \tag{3.16}$$

where I_n is the identity matrix of size $N \times N$. Write $r(\boldsymbol{\sigma}) = (r_x(\boldsymbol{\sigma})\ r_z(\boldsymbol{\sigma}))$. The inner product is explicitly

$$\langle r(\boldsymbol{\sigma}), r(\boldsymbol{\sigma}')\rangle_\Lambda = \begin{bmatrix} r_x(\boldsymbol{\sigma}) & r_z(\boldsymbol{\sigma}) \end{bmatrix} \begin{bmatrix} 0 & I_n \\ I_n & 0 \end{bmatrix} \begin{bmatrix} r_x(\boldsymbol{\sigma}')^T \\ r_z(\boldsymbol{\sigma}')^T \end{bmatrix} = \langle r_x(\boldsymbol{\sigma}), r_z(\boldsymbol{\sigma}')\rangle + \langle r_z(\boldsymbol{\sigma}), r_x(\boldsymbol{\sigma}')\rangle \,. \tag{3.17}$$

Intuitively, the inner product $\langle\cdot,\cdot\rangle_\Lambda$ appears as a "twisted" inner product. In mathematical terms the inner product is called a *symplectic inner product* because of the symplecticity of the metric Λ.

With this inner product, we can characterize commutation relation between $\boldsymbol{\sigma}$ and $\boldsymbol{\sigma}'$, as given in the following proposition.

Proposition 7. $[\boldsymbol{\sigma}, \boldsymbol{\sigma}'] = 0$ if and only if $\langle r(\boldsymbol{\sigma}), r(\boldsymbol{\sigma}')\rangle_\Lambda = 0$.

Proof. For any single-qubit Pauli operator σ, let $\sigma^{(a_1,...,a_N)}$ with $(a_1, ..., a_N) \in \mathbb{F}_2^n$ denote the Pauli string $\sigma^{a_1} \otimes ... \otimes \sigma^{a_N}$. By definitions of the r vectors,

$$\boldsymbol{\sigma} = (-1)^\eta X^{r_x(\boldsymbol{\sigma})} Z^{r_z(\boldsymbol{\sigma})}, \tag{3.18}$$

$$\boldsymbol{\sigma}' = (-1)^{\eta'} X^{r_x(\boldsymbol{\sigma}')} Z^{r_z(\boldsymbol{\sigma}')}, \tag{3.19}$$

$$\tag{3.20}$$

where $\eta, \eta' \in \{0, 1\}$. Note that

$$\begin{aligned} \boldsymbol{\sigma}\boldsymbol{\sigma}' &= (-1)^{\eta+\eta'} X^{r_x(\boldsymbol{\sigma})} Z^{r_z(\boldsymbol{\sigma})} X^{r_x(\boldsymbol{\sigma}')} Z^{r_z(\boldsymbol{\sigma}')} && (3.21)\\ &= (-1)^{\eta+\eta'+\langle r_x(\boldsymbol{\sigma}'), r_z(\boldsymbol{\sigma})\rangle} X^{r_x(\boldsymbol{\sigma})} X^{r_x(\boldsymbol{\sigma}')} Z^{r_z(\boldsymbol{\sigma})} Z^{r_z(\boldsymbol{\sigma}')} && (3.22)\\ &= (-1)^{\eta+\eta'+\langle r_x(\boldsymbol{\sigma}'), r_z(\boldsymbol{\sigma})\rangle+\langle r_x(\boldsymbol{\sigma}), r_z(\boldsymbol{\sigma}')\rangle} X^{r_x(\boldsymbol{\sigma}')} Z^{r_z(\boldsymbol{\sigma}')} X^{r_x(\boldsymbol{\sigma})} Z^{r_z(\boldsymbol{\sigma})} && (3.23)\\ &= (-1)^{\langle r(\boldsymbol{\sigma}), r(\boldsymbol{\sigma}')\rangle_\Lambda} \boldsymbol{\sigma}'\boldsymbol{\sigma}. && (3.24) \end{aligned}$$

The conclusion follows naturally. □

With the vector space $\mathbb{F}_2^{2n}$, a base field $\mathbb{F}_2$ and an inner product defined, we can do linear algebra on the $\mathbb{F}_2$ representation. The rank-nullity theorem still holds, as given in the following theorem.

Theorem 8. Let W be a k-dimensional subspace of $\mathbb{F}_2^n$. Then $\dim(W^\perp) = n - k$.

However, because of self-orthogonality of vectors in vector spaces over $\mathbb{F}_2$, even if we have a set of linearly independent vectors, we can't necessarily orthogonalize them to an orthogonal set of vectors. In fact, in $\mathbb{F}_2^{2n}$, we can at most have n mutually orthogonal vectors, a fact captured in the theorem below.

Theorem 9. Let $\{\mathbf{v}_1, ..., \mathbf{v}_k\}$ be an orthogonal set of vectors in $\mathbb{F}_2^{2n}$ with respect to the symplectic inner product $\langle \cdot, \cdot \rangle_\Lambda$ and each $\mathbf{v}_i \neq \mathbf{0}$. Then $k \leq n$.

Proof. Let $W = \text{span}(\{\mathbf{v}_1, ..., \mathbf{v}_k\})$. Since each vector is orthogonal to itself, $\mathbf{v}_i \in W^\perp$ for $i = 1, ..., k$. Hence W is a subspace of $W^\perp$ and $\dim(W^\perp) \geq \dim(W) = k$. Then

$$2k = k + k \leq \dim(W) + \dim(W^\perp) = 2n, \tag{3.25}$$

which implies $k \leq n$. □

Theorem 9 expresses the idea that we can find at most n mutually commuting nontrivial Pauli strings (that is, excluding the identity operator). One set of Pauli strings is

$$Z_1, Z_2, ..., Z_n. \tag{3.26}$$

In the next section, using the theory of Clifford groups, we will show that any set of k mutually commuting Pauli strings for some $k \leq n$ is equivalent to $Z_1, Z_2, ..., Z_k$.

Operations on the stabilizer subspace

Given a stabilizer subspace, an important class of operators is the ones that preserve this subspace. In other words, for $|\psi\rangle \in V_\mathcal{S}$, we want to find operators $\boldsymbol{\tau}$ such that $\boldsymbol{\tau}|\psi\rangle \in V_\mathcal{S}$. If we restrict our states to the subspace $V_\mathcal{S}$, these are the only viable operations on $V_\mathcal{S}$.

This gives rise to the idea of normalizers. Specifically, an element $\boldsymbol{\tau} \in \mathcal{P}_n$ normalizes $\mathcal{S}$ if for any $\boldsymbol{\sigma} \in \mathcal{S}$, $\boldsymbol{\tau}\boldsymbol{\sigma}\boldsymbol{\tau}^{-1} \in \mathcal{S}$. Since two Pauli strings either commute or anticommute, $\boldsymbol{\tau}\boldsymbol{\sigma}\boldsymbol{\tau}^{-1} = \boldsymbol{\sigma}$ if $\boldsymbol{\sigma}$ and $\boldsymbol{\tau}$ commute and $\boldsymbol{\tau}\boldsymbol{\sigma}\boldsymbol{\tau}^{-1} = -\boldsymbol{\sigma}$ if $\boldsymbol{\sigma}$ and $\boldsymbol{\tau}$ anticommute. But we know that if $\boldsymbol{\sigma} \in \mathcal{S}$, $-\boldsymbol{\sigma} \notin \mathcal{S}$, so $\boldsymbol{\tau}\boldsymbol{\sigma}\boldsymbol{\tau}^{-1} = \boldsymbol{\sigma}$ for any $\boldsymbol{\sigma} \in \mathcal{S}$. We shall call this group the normalizer of $\mathcal{S}$ and write it as $\mathcal{N}(\mathcal{S})$.

We can move on to analyze the number of elements in this normalizer subgroup. Let $r(\mathcal{S})$ be $\text{span}(\{r(\boldsymbol{\sigma}) : \boldsymbol{\sigma} \in \mathcal{S}\})$ and similarly for $r(\mathcal{N}(\mathcal{S}))$. Clearly $r(\mathcal{N}(\mathcal{S})) =$

$r(\mathcal{S})^{\perp}$. Then

$$\dim r(\mathcal{N}(\mathcal{S})) = \dim r(\mathcal{S})^{\perp} = 2n - l. \tag{3.27}$$

Therefore, $\mathcal{N}(\mathcal{S})$ is a subgroup with $2n - l$ generators and hence 2^{2n-l} elements ignoring multiplicative factors $\pm 1, \pm i$.

Since $\mathcal{S}$ is a normal subgroup of $\mathcal{N}(\mathcal{S})$, we can form the quotient group $\mathcal{N}(\mathcal{S})/\mathcal{S}$, where each coset in $\mathcal{N}(\mathcal{S})/\mathcal{S}$ represents an equivalent class of operations on the stabilizer subspace $V_{\mathcal{S}}$. The generators of the quotient group $\mathcal{N}(\mathcal{S})/\mathcal{S}$ is $n-l$, and it contains 2^{n-l} coset ignoring multiplicative factors $\pm 1, \pm i$. In practice, we can choose the multiplicative factors arbitrarily to fit our purpose. Note that the multiplicative factor of each coset representative fully determines the members of the coset if we revert to $\mathcal{N}(\mathcal{S})$. But if we are only considering equivalent operations on $V_{\mathcal{S}}$, the multiplicative factor does not matter.

There are more general operations we can perform on the stabilizer subspace that don't preverse the subspace but permute it to another subspace within the Hilbert space. Suppose we evolve the state $|\psi\rangle$ to $U|\psi\rangle$. Since

$$UO|\psi\rangle = UOU^{\dagger}U|\psi\rangle,$$

$|\psi\rangle$ is an eigenvector of O with eigenvalue λ if and only if $U|\psi\rangle$ is an eigenvector of $UOU^{\dagger}$ with eigenvalue λ. Therefore, after evolution by U, the stabilizer group for the new state $U|\psi\rangle$ is $U\mathcal{S}U^{\dagger}$. In general $U\mathcal{S}U^{\dagger}$ might not be in $\mathcal{P}_n$, but we want to restrict our attention to the unitary operators that conjugates any stabilizer into $\mathcal{P}_n$. To consider all stabilizer subgroups $\mathcal{S}$ in $\mathcal{P}_n$, we need to consider unitary operators that satisfy $U\mathcal{P}_nU^{\dagger} \subseteq \mathcal{P}_n$, or the normalizer $N_{U(2^n)}(\mathcal{P}_n) \equiv N(\mathcal{P}_n)$. Since the centralizer of $\mathcal{P}_n$ in $U(2^n)$ is $U(1)$, by a result in group theory $N(\mathcal{P}_n)/U(1)$ is isomorphic to a subgroup of $\mathrm{Aut}(\mathcal{P}_n)$. Define the quotient group $N(\mathcal{P}_n)/U(1)$ to be the Clifford group $\mathcal{C}_n$.

Lemma 10. The Clifford group on one qubit is generated by the Hadamard gate H and the phase gate S, that is $\mathcal{C}_1 = \langle H, S\rangle$.

Proof. Let Φ be any automorphism of $\mathcal{P}_1$ by conjugation with a unitary operator. To find out the action of Φ, we only need to find the images of the generators X, Y, Z. Since X and $\Phi(X)$ have the same order, X can only be mapped to one of $\{\pm X, \pm Y, \pm Z\}$. After X is determined, Z can be mapped to $\{\pm X, \pm Y, \pm Z\} \setminus \{\pm\Phi(X)\}$. $\Phi(Y)$ is determined by $\Phi(X)$ and $\Phi(Z)$ since

$$\Phi(Y) = \Phi(iIXZ) = \Phi(iI)\Phi(X)\Phi(Z) = i\Phi(X)\Phi(Z).$$

The automorphisms of $\mathcal{P}_1$ by conjugation with a unitary operator is equivalent to all orientation-preserving permutations of the three coordinate axes. Therefore $C_1 \cong O$ where O is the rotational subgroup of the octahedral group. Let this isomorphism be Γ. Note that

$$HXH^\dagger = Z, HYH^\dagger = -Y, HZH^\dagger = X,$$

so $\Gamma(H)$ is rotation by π along the unit vector $\frac{1}{\sqrt{2}}(\hat{\mathbf{x}} + \hat{\mathbf{z}})$. Similarly,

$$SXS^\dagger = Y, SYS^\dagger = -X, SZS^\dagger = Z,$$

so $\Gamma(S)$ is rotation counterclockwise by $\pi/2$ along $\hat{\mathbf{z}}$.
The group O is isomorphic to S_4 when regarded as permuting the four body diagonals of the cube. Define an isomorphism from C_1 to S_4 such that the image of R is what $\Gamma(R)$ does to the four body diagonals. Under this isomorphism,

$$H \mapsto (12),$$
$$S \mapsto (1234).$$

Since (12) and (1234) generates S_4, H and S generates C_1. Therefore, $C_1 = \langle H, S \rangle$. □

Clifford group element	Transformation	Effect
H	$X \to Z, Y \to -Y, Z \to X$	$X \leftrightarrow Z$
S	$X \to Y, Y \to -X, Z \to Z$	$X \leftrightarrow Y$
HS	$X \to -Y, Y \to -Z, Z \to X$	$X \to Y \to Z \to X$
SH	$X \to Z, Y \to X, Z \to -Y$	$X \to Z \to Y \to X$
HSH	$X \to X, Y \to Z, Z \to -Y$	$Y \leftrightarrow Z$

Table 3.1: Clifford transformation between single-qubit Pauli strings.

3.2 Noisy Quantum Channels

Definition

A quantum operation describes how a quantum system evolves. Despite the generality of quantum operations, they have a precise mathematical definition.

Definition. A *quantum operation* is a linear map

$$\mathcal{E} : \mathcal{L}(H_1) \to \mathcal{L}(H_2)$$

such that
(1) (Completely positive) If we introduce an extra system B and let $\mathcal{I}$ be the identity operator on B, $(\mathcal{I} \otimes \mathcal{E})(A)$ is positive for any positive operator $A \in \mathcal{L}(B \otimes H_1)$.
(2) (Non-trace-increasing) For all $O \in \mathcal{L}(H_1)$, $\mathrm{tr}(\mathcal{E}(O)) \leq \mathrm{tr}(O)$.
In property (2), if $\mathrm{tr}(\mathcal{E}(O)) = \mathrm{tr}(O)$ for all $O \in \mathcal{L}(H_1)$ then $\mathcal{E}$ is trace-preserving. A trace-preserving quantum operation is called a *quantum channel*.

Quantum operations are defined on the space of general linear operators on a Hilbert space, we will primarily encounter it as operators on the density matrices.
If the system is a closed system, the only permissible quantum operations are unitary evolution, that is $\rho \mapsto U\rho U^\dagger$ where U is a unitary operator on the Hilbert space. When we do a measurement, the operation of a single measurement operator M_m defined as $\rho \mapsto M_m \rho M_m^\dagger$ is also a valid quantum operation.
When the system is open, we can regard the quantum operation as evolving the whole system and tracing out the environment, that is

$$\mathcal{E}(\rho) = \mathrm{tr}_{\mathrm{env}}(U(\rho \otimes \rho_{\mathrm{env}})U^\dagger). \tag{3.28}$$

Suppose the environment has basis $\{|e_k\rangle\}$. Without loss of generality, we can assume the environment to be in a pure state $|e_0\rangle$, since if it is not in a pure state we can introduce an extra system to purify it. Then Eq. 3.28 corresponds to

$$\mathcal{E}(\rho) = \sum_k \left\langle e_k|U(\rho \otimes |e_0\rangle \langle e_0|)U^\dagger|e_k\right\rangle_{\mathrm{env}} = \sum_k E_k \rho E_k^\dagger$$

where $E_k = \langle e_k|U|e_0\rangle_{\mathrm{env}}$ is an operator on the state space of the system. This is the operator-sum representation of quantum operations.
The operation is trace-preserving if $\mathrm{tr}(\mathcal{E}(\rho)) = 1$, which is equivalent to $\sum_k E_k^\dagger E_k = I$. The state after the operation is just $\mathcal{E}(\rho)$. The operation is non-trace preserving if $\mathrm{tr}(\mathcal{E}(\rho)) \leq 1$, which is equivalent to $\sum_k E_k^\dagger E_k \leq I$. The state after the operation is $\mathcal{E}(\rho)/\mathrm{tr}(\mathcal{E}(\rho))$

Theorem 11. The map $\mathcal{E}$ is a quantum operation if and only if

$$\mathcal{E}(O) = \sum_k E_k O E_k^\dagger$$

for some set of operators $\{E_k\}$ such that each E_k maps the input Hilbert space to the output Hilbert space and $\sum_k E_k^\dagger E_k \leq I$.

Below we look at some examples of noisy quantum channels.

Examples of Quantum Channels

The action of a dephasing channel is

$$\mathcal{E}(\rho) = \left(1 - \frac{p}{2}\right)\rho + \frac{p}{2} Z\rho Z,$$

which has the Kraus operator representation

$$\begin{aligned}\mathcal{E}(\rho) &= K_0 \rho K_0^\dagger + K_1 \rho K_1^\dagger, \\ K_0 &= \sqrt{1 - p/2} I, K_1 = \sqrt{p/2} Z.\end{aligned}$$

A generic density matrix transforms as

$$\begin{bmatrix}\rho_{00} & \rho_{01} \\ \rho_{10} & \rho_{11}\end{bmatrix} \overset{\mathcal{E}}{\longmapsto} \begin{bmatrix}\rho_{00} & (1-p)\rho_{01} \\ (1-p)\rho_{10} & \rho_{11}\end{bmatrix}.$$

Here $0 \leq p \leq 1$, and when $p = 1$ the coherence (off-diagonal elements) between the two states is lost.

The amplitude damping channel is a result of energy dissipation and transfers population of a qubit in the state $|1\rangle$ to the state $|0\rangle$. Kraus operator representation of the amplitude damping channel is

$$\begin{aligned}\mathcal{E}_{\text{amp-damp}}(\rho) &= K_0 \rho K_0^\dagger + K_1 \rho K_1^\dagger, \\ K_0 = \begin{bmatrix}1 & 0 \\ 0 & \sqrt{1-\gamma}\end{bmatrix}, K_1 &= \begin{bmatrix}0 & \sqrt{\gamma} \\ 0 & 0\end{bmatrix},\end{aligned}$$

where $0 \leq \gamma \leq 1$. γ can be thought of as the probability of losing a photon, but note that the amplitude damping channel is applied deterministically on the density matrix.

A generic density matrix transforms as

$$\mathcal{E}_{\text{amp-damp}}(\rho) = \begin{bmatrix}\rho_{00} + \gamma\rho_{11} & \sqrt{1-\gamma}\rho_{01} \\ \sqrt{1-\gamma}\rho_{10} & (1-\gamma)\rho_{11}\end{bmatrix},$$

from which we can see that when $\gamma = 1$ all population is transferred to the ground state $|0\rangle$.

The depolarizing channel replaces the state with a completely mixed state $I/2$ with probability p and leaves the state unchanged with probability $1 - p$, that is [32]

$$\mathcal{E}_{\text{depolarizing}}(\rho) = (1-p)\rho + p\frac{I}{2} \tag{3.29}$$

Using the identity

$$\frac{I}{2} = \frac{\rho + X\rho X + Y\rho Y + Z\rho Z}{4}$$

for any single-qubit density matrix ρ, we can rewrite Eq. 3.29 in Kraus operator representation

$$\mathcal{E}_{\text{depolarizing}}(\rho) = \left(1 - \frac{3}{4}p\right)\rho + \frac{p}{4}(X\rho X + Y\rho Y + Z\rho Z),$$

where $0 \leq p \leq 1$ as in Eq. 3.29.

Alternatively, we can write the depolarizing channel as

$$\mathcal{E}_{\text{depolarizing}}(\rho) = (1-p)\,\rho + \frac{p}{3}(X\rho X + Y\rho Y + Z\rho Z),$$

where now $0 \leq p \leq 3/4$. This is the representation used in Ref. [33]. In particular, Cirq [34] applies the depolarizing channel by leaving the state unchanged with probability $1 - p$ and applying an X, Y or Z gate with probability $p/3$.

Master Equation Representations

The master equation has the general form

$$\dot{\rho} = -\frac{i}{\hbar}[\hat{H}, \rho] + \mathcal{D}[\hat{O}](\rho)$$

where the dissipator $\mathcal{D}$ is the operation

$$\mathcal{D}[\hat{O}](\cdot) = \hat{O} \cdot \hat{O}^\dagger - \frac{1}{2}\hat{O}^\dagger\hat{O} \cdot - \frac{1}{2} \cdot \hat{O}^\dagger\hat{O}.$$

Below we will derive amplitude damping and dephasing from the master equation formalism.

Amplitude damping channel

Consider the following master equation

$$\dot{\rho} = \frac{1}{T_1}\mathcal{D}[\sigma_-](\rho) = \frac{1}{T_1}\left(\sigma_-\rho\sigma_+ - \frac{1}{2}\sigma_+\sigma_-\rho - \frac{1}{2}\rho\sigma_+\sigma_-\right).$$

The raising and lowering operators have the expressions

$$\sigma_+ = \begin{bmatrix} 0 & 0 \\ 1 & 0 \end{bmatrix}, \quad \sigma_- = \begin{bmatrix} 0 & 1 \\ 0 & 0 \end{bmatrix}, \quad \sigma_+\sigma_- = \begin{bmatrix} 0 & 0 \\ 0 & 1 \end{bmatrix}.$$

From these expressions, we obtain the differential equation

$$\dot{\rho} = \frac{1}{T_1}\begin{bmatrix} \rho_{11} & -\rho_{01}/2, \\ -\rho_{01}^*/2 & -\rho_{11} \end{bmatrix},$$

or in element-wise form

$$\dot{\rho}_{00} = \frac{1}{T_1}\rho_{11},$$
$$\dot{\rho}_{01} = -\frac{1}{2T_1}\rho_{01}.$$
$$\dot{\rho}_{11} = -\frac{1}{T_1}\rho_{11}.$$

The latter two differential equations have the solutions

$$\rho_{01}(t) = \rho_{01}e^{-t/2T_1},$$
$$\rho_{11}(t) = \rho_{11}e^{-t/T_1},$$

from which we can write down the density matrix at time t as

$$\rho(t) = \begin{bmatrix} 1-\rho_{11}e^{-t/T_1} & \rho_{01}e^{-t/2T_1} \\ \rho_{01}^*e^{-t/2T_1} & \rho_{11}e^{-t/T_1} \end{bmatrix}.$$

This is the same as an amplitude-damping channel with damping rate $\gamma = 1/T_\phi$.

Dephasing channel

The dephasing channel can be derived from a master equation of the form

$$\dot{\rho} = \frac{1}{2T_\phi}\mathcal{D}[\sigma_z](\rho) = \frac{1}{2T_\phi}(\sigma_z\rho\sigma_z - \rho).$$

Explicitly

$$\dot{\rho} = -\frac{1}{T_\phi}\begin{bmatrix} 0 & \rho_{01} \\ \rho_{01}^* & 0 \end{bmatrix}.$$

and in element-wise form

$$\rho_{01} = -\frac{1}{T_\phi}\rho_{01}.$$

The solution is

$$\rho_{01}(t) = \rho_{01}e^{-t/T_\phi}.$$

So under this master equation

$$\rho(t) = \begin{bmatrix} \rho_{00} & \rho_{01}e^{-t/T_\phi} \\ \rho_{01}^*e^{-t/T_\phi} & \rho_{11} \end{bmatrix}$$

which corresponds to a dephasing channel with dephasing probability $p = 1-e^{-t/T_\phi}$.

Amplitude phase damping channel and T_2

Under both the amplitude and phase damping, the density matrix is transformed to the form

$$\rho(t) = \begin{bmatrix} 1 - \rho_{11} e^{-t/T_1} & \rho_{01} e^{-t(1/2T_1 + 1/T_\phi)} \\ \rho_{01}^* e^{-t(1/2T_1 + 1/T_\phi)} & \rho_{11} e^{-t/T_1} \end{bmatrix}.$$

The off-diagonal elements have the compound effect from both T_1 and T_ϕ. We can define a new relaxation time T_2 such that [35]

$$\frac{1}{T_2} = \frac{1}{2T_1} + \frac{1}{T_\phi}$$

so that T_2 is the effective relaxation time observed on the off-diagonal elements in experiments.

3.3 Entanglement and Special Quantum States

The entanglement is defined as the entropy of the reduced density matrix.

On three qubits, there are two different kinds of maximum entanglement [36], which are given by the GHZ state

$$|\text{GHZ}\rangle = \frac{1}{\sqrt{2}}(|000\rangle + |111\rangle) \tag{3.30}$$

and the W state

$$|W\rangle = \frac{1}{\sqrt{3}}(|001\rangle + |010\rangle + |100\rangle). \tag{3.31}$$

The GHZ state is maximally entangled with entanglement entropy 1 after tracing over any qubit. However, if any one of the qubits is traced out, the state is completely unentangled:

$$\text{Tr}_0(|\text{GHZ}\rangle\langle\text{GHZ}|) = \frac{1}{2}(|00\rangle\langle 00| + |11\rangle\langle 11|) \to \frac{1}{2}\begin{bmatrix} 1 & 0 & 0 & 0 \\ 0 & 0 & 0 & 0 \\ 1 & 0 & 0 & 0 \\ 0 & 0 & 0 & 1 \end{bmatrix} \tag{3.32}$$

On the other hand, the W state is not maximally entangled, since it has entanglement entropy

$$S = -\frac{1}{3}\log\frac{1}{3} - \frac{2}{3}\log\frac{2}{3} = 0.918296. \tag{3.33}$$

However, after tracing out any qubit, the resulting state is

$$\mathrm{Tr}_0(|\mathrm{GHZ}\rangle\langle\mathrm{GHZ}|) = \frac{1}{3}(|00\rangle\langle 00| + |01\rangle\langle 01| + |01\rangle\langle 10| + |10\rangle\langle 01| + |10\rangle\langle 10|) \tag{3.34}$$

$$\rightarrow \frac{1}{3}\begin{bmatrix} 1 & 0 & 0 & 0 \\ 0 & 1 & 1 & 0 \\ 0 & 1 & 1 & 0 \\ 0 & 0 & 0 & 0 \end{bmatrix} \tag{3.35}$$

Contrary to the GHZ state, the entanglement of $|W\rangle$ is maximally robust under disposal of any qubit.

Note that both the GHZ state and the W state can be generalized to N qubits. The N-qubit GHZ state is

$$|\mathrm{GHZ}\rangle = \frac{1}{\sqrt{2}}(|00...0\rangle + |11...1\rangle), \tag{3.36}$$

and the N-qubit W state is

$$|W\rangle = \frac{1}{\sqrt{N}}(|100...0\rangle + |010...0\rangle + ... + |000...1\rangle). \tag{3.37}$$

Cluster States

Cluster states can be defined on a graph with N sites. For a site i, let $\Gamma(i)$ denote all the neighbors of i on the graph. The cluster states are stabilized by the N stabilizers of the form

$$X_i \bigotimes_{j\in\Gamma(i)} Z_j. \tag{3.38}$$

An N-qubit state stabilized by N stabilizers is thus a one-dimensional space.

To create this state, we start with $|00...0\rangle$ and apply the Hadamard gate H to each site to create the state $|++...+\rangle$, then apply CZ to every edge on the graph to obtain the cluster state. In the stabilizer formalism, the stabilizers are transformed respectively as

$$Z_i \xrightarrow{H_i} X_i \xrightarrow{\prod_{j\in\Gamma(i)} \mathrm{CZ}_{ij}} X_i \bigotimes_{j\in\Gamma(i)} Z_j. \tag{3.39}$$

We can better see the structure of the cluster state by consider the following two relations

$$\mathrm{CZ}\,|\pm 0\rangle = |\pm 0\rangle\,, \tag{3.40}$$

$$\mathrm{CZ}\,|\pm 1\rangle = |\mp 1\rangle\,. \tag{3.41}$$

To use these two relatoins, we write states on all odd sites in Z basis, and states on all even sites in X basis. On three sites, for example

$$|+++\rangle = \frac{1}{2}\left(|0+0\rangle + |1+1\rangle + |0+1\rangle + |1+0\rangle\right) \tag{3.42}$$

$$\xrightarrow{\text{CZs}} \frac{1}{2}\left(|0+0\rangle + |1+1\rangle + |0-1\rangle + |1-0\rangle\right) \tag{3.43}$$

$$= \frac{1}{\sqrt{2}}\left[\frac{1}{\sqrt{2}}\left(|00\rangle_{\text{odd}} + |11\rangle_{\text{odd}}\right)|+\rangle_{\text{even}} + \frac{1}{\sqrt{2}}\left(|01\rangle_{\text{odd}} + |10\rangle_{\text{odd}}\right)|-\rangle_{\text{even}}\right] \tag{3.44}$$

In the last line, we regrouped the odd sites together and the even sites together. Hence, we see that the cluster states is characterized by odd sites in X basis which define the domain walls, and a cat-like GHZ state on the odd sites that obey the domain wall property.

The number of terms in the above expansion is 2. In general, for $2N$ or $2N-1$ sites, the number of terms is $N-1$ (with or without periodic boundary condition), since the last domain wall can be completely determined if the first N domain walls are specified. For example, in a four-site model, the original all + state is transformed as

$$|++++\rangle \longrightarrow \frac{1}{2}\left(|0+0+\rangle + |1+1+\rangle + |0-1+\rangle + |1-0+\rangle\right) \tag{3.45}$$

$$\longrightarrow \frac{1}{2}\left(|0+0+\rangle + |1+1-\rangle + |0-1-\rangle + |1-0+\rangle\right). \tag{3.46}$$

In general, given two sublattices A and B of a bipartite graph, let s_i and σ_i denote the state on the ith qubit in the X and Z basis, respectively. We will use the shorthand $\{\sigma\} = \{\sigma_i\}_{i\in A}$ and $\{s\} = \{s_j\}_{j\in B}$. The general cluster state is written down as

$$|\psi\rangle = \frac{1}{\sqrt{2^{N-1}}}\sum_{\{s\}} |\mathrm{GHZ}(\{\sigma\})\rangle_A\,|\{s\}\rangle_B \tag{3.47}$$

where

$$\boxed{|\mathrm{GHZ}(\{\sigma\})\rangle_A = \frac{1}{\sqrt{2}}\left(|\{\sigma_i\}\rangle_A + |\{1-\sigma_i\}\rangle_A\right)}. \tag{3.48}$$

such that both $|\{\sigma_i\}\rangle_A$ and $|\{1-\sigma_i\}\rangle_A$ satisfy the domain wall relation specified by the B sublattice.

Chapter 4

QUANTUM MANY-BODY SYSTEMS

This chapter reviews quantum many-body systems, which are the target of quantum simulation that forms the main topic of this thesis. We start with reviewing spin models in Sec. 4.1, then move on to molecular models in Sec. 4.2, and finally to qubit encoding schemes in Sec. 4.3.

4.1 Spin Models

Ising Model

An Ising model with an external field h has the Hamiltonian [37]

$$H = -J \sum_{\langle ij \rangle} \sigma_i \sigma_j - h \sum_i \sigma_i \tag{4.1}$$

The Ising model is ferromagnetic when $J > 0$ since the spins tend to align at ground state; the model is anti-ferromagnetic when $J < 0$ since the spins tend to anti-align at ground state.

We use the shorthand $\{\sigma\}$ to denote all configurations $\{\sigma_i = \pm 1\}_{i=1}^N$. The partition function is written as

$$\mathcal{Z} = \sum_{\{\sigma\}} e^{\beta J \sum_{\langle ij \rangle} \sigma_i \sigma_j + \beta h \sum_i \sigma_i} \tag{4.2}$$

Assume the model is 1D with periodic boundary condition so that $\sigma_{N+1} \equiv \sigma_1$. We can write the partition function in symmetric form as

$$\mathcal{Z} = \sum_{\{\sigma\}} e^{\beta \sum_{i=1}^N \left(J \sigma_i \sigma_{i+1} + \frac{1}{2} h (\sigma_i + \sigma_{i+1}) \right)} = \sum_{\{\sigma\}} T_{\sigma_1 \sigma_2} T_{\sigma_2 \sigma_3} \ldots T_{\sigma_N \sigma_1} = \mathrm{Tr}\left(T^N \right). \tag{4.3}$$

where T is the 2×2 matrix

$$T = \begin{bmatrix} T_{+1,+1} & T_{+1,-1} \\ T_{-1,+1} & T_{-1,-1} \end{bmatrix} = \begin{bmatrix} e^{\beta(J+h)} & e^{-\beta J} \\ e^{-\beta J} & e^{\beta(J-h)} \end{bmatrix}. \tag{4.4}$$

The eigenvalues of T can be found to be

$$\lambda_\pm = e^{\beta J} \left(\cosh(\beta h) \pm \sqrt{\sinh^2(\beta h) + e^{-4\beta J}} \right). \tag{4.5}$$

so that the partition function is

$$\boxed{\mathcal{Z} = \mathrm{Tr}\left(T^N\right) = \lambda_+^N + \lambda_-^N}, \tag{4.6}$$

which reduces to λ_+^N as $N \to \infty$. From the partition function, we can obtain the free energy in the thermodynamic limit as

$$F/N = -\frac{1}{\beta N}\ln\mathcal{Z} = -\frac{1}{\beta}\ln\lambda_+ = -J - \frac{1}{\beta}\ln\left(\cosh(\beta h) + \sqrt{\sinh^2(\beta h) + e^{-4\beta J}}\right). \tag{4.7}$$

We can also calculate the expectation of a single spin and the correlation between two spins. For a single spin, one approach is to take the derivative of the free energy,

$$\langle\sigma_i\rangle = -\frac{\partial(F/N)}{\partial h} = \frac{1}{\beta}\frac{\sinh^2(\beta h)\beta + \frac{2\sinh(\beta h)\cosh(\beta h)\beta}{2\sqrt{\sinh^2(\beta h)+e^{-4\beta J}}}}{\cosh(\beta h) + \sqrt{\sinh^2(\beta h) + e^{-4\beta J}}} = \frac{\sinh(\beta h)}{\sqrt{\sinh^2(\beta h) + e^{-4\beta J}}}. \tag{4.8}$$

Another approach is to do matrix multiplication using the T matrix. Suppose $T = U\Lambda U^\dagger$ where $\Lambda = \begin{bmatrix} \lambda_+^N & 0 \\ 0 & \lambda_-^N \end{bmatrix} \to \begin{bmatrix} \lambda_+^N & 0 \\ 0 & 0 \end{bmatrix}$. We can calculate the spin expectation value as

$$\langle\sigma_i\rangle = \frac{1}{\mathcal{Z}}\mathrm{Tr}\left(e^{-\beta H}Z_i\right) = \frac{1}{\lambda_+^N}\mathrm{Tr}\left(T^N Z_i\right) = \frac{1}{\lambda_+^N}\mathrm{Tr}\left(\Lambda^N U Z_i U^\dagger\right) = \mathrm{Tr}\left(U Z_i U^\dagger\right) = \frac{\sinh(\beta h)}{\sqrt{\sinh^2(\beta h) + e^{-4\beta J}}} \tag{4.9}$$

Note that at zero field $h = 0$, $\langle\sigma_i\rangle = 0$ for any temperature $T \neq 0$. This shows that in 1D, there is no spontaneous magnetization.

Zero-Field Solution

Setting the field to zero will significantly simplify our calculation. The partition function has the expression

$$\mathcal{Z} = \sum_{\{\sigma\}} e^{\beta J \sum_{\langle ij\rangle}\sigma_i\sigma_j} \tag{4.10}$$

Consider the transfer matrix T under zero field

$$T = \begin{bmatrix} e^{\beta J} & e^{-\beta J} \\ e^{-\beta J} & e^{\beta J} \end{bmatrix}. \tag{4.11}$$

In this case the eigenvalues and eigenvectors are

$$\lambda_+ = 2\cosh(\beta J), \tag{4.12}$$

$$\lambda_- = 2\sinh(\beta J), \tag{4.13}$$

$$U = \frac{1}{\sqrt{2}}\begin{bmatrix} 1 & 1 \\ 1 & -1 \end{bmatrix}, \tag{4.14}$$

Note that the eigenvector matrix in this case is exactly the Hadamard matrix. With these expressions of the $\lambda_\pm$, we can then write the partition function as

$$\mathcal{Z} = \lambda_+^N \left(1 + (\lambda_-/\lambda_+)^N\right) = (2\cosh(\beta J))^N \left(1 + \tanh^N(\beta J)\right) \xrightarrow{N\to\infty} (2\cosh(\beta J))^N. \tag{4.15}$$

The single-site magnetization is

$$\langle \sigma_i \rangle = \frac{1}{\mathcal{Z}} \operatorname{Tr}\left(T^N Z_i\right) = \operatorname{Tr}\left(\Lambda^N U Z U^\dagger\right) = \operatorname{Tr}\left(\Lambda^N X\right) = 0, \tag{4.16}$$

since Λ^N is a diagonal matrix and under the permutation of X the trace becomes 0.

Suppose the two spins we are interested in are n sites apart, then

$$\langle \sigma_i \sigma_{i+n} \rangle = \frac{1}{\mathcal{Z}} \operatorname{Tr}\left(Z T^n Z T^{N-n}\right) = \frac{1}{\mathcal{Z}} \operatorname{Tr}\left(\begin{bmatrix} 0 & 1 \\ 1 & 0 \end{bmatrix}\begin{bmatrix} \lambda_+^n & 0 \\ 0 & \lambda_-^n \end{bmatrix}\begin{bmatrix} 0 & 1 \\ 1 & 0 \end{bmatrix}\begin{bmatrix} \lambda_+^{N-n} & 0 \\ 0 & \lambda_-^{N-n} \end{bmatrix}\right) = \frac{\lambda_+^{N-n}\lambda_-^n + \lambda_-^{N-n}\lambda_+^n}{\lambda_+^N + \lambda_-^N} \tag{4.17}$$

As $N \to \infty$,

$$\langle \sigma_i \sigma_{i+n} \rangle \to \frac{\lambda_+^{N-n}\lambda_-^n}{\lambda_+^N} = \left(\frac{\lambda_-}{\lambda_+}\right)^n = \tanh^n(\beta J) \tag{4.18}$$

The correlation length is defined as the quantity ξ that satisfies the equation $\langle \sigma_i \sigma_{i+n} \rangle = e^{-n/\xi}$. From the equation above, we can write down the expression for the correlation length as [37]

$$\boxed{\xi = -\frac{1}{\ln\tanh(\beta J)}}. \tag{4.19}$$

Random-Bond Ising Model

The Hamiltonian of random-bond Ising model (RBIM) in the notation of Ref. [23] is

$$\mathcal{H} = -\sum_{\langle ij \rangle} s_{ij}\sigma_i\sigma_j. \tag{4.20}$$

where s_{ij} is a random variable with the probability distribution

$$p(s_{ij} = +1) = p, \tag{4.21}$$

$$p(s_{ij} = -1) = 1 - p. \tag{4.22}$$

The probablity of each configuration $\{s\}$ is

$$p(\{s\}) = \prod_{\{s\}} p(\{s\}). \tag{4.23}$$

If we define a variable $\beta = \ln[p/(1-p)]/2$, the probability distribution of each s_{ij} in terms of β is

$$p(s = +1) = \frac{e^{\beta}}{2\cosh(\beta)}, \tag{4.24}$$

$$p(s = -1) = \frac{e^{-\beta}}{2\cosh(\beta)}. \tag{4.25}$$

or we can write it as

$$p(s) = \frac{e^{\beta s}}{2\cosh\beta}. \tag{4.26}$$

Suppose there are N_e edges (bonds), the overall probability of a configuration $\boldsymbol{s}$ is

$$p(\boldsymbol{s}) = \prod_{\langle ij \rangle} p(s_{ij}) = \frac{e^{\beta \sum_{\langle ij \rangle} s_{ij}}}{(2\cosh\beta)^{N_e}} \tag{4.27}$$

Suppose we are summing a probability over an observable $O(\boldsymbol{s}, \boldsymbol{\sigma})$. The probability is

$$\langle O \rangle = \sum_{\boldsymbol{s}} p(\boldsymbol{s}) O(\boldsymbol{s}, \boldsymbol{\sigma}) = \frac{1}{(2\cosh\beta)^{N_e}} \sum_{\boldsymbol{s}} e^{\beta \sum_{\langle ij \rangle} s_{ij}} O(\boldsymbol{s}, \boldsymbol{\sigma}). \tag{4.28}$$

Suppose we put gauges $\boldsymbol{\tau} = \{\tau_i\}$ on the vertices and edges, so that

$$s_{ij} \longrightarrow s_{ij}\tau_i\tau_j, \quad \sigma_i = \sigma_i\tau_i. \tag{4.29}$$

If the observable is gauge-invariant, we can resum the expression as

$$\langle O \rangle = \frac{1}{2^{N_v}(2\cosh\beta)^{N_e}} \sum_{\boldsymbol{s}} \sum_{\boldsymbol{\tau}} e^{\beta \sum_{\langle ij \rangle} s_{ij}\tau_i\tau_j} O(\boldsymbol{s}, \boldsymbol{\sigma}). \tag{4.30}$$

Note that here the gauge-symmetrized probability has the expression

$$p(\boldsymbol{s}) = \frac{1}{2^{N_v}(2\cosh\beta)^{N_e}} \sum_{\boldsymbol{\tau}} e^{\beta \sum_{\langle ij \rangle} s_{ij}\tau_i\tau_j}. \tag{4.31}$$

When considering the gauges as spins, this expression exactly looks like a partition function.

The relation that results in this expression of probability

$$\boxed{\beta = \frac{1}{2} \ln \frac{p}{1-p}} \tag{4.32}$$

defines the Nishimori line on the phase diagram of RBIM.

4.2 Molecular Models

The Hamiltonian of a molecule with K nuclei and N electrons is [8]

$$H = -\sum_{i=1}^{N} \frac{\hbar^2}{2m_e} \nabla_i^2 - \sum_{I=1}^{K} \frac{\hbar^2}{2M_I} \nabla_I^2 - \sum_{i=1}^{N} \sum_{I=1}^{K} \frac{e^2}{4\pi\epsilon_0} \frac{Z_I}{|\mathbf{r}_i - \mathbf{R}_I|} \tag{4.33}$$

$$+ \frac{1}{2} \sum_{i \neq j} \frac{e^2}{4\pi\epsilon_0} \frac{1}{|\mathbf{r}_i - \mathbf{r}_j|} + \frac{1}{2} \sum_{I \neq J} \frac{e^2}{4\pi\epsilon_0} \frac{Z_I Z_J}{|\mathbf{R}_I - \mathbf{R}_J|} \tag{4.34}$$

Under the Born-Oppenheimer approximation, we treat the nuclei as classical charges and hence obtain the Hamiltonian only for the electrons in atomic units as:

$$H_e = -\sum_{i=1}^{N} \frac{\nabla_i^2}{2} - \sum_{i=1}^{N} \sum_{I=1}^{K} \frac{Z_I}{|\mathbf{r}_i - \mathbf{R}_I|} + \frac{1}{2} \sum_{i \neq j} \frac{1}{|\mathbf{r}_i - \mathbf{r}_j|}. \tag{4.35}$$

Using Slater determinants to represent the atomic orbitals, we arrive at the second-quantized Hamiltonian

$$H = \sum_{pq} h_{pq} \hat{a}_p^\dagger \hat{a}_q + \frac{1}{2} \sum_{pqrs} h_{pqrs} \hat{a}_p^\dagger \hat{a}_q^\dagger \hat{a}_r \hat{a}_s \tag{4.36}$$

where the one-electron integrals h_{pq} and two-electron integrals h_{pqrs} are

$$h_{pq} = \int d\mathbf{x} \phi_p^*(\mathbf{x}) \left(-\frac{\nabla^2}{2} - \sum_{I=1}^{K} \frac{Z_I}{|\mathbf{r} - \mathbf{R}_I|} \right) \phi_q(\mathbf{x}), \tag{4.37}$$

$$h_{pqrs} = \int d\mathbf{x}_1 d\mathbf{x}_2 \frac{\phi_q^*(\mathbf{x}_1) \phi_q^*(\mathbf{x}_2) \phi_r(\mathbf{x}_2) \phi_s(\mathbf{x}_1)}{|\mathbf{r}_1 - \mathbf{r}_2|}. \tag{4.38}$$

The second-quantized Hamiltonian can be converted to qubit Hamiltonian through qubit encoding methods in Sec. 4.3.

4.3 Qubit Encoding

This section introduces the Jordan-Wigner transformation [38] for encoding fermionic operators into qubit operators.

The one-qubit creation and annihilation operators need to satisfy the relations

$$Q^+ |0\rangle = |1\rangle, Q^+ |1\rangle = 0, \tag{4.39}$$

$$Q^- |0\rangle = 0, Q^- |1\rangle = |0\rangle. \tag{4.40}$$

In matrix notation,

$$Q^+ = \begin{bmatrix} 0 & 0 \\ 1 & 0 \end{bmatrix}, \tag{4.41}$$

$$Q^- = \begin{bmatrix} 0 & 1 \\ 0 & 0 \end{bmatrix}, \tag{4.42}$$

so that $Q^+ = (X - iY)/2, Q^- = (X + iY)/2$.

Some useful relations we will be using later are

$$Q^+ Z = Q^+, \tag{4.43}$$

$$ZQ^- = Q^-. \tag{4.44}$$

To impose fermionic anti-commutation relation, we define

$$\hat{a}_j^\dagger = Z_0 \ldots Z_{j-1} Q_j^+, \tag{4.45}$$

$$\hat{a}_j = Z_0 \ldots Z_{j-1} Q_j^-, \tag{4.46}$$

which is the Jordan-Wigner transformation.

One-body terms

We derive one-body terms in the electronic structure Hamiltonian as an example. The one-body terms in the electronic structure Hamiltonian is

$$\hat{H}_1 = \sum_{ij} h_{ij} \hat{a}_i^\dagger \hat{a}_j = \sum_i h_{ii} \hat{a}_i^\dagger \hat{a}_i + \sum_{i<j} h_{ij} (\hat{a}_i^\dagger \hat{a}_j + \hat{a}_j^\dagger \hat{a}_i). \tag{4.47}$$

The second equality assumes h is real, which is usually the case.

The diagonal terms can be written explicitly as

$$\hat{a}_i^\dagger \hat{a}_i = (Z_0 \ldots Z_{i-1} Q_i^+)(Z_0 \ldots Z_{i-1} Q_i^-) \tag{4.48}$$

$$= \frac{1}{4}(X_i - iY_i)(X_i + iY_i) \tag{4.49}$$

$$= \frac{1}{4}(2I_i + i[X_i, Y_i]) \tag{4.50}$$

$$= \frac{1}{2}(I_i - Z_i). \tag{4.51}$$

The off-diagonal one-body terms are, WLOG $i < j$,

$$\hat{a}_i^\dagger \hat{a}_j = (Q_i^+ Z_i) Z_{i+1} \ldots Z_{j-1} Q_j^- = Q_i^+ Z_{i+1} \ldots Z_{j-1} Q_j^-, \tag{4.52}$$

$$\hat{a}_j^\dagger \hat{a}_i = (Z_i Q_i^-) Z_{i+1} \ldots Z_{j-1} Q_j^+ = Q_i^- Z_{i+1} \ldots Z_{j-1} Q_j^+ \tag{4.53}$$

The sum of these two terms gives

$$\hat{a}_i^\dagger \hat{a}_j + \hat{a}_j^\dagger \hat{a}_i = Q_i^+ Z_{i+1} \ldots Z_{j-1} Q_j^- + Q_i^- Z_{i+1} \ldots Z_{j-1} Q_j^+ \tag{4.54}$$

$$= \frac{1}{4}[(X_i - iY_i) Z_{i+1} \ldots Z_{j-1} (X_j + iY_j) + (X_i + iY_i) Z_{i+1} \ldots Z_{j-1} (X_j - iY_j)] \tag{4.55}$$

$$= \frac{1}{2}(X_i Z_{i+1} \ldots Z_{j-1} X_j + Y_i Z_{i+1} \ldots Z_{j-1} Y_j). \tag{4.56}$$

So the one-body terms can be written in qubit operator form as

$$\hat{H}_1 = \frac{1}{2} \sum_i h_{ii}(I_i - Z_i) + \frac{1}{2} \sum_{i<j} h_{ij}(X_i Z_{i+1} \ldots Z_{j-1} X_j + Y_i Z_{i+1} \ldots Z_{j-1} Y_j) \tag{4.57}$$

Chapter 5

FINITE-TEMPERATURE PROPERTIES OF SPIN MODELS

[1]S.-N. Sun, M. Motta, R. N. Tazhigulov, A. T. Tan, G. K.-L. Chan, and A. J. Minnich, "Quantum Computation of Finite-Temperature Static and Dynamical Properties of Spin Systems Using Quantum Imaginary Time Evolution", PRX Quantum **2**, 010317 (2021),

5.1 Introduction

Quantum computers have long been considered as a potential tool to simulate quantum many-body systems [1, 39, 40]. While near-term quantum devices have made rapid progress in simulating ground-state properties [41–47] and dynamics [30, 31, 48–50], the study of finite-temperature physics on quantum computers is less understood and established [51]. Early works on digital quantum simulation of finite-temperature physical systems involved thermalizing the quantum simulator by coupling to a bath comprised of ancilla qubits [52–54] or sampling thermal states using quantum versions of the Metropolis algorithm [55, 56]. These schemes require prohibitively large numbers of qubits and deep circuits and are hence out of reach for near-term quantum devices.

More practical variational algorithms have been proposed in recent years, such as protocols to construct thermofield double states [57–59] and machine learning-based methods to construct Gibbs states [60–64]. However, the accuracies of these variational schemes depend on the quality of the ansatz. While other non-variational alternatives exist, they are subject to various assumptions. For example, the minimal effective Gibbs ansatz [65] algorithm generates a minimal ensemble of pure states but presumes the eigenstate thermalization hypothesis.

Recently, the quantum imaginary time evolution (QITE) algorithm was introduced [17]. Compared to variational-based algorithms of imaginary time evolution on quantum computers [66–68], QITE is ansatz-independent. The QITE algorithm approximates imaginary time evolution with unitary operators over a domain of qubits and is able to reach the ground states of systems with a few sites. QITE can also be used to calculate finite-temperature quantities, for instance by combining with sampling techniques such as the minimal entangled typical thermal states (METTS) algorithm [69, 70], together denoted as the quantum METTS (QMETTS) algorithm.

However, the original work on QITE [17] focused on the general formalism, while reduction and optimization of quantum resources were not thoroughly investigated. Subsequent development of QITE [71–74] proposed several variations of the original algorithm, but the practical evaluation of finite-temperature properties on existing quantum devices remains largely unaddressed.

Here, we report QITE-based calculations of finite-temperature static and dynamical properties of one-dimensional spin systems with up to four sites on five-qubit IBM Quantum devices. The computed observables include finite-temperature energy, static and dynamical correlation functions, and excitation spectra. These calculations are made possible by several algorithmic improvements. First, we exploit symmetries in the spin Hamiltonians to reduce Pauli strings in the QITE unitaries, thus reducing the overall required quantum resources. Second, circuit optimization procedures including gate decomposition and circuit recompilation are used to further reduce circuit depth. Third, error mitigation techniques, namely post-selection, readout error mitigation and phase-and-scale correction, are used to improve the quality of raw hardware data. Our work demonstrates that with efficient use of quantum resources and effective error mitigation strategies, the ansatz-independent QITE algorithm is capable of computing diverse finite-temperature observables on near-term quantum devices.

This paper is organized as follows. In Sec. 5.2 we review the QITE algorithm and propose a quantum circuit to evaluate finite-temperature dynamical correlation functions. In Sec. 5.3 we introduce the algorithmic improvements including Pauli string reduction, circuit optimization and error mitigation that enabled us to obtain accurate results from hardware. Section 5.4 presents the results of our two-site and four-site calculations. Finally, we conclude and suggest directions for future studies in Sec. 5.5.

5.2 Theory

Quantum imaginary time evolution (QITE)

We begin by reviewing the QITE algorithm in the context of a general Trotterization scheme of the imaginary time propagator. Consider imaginary time evolution on N qubits under a Hamiltonian $\hat{H} = \sum_{m=1}^{M} \hat{h}[m]$, where each $\hat{h}[m]$ acts on a local set of qubits. Since the local terms $\hat{h}[m]$ are not commutative, we need to Trotterize the imaginary time propagator $e^{-\beta\hat{H}}$ by grouping local terms $\hat{h}[m]$ into Trotter terms $\hat{H}[l]$ such that each $\hat{H}[l]$ is a sum of local terms $\hat{h}[m]$ and

$\hat{H} = \sum_{l=1}^{L} \hat{H}[l]$. For example, for a two-local Hamiltonian where each local term $\hat{h}[m]$ acts on qubits $m-1$ and m, setting $L = 2, \hat{H}[1] = \sum_{m=1}^{\lceil M/2 \rceil} \hat{h}[2m-1]$ and $\hat{H}[2] = \sum_{m=1}^{\lfloor M/2 \rfloor} \hat{h}[2m]$ corresponds to the even-odd Trotterization used in one-dimensional tensor network calculations of quantum many-body systems [75]. We consider first-order Trotterization [76] of the full imaginary time propagator $e^{-\beta\hat{H}}$:

$$e^{-\beta\hat{H}} = \left(\prod_{l=1}^{L} e^{-\Delta\tau \hat{H}[l]} \right)^{n_\beta} + O(\Delta\tau^2), \tag{5.1}$$

where n_β is the number of imaginary time steps and $\Delta\tau = \beta/n_\beta$.

The QITE algorithm approximates each imaginary time propagator $e^{-\Delta\tau\hat{H}[l]}$ by a unitary operator

$$e^{-i\Delta\tau\hat{G}[l]} = e^{-i\Delta\tau \sum_\mu x[l]_\mu \sigma_\mu}, \tag{5.2}$$

where $x[l]_{\boldsymbol{\mu}}$ are real coefficients and $\sigma_{\boldsymbol{\mu}}$ are Pauli strings. Here we use the notation $\sigma_0 = I, \sigma_x = X, \sigma_y = Y, \sigma_z = Z$ to denote the identity and the Pauli matrices, so that each Pauli string can be written in the form $\sigma_{\boldsymbol{\mu}} = \bigotimes_{j=0}^{N-1} \sigma_{\mu_j}$ where σ_{μ_j} acts on qubit j and $\mu_j \in \{0, x, y, z\}$. The Pauli strings $\sigma_{\boldsymbol{\mu}}$ are chosen from the set

$$\mathcal{P}_{\hat{H}[l]} = \bigcup_{\hat{h}[m] \in \hat{H}[l]} \mathcal{P}_{\hat{h}[m]}, \tag{5.3}$$

where $\mathcal{P}_{\hat{h}[m]}$ is the set all Pauli strings over a domain of D qubits larger than or equal to the support of $\hat{h}[m]$. To apply the QITE unitaries, without an efficient decomposition scheme each unitary needs to be further Trotterized as

$$e^{-i\Delta\tau\hat{G}[l]} = \prod_{\boldsymbol{\mu}} e^{-i\Delta\tau x[l]_\mu \sigma_\mu} + O(\Delta\tau^2). \tag{5.4}$$

The coefficient vector $\boldsymbol{x[l]}$ is found by minimizing the square of the difference between the unitarily evolved state $e^{-i\Delta\tau\hat{G}[l]} |\Psi\rangle$ and the imaginary-time-evolved state $c[l]^{-1/2} e^{-\Delta\tau\hat{H}[l]} |\Psi\rangle$, where $c[l] = ||e^{-\Delta\tau\hat{H}[l]} |\Psi\rangle||^2$. This minimization results in a linear system

$$\boldsymbol{A[l]x[l] = b[l]}, \tag{5.5}$$

where

$$A[l]_{\boldsymbol{\mu\nu}} = \mathrm{Re}\langle\Psi|\sigma_{\boldsymbol{\mu}}\sigma_{\boldsymbol{\nu}}|\Psi\rangle, \tag{5.6}$$

$$b[l]_{\boldsymbol{\mu}} = \frac{\mathrm{Im}\langle\Psi|e^{-\Delta\tau\hat{H}[l]}\sigma_{\boldsymbol{\mu}}|\Psi\rangle}{\Delta\tau c[l]^{1/2}}. \tag{5.7}$$

In our implementation, we expand the exponential $e^{-\Delta\tau\hat{H}[l]}$ in $\boldsymbol{b[l]}$ and $c[l]$ to second order in $\Delta\tau$:

$$b[l]_\mu = \frac{\mathrm{Im}\langle\Psi|(-\hat{H}[l] + \Delta\tau\hat{H}[l]^2)\sigma_\mu|\Psi\rangle}{c[l]^{1/2}} + O(\Delta\tau^2), \tag{5.8}$$

$$c[l] = \langle\Psi|1 - 2\Delta\tau\hat{H}[l] + 2\Delta\tau^2\hat{H}^2[l]|\Psi\rangle + O(\Delta\tau^3), \tag{5.9}$$

To construct the linear systems, given the terms in Eqs. **??** we measure operators of the form

$$\sigma_\mu\sigma_\nu,\ \hat{H}[l]\sigma_\mu,\ \hat{H}[l]^2\sigma_\mu,\ \hat{H}[l],\ \hat{H}[l]^2. \tag{5.10}$$

The QITE algorithm is carried out by iterating the procedure of constructing the circuit from the QITE unitaries obtained at the previous imaginary time steps, measuring the operators in Eq. 5.10, constructing the linear system in Eq. 5.5, solving for $\boldsymbol{x[l]}$, and propagating the state with the new unitary $e^{-i\Delta\tau\hat{G}[l]}$.

Finite-temperature dynamical correlation functions

Finite-temperature static observables have been previously computed on quantum hardware using the QMETTS algorithm by averaging over the observable evaluated from each METTS sample state [17]. In this work, we show that finite-temperature dynamical observables, in particular finite-temperature dynamical correlation functions, can be computed using a similar averaging procedure as for finite-temperature static observables.

On quantum computers, dynamical correlation functions can be calculated using the circuit reported in Refs. [15, 16]; this circuit has been recently used to compute neutron scattering cross-section [30] and magnon spectra [31] on quantum hardware. To obtain finite-temperature dynamical correlation functions, we insert the QITE circuit into the dynamical correlation function circuit, resulting in the circuit shown in Fig. 5.1. The ancilla qubit is initialized in $|0\rangle$ and the system qubits are initialized in $|\Psi\rangle$. Define $|\Psi(\tau)\rangle = e^{-\tau\hat{H}}|\Psi\rangle / ||e^{-\tau\hat{H}}|\Psi\rangle||$ as the state initialized in $|\Psi\rangle$ and evolved to imaginary time τ, and $|\Phi(\tau)\rangle$ as the QITE-evolved state that approximates $|\Psi(\tau)\rangle$. Let subscript a (s) denote quantities on the ancilla qubit (system qubits). To evaluate finite-temperature observables at an inverse temperature β, we evolve the initial state by QITE to $\beta/2$ so that the joint ancilla-system density operator prior to measurement is

$$\tilde{\rho} = \tilde{U}(I_a \otimes e^{-i\hat{H}t})\tilde{V}(\rho_a \otimes \rho_s)\tilde{V}^\dagger(I_a \otimes e^{i\hat{H}t})\tilde{U}^\dagger, \tag{5.11}$$

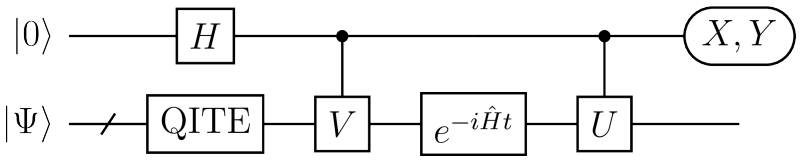

Figure 5.1: Quantum circuit to calculate the finite-temperature dynamical correlation function $\langle U(t)V\rangle_\beta$. The ancilla qubit is initialized in $|0\rangle$ and the system qubit are initialized in $|\Psi\rangle$. Here / denotes a bundle of qubits. Measuring X (Y) on the ancilla yields the real (imaginary) part of $\langle U(t)V\rangle$ on the QITE-evolved initial state. Performing a thermal average over all initial states yields $\langle U(t)V\rangle_\beta$.

where

$$\rho_a = |+\rangle\langle +|, \tag{5.12}$$

$$\rho_s = |\Phi(\beta/2)\rangle\langle\Phi(\beta/2)|, \tag{5.13}$$

and $\tilde{U}$ ($\tilde{V}$) is the controlled-U (controlled-V) gate.

Measuring X (Y) on the ancilla yields the real (imaginary) part of the dynamical correlation function on a single QITE-evolved basis state:

$$\mathrm{Tr}(\tilde{\rho}X_a) = \mathrm{Re}\langle\Phi(\beta/2)|U(t)V|\Phi(\beta/2)\rangle \tag{5.14}$$

$$\mathrm{Tr}(\tilde{\rho}Y_a) = \mathrm{Im}\langle\Phi(\beta/2)|U(t)V|\Phi(\beta/2)\rangle. \tag{5.15}$$

If the initial states are the METTS sample states, an unweighted average over the initial states yields the finite-temperature dynamical correlation function $\langle U(t)V\rangle_\beta$. In this work, we consider trace evaluation in the exact expression of an observable $\hat{O}$ at finite temperature:

$$\langle\hat{O}\rangle_\beta = \frac{\mathrm{Tr}(e^{-\beta\hat{H}}\hat{O})}{\mathrm{Tr}(e^{-\beta\hat{H}})}. \tag{5.16}$$

The numerator trace and the denominator trace are either evaluated by full sampling over the entire Hilbert space, denoted as full trace evaluation, or by random sampling over a subspace of the Hilbert space, denoted as stochastic trace evaluation. If $\hat{O} = U(t)V$, Eq. 5.16 yields the finite-temperature dynamical correlation function $\langle U(t)V\rangle_\beta$. $\hat{O}$ can also be a static observable, in which case Eq. 5.16 yields the static observable at finite temperature.

5.3 Methods

Pauli string reduction by $\mathbb{Z}_2$ symmetries

If we include all 4^D Pauli strings over each domain consisting of D qubits, each QITE unitary $e^{-i\Delta\tau\hat{G}[l]}$ applied as in Eq. 5.4 yields $O(N4^D)$ multi-qubit rotation gates by

the standard rotation gate decomposition [32], which results in a circuit too deep on near-term quantum devices even for $D = 2$. Because of this prohibitive resource overhead, we describe a systematic method to reduce the number of Pauli strings in the QITE unitaries when the Hamiltonian and initial state have $\mathbb{Z}_2$ symmetries.

$\mathbb{Z}_2$ symmetries on qubit Hamiltonians have direct parallels with the stabilizer formalism in quantum error-correcting codes [18]. Suppose the Hamiltonian has d $\mathbb{Z}_2$ symmetries, i.e. $\hat{H}$ commutes with elements of a group isomorphic to $\mathbb{Z}_2^d$ generated independently by d Pauli strings, and the initial state is in the +1 eigenspace of all d generators. If we regard the symmetry group $\mathbb{Z}_2^d$ as the stabilizer $\mathcal{S}$, the symmetry sector of the initial state corresponds to the stabilizer subspace $V_{\mathcal{S}}$.

In stabilizer codes, the normalizer of the stabilizer $\mathcal{N}(\mathcal{S})$ includes all Pauli strings that commute with elements of the stabilizer $\mathcal{S}$, and all valid operations on the code space are in the quotient group $\mathcal{N}(\mathcal{S})/\mathcal{S}$. Intuitively, to preserve $\mathbb{Z}_2$ symmetries, among all Pauli strings from $\mathcal{P}_{\hat{H}[l]}$ the QITE unitaries should only include those from the quotient group $\mathcal{N}(\mathcal{S})/\mathcal{S}$. We now show that the original QITE algorithm subsumes the requirement that the Pauli strings should be chosen from $\mathcal{N}(\mathcal{S})/\mathcal{S}$ because the action of the unitary $e^{-i\Delta\tau\hat{G}[l]}$ with the Pauli strings from the unreduced set $\mathcal{P}_{\hat{H}[l]}$ is the same as the action with Pauli strings from the reduced set $\mathcal{P}_{\hat{H}[l]} \cap \mathcal{N}(\mathcal{S})/\mathcal{S}$. This result is stated as the following proposition, proved and discussed in Appendix **??**.

Proposition 12. Suppose QITE is applied to approximate the imaginary time propagator $e^{-\Delta\tau\hat{H}[l]}$ on the state $|\Psi\rangle$. If there exists a stabilizer $\mathcal{S}$ such that every element of $\mathcal{S}$ commutes with $\hat{H}[l]$ and $|\Psi\rangle \in V_{\mathcal{S}}$, then
(a) The action of $e^{-i\Delta\tau\hat{G}[l]}$ on $|\Psi\rangle$ with $\sigma_{\boldsymbol{\mu}} \in \mathcal{P}_{\hat{H}[l]}$ is equivalent to the action with $\sigma_{\boldsymbol{\mu}} \in \mathcal{P}_{\hat{H}[l]} \cap \mathcal{N}(\mathcal{S})/\mathcal{S}$,
(b) $e^{-i\Delta\tau\hat{G}[l]}|\Psi\rangle \in V_{\mathcal{S}}$.

Further reduction in the number of Pauli strings can be achieved by recalling from Ref. [17] that when the Hamiltonian and the initial state are real in the computational basis, the state after imaginary time evolution must be real. Thus, only Pauli strings with an odd number of Y need to be included in the QITE unitaries. Since $\mathbb{Z}_2$ symmetries and the conditions of a real Hamiltonian and initial state are independent, when both conditions are satisfied, the number of Pauli strings can be reduced using both conditions, in which case the reduced set of Pauli strings is modified to $\mathcal{P}_{\hat{H}[l]} \cap \mathcal{N}(\mathcal{S})/\mathcal{S} \cap \{\sigma_{\boldsymbol{\mu}} : \sum_j \delta_{\mu_j,y} \equiv 1 \pmod 2\}$.

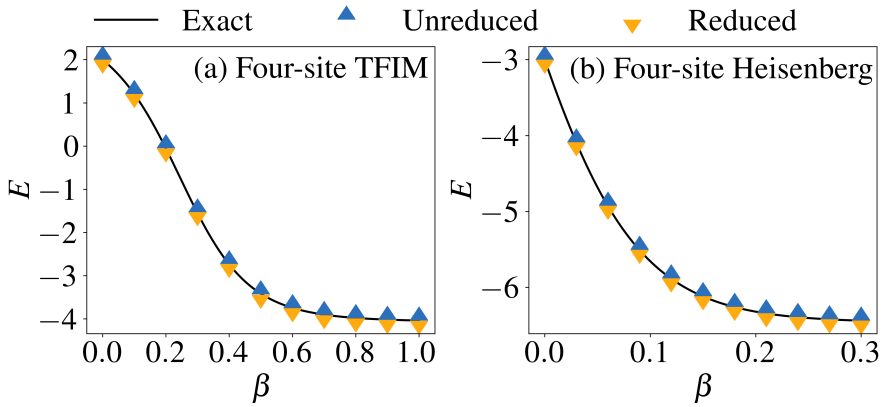

Figure 5.2: Energy E versus imaginary time β simulated without noise or measurement sampling on a single initial state with and without reduction of the Pauli strings in the QITE unitaries by $\mathbb{Z}_2$ symmetries. (a) Four-site TFIM with $J = h = 1$ and initial state $|0001\rangle$. The imaginary time step size in QITE is set to $\Delta\tau = 0.01$. The number of Pauli strings from three $D = 2$ domains is reduced from 16 to 6 by one $\mathbb{Z}_2$ symmetry $Z_0Z_1Z_2Z_3$. (b) Four-site Heisenberg model with $J = \Delta = 1$ and initial state $(|0101\rangle + |1010\rangle)/\sqrt{2}$. The imaginary time step size in QITE is set to $\Delta\tau = 0.03$. The number of Pauli strings on the single $D = 4$ domain is reduced from 120 to 6 by two $\mathbb{Z}_2$ symmetries $Z_0Z_1Z_2Z_3$ and $X_0X_1X_2X_3$. In both panels the energy trajectories using reduced numbers of Pauli strings match the energy trajectories without reduction, which also match the energy trajectories from exact imaginary time evolution.

In practice the Proposition is used inductively on the Trotter terms $\hat{H}[l]$, which implies the stabilizer need to be chosen such that every element of the stabilizer commutes with all $\hat{H}[l]$, or equivalently with $\hat{H}$. For spin Hamiltonians, the stabilizer generators are usually global $\mathbb{Z}_2$ symmetries such as $Z^{\otimes N}$ and $X^{\otimes N}$. For general Hamiltonians, the $\mathbb{Z}_2$ symmetries can be found by Gaussian elimination on the parity check matrix formed from the Hamiltonian terms [77].

To confirm our Pauli string reduction scheme, we compare the QITE energy trajectory as a function of imaginary time simulated without noise or measurement sampling on a single initial state with and without reduction of the Pauli strings in the QITE unitaries by $\mathbb{Z}_2$ symmetries. The Hamiltonians we study include the transverse-field Ising model (TFIM) Hamiltonian

$$\hat{H}_{\text{TFIM}} = J \sum_{i=0}^{N-2} X_i X_{i+1} + h \sum_{i=0}^{N-1} Z_i \tag{5.17}$$

and the Heisenberg XXZ Hamiltonian

$$\hat{H}_{XXZ} = J \sum_{i=0}^{N-2} (X_i X_{i+1} + Y_i Y_{i+1} + \Delta Z_i Z_{i+1}), \tag{5.18}$$

with open boundary conditions assumed for both.

In Fig. 5.2 we plot energy versus imaginary time calculated with QITE on a single initial state. The unreduced set of Pauli strings only includes Pauli strings with odd numbers of Y because the Hamiltonian and initial state are real in the computational basis. We choose a sufficiently small imaginary time step size $\Delta\tau$ to ensure that the Trotter errors from expansion in Eq. 5.4 are negligible. Figure 5.2a plots the energy trajectory for the initial state $|0001\rangle$ in the four-site TFIM with $J = h = 1$. The Hamiltonian and the initial state have a $\mathbb{Z}_2$ symmetry $Z_0Z_1Z_2Z_3$. By combining reduced Pauli strings from all three $D = 2$ domains, we obtain six Pauli strings in the QITE unitaries

$$X_0Y_1, Y_0X_1, X_1Y_2, Y_1X_2, X_2Y_3, Y_2X_3, \tag{5.19}$$

compared to 16 Pauli strings without reduction by $\mathbb{Z}_2$ symmetries. Figure 5.2b plots energy versus imaginary time of the initial state $(|0101\rangle + |1010\rangle)/\sqrt{2}$ on the four-site Heisenberg model with $J = \Delta = 1$. The Hamiltonian and the initial state have two $\mathbb{Z}_2$ symmetries $Z_0Z_1Z_2Z_3$ and $X_0X_1X_2X_3$. The 120 Pauli strings in the QITE unitaries without reduction is reduced to the 6 Pauli strings

$$X_0Y_1Z_2, X_0Z_1Y_2, Y_0X_1Z_2, Y_0Z_1X_2, Z_0X_1Y_2, Z_0Y_1X_2. \tag{5.20}$$

In both panels of Fig. 5.2, the energy trajectories using reduced numbers of Pauli strings match the energy trajectories without reduction, which also match the energy trajectories from exact imaginary time evolution.

Circuit optimization

Even with reduction of Pauli strings in the QITE unitaries by $\mathbb{Z}_2$ symmetries, applying the QITE unitaries as in Eq. 5.4 may still result in a circuit too deep to be implemented on current quantum hardware. In this section we describe circuit optimization techniques that further reduce circuit depth.

In two-site calculations, both the QITE circuit and the real time evolution circuit can be optimized to constant depth with a standard one- and two-qubit gate set, regardless of the number of imaginary and real time steps. For example, in two-site TFIM there is only one Pauli string X_0Y_1 in the QITE unitaries after reduction

by the $\mathbb{Z}_2$ symmetry Z_0Z_1. Suppose the unitary applied to the state at the k-th imaginary time step is $e^{-i\Delta\tau x_k X_0 Y_1}$. Then the unitaries at all imaginary time steps can be multiplied into a single two-qubit rotation gate $e^{-i\theta X_0 Y_1/2}$ where $\theta = 2\Delta\tau \sum_k x_k$. For real time evolution, the two-qubit operator $e^{-i\hat{H}t}$ is decomposed by the KAK decomposition [78–81] into six single-qubit gates and two CNOT gates.

In four-site calculations, neither the QITE circuit nor the real time evolution circuit is of constant depth. If we Trotterize the QITE unitaries as in Eq. 5.4 and similarly for the real time propagator, the circuit is too deep to be accurately implemented on existing quantum devices. Therefore, we recompile the circuit by fitting each QITE unitary $e^{-i\Delta\tau\hat{G}[l]}$ or the real time propagator $e^{-i\hat{H}t}$ to a parametrized circuit [82–84] using an open-source tensor network-based quantum simulation library [85]. Figure 5.3a shows the recompiled four-site QITE circuit, where the U_3 gate is a generic single-qubit gate defined as

$$U_3(\theta,\phi,\lambda) = \begin{pmatrix} \cos(\theta/2) & -e^{i\lambda}\sin(\theta/2) \\ e^{i\phi}\sin(\theta/2) & e^{i(\lambda+\phi)}\cos(\theta/2) \end{pmatrix}. \tag{5.21}$$

The four U_3 gates at the left constitute the base gate round. Each additional gate round consists of a layer of CNOT gates and a layer of single-qubit gates. The additional gate rounds alternate between even-odd and odd-even pairs of qubits. Let the target unitary be U_{targ} and the recompiled unitary be $U_{\text{rec}}(\boldsymbol{\theta})$, where $\boldsymbol{\theta}$ is a composite variable denoting all the angles. Given a reduced density operator ρ on the finite domain acted on by the target unitary, the optimal recompiled unitary is found by performing a gradient descent to maximize the function

$$F(\boldsymbol{\theta}) = \left|\text{Tr}(U_{\text{rec}}(\boldsymbol{\theta})^\dagger U_{\text{targ}}\rho)\right|^2, \tag{5.22}$$

which can be interpreted as the fidelity between $U_{\text{rec}}(\boldsymbol{\theta})$ and U_{targ} with respect to the reduced density matrix ρ. Since the QITE unitaries are real, we use the one-parameter single-qubit gate $R_y(\theta) = U_3(\theta, 0, 0)$ in the recompiled circuit for QITE, while for real time evolution we keep the U_3 gate as the parametrized single-qubit gate.

In Fig. 5.3b, we examine how recompilation affects observable values by simulating the finite-temperature energy $\langle E\rangle_\beta$ of the four-site TFIM with $J = 3$, $h = 1$ in the absence of noise or measurement sampling. Both the $D = 2$ and the $D = 4$ QITE unitaries are recompiled with three gate rounds, resulting in a circuit of the same form as that shown in Fig. 5.3a. For both $D = 2$ and $D = 4$, the average recompilation

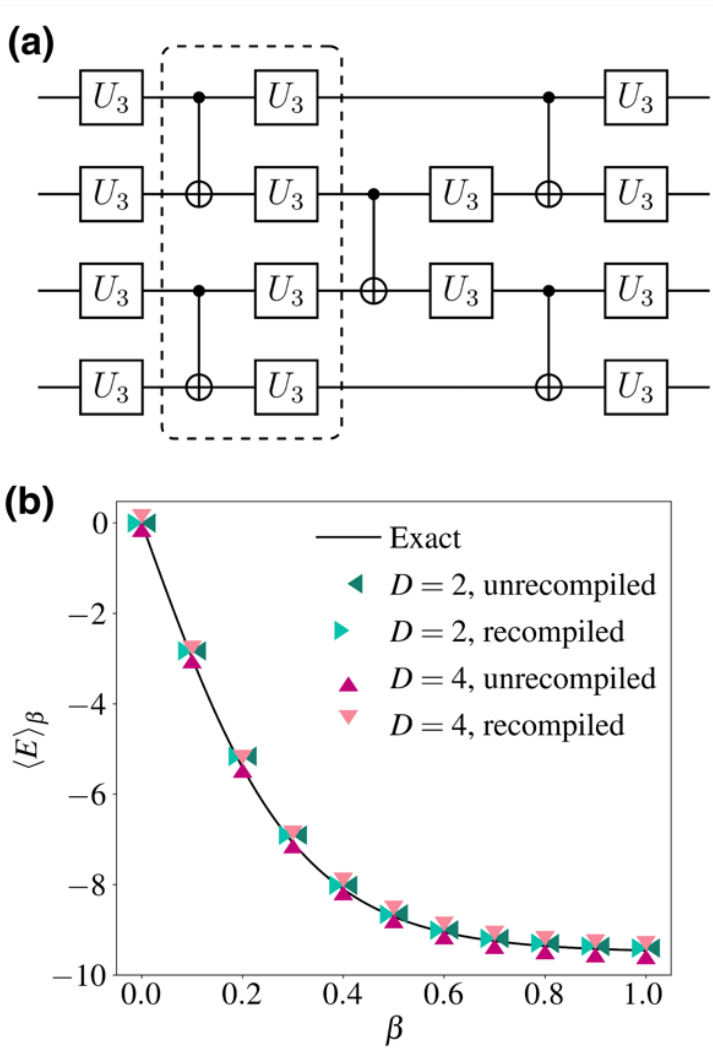

Figure 5.3: (a) Four-site recompiled circuit. The four U_3 gates at the left constitute the base gate round. Each additional gate round includes a layer of CNOT gates and a layer of single-qubit gates as shown in the dashed box. The additional gate rounds alternate between even-odd and odd-even pairs of qubits, so that the circuit shown consists of three gate rounds. (b) Comparison of the finite-temperature energy $\langle E \rangle_\beta$ of the four-site TFIM with $J = 3, h = 1$ with and without recompilation in the absence of noise and measurement sampling. The imaginary time step size in QITE is $\Delta\tau = 0.05$. For both $D = 2$ and $D = 4$, the observable values from the recompiled QITE unitaries are within 0.1% of those from the unrecompiled QITE unitaries.

fidelity defined in Eq. 5.22 is above 0.9999, and the observable values from the recompiled QITE unitaries are within 0.1% of those from the unrecompiled QITE unitaries. The observable values from QITE are also close to the exact values, which is expected from a noiseless simulation.

Error mitigation

To mitigate the effect of hardware noise on the measurement results, we post-process our hardware data by error mitigation methods including post-selection, readout error mitigation and phase-and-scale correction. Post-selection and readout error mitigation are applied to the measurement outcomes at each imaginary time step in the QITE subroutine; phase-and-scale correction is applied to the final computed finite-temperature dynamical correlation function as a single-step post-processing. Richardson extrapolation to the zero-noise limit on short-depth circuits [86] as recently implemented in QITE [71] was also carried out; however, it was not observed to further improve the results and hence was not applied in our calculations.

Post-selection is performed on $\mathbb{Z}_2$ symmetries discussed in Sec. 5.3. When the Hamiltonian and the initial state have $\mathbb{Z}_2$ symmetries, the final state after imaginary or real time evolution should have the same stabilizer parities as the initial state. However, during execution of the circuit, gate errors and qubit decoherence can induce nonzero overlap of the qubit state with the subspace of the wrong parity. Post-selection can mitigate these undesirable effects by discarding measurement outcomes with the wrong parity [87, 88].

We specifically consider the symmetry from a single stabilizer generator. If the operator to be measured is an ancilla operator, we can simply measure the stabilizer generator on all the system qubits and read off the parity without interfering with measurement of the ancilla. If the operator to be measured acts on system qubits,

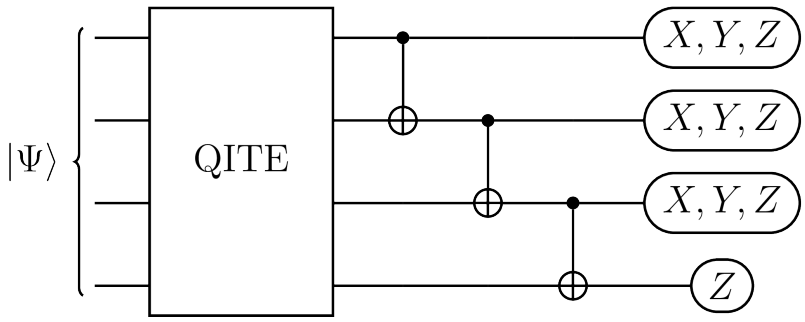

Figure 5.4: Measurement of a Pauli string in a four-site QITE calculation with post-selection on the stabilizer generator $Z_0Z_1Z_2Z_3$. The appended CNOT gates achieve simultaneous measurement of the Pauli string with the stabilizer generator by transforming $Z_0Z_1Z_2Z_3$ to Z_3 acting on a single qubit, from which the stabilizer parity is read off. The other qubits are measured in X-, Y- or Z-basis depending on the Pauli string measured. Measurement outcomes with the wrong parity are discarded.

we need to simultaneously measure the operator and the stabilizer generator, which is possible because all operators in Eq. 5.10 commute with the stabilizer generator by our choice of Pauli strings in the QITE unitaries in Sec. 5.3. Specifically, each operator and the stabilizer generator can be simultaneously measured by using Clifford gates to transform the Pauli string components of the operator and the stabilizer generator until they are qubit-wise commuting, so that their expectation values can be read off on different qubits [89–92].

Figure 5.4 shows the circuit to simultaneously measure the stabilizer generator $Z_0Z_1Z_2Z_3$ and a Pauli string that commutes with it in a four-site QITE calculation. The sequence of CNOT gates after the QITE circuit in Fig. 5.4 transforms $Z_0Z_1Z_2Z_3$ to Z_3. Since Z_3 acts on a single qubit, it necessarily qubit-wise commutes with the transformed Pauli string. In practice, we stop applying CNOT gates when the transformed Pauli string becomes qubit-wise commuting with the transformed stabilizer generator, and therefore the number of CNOT gates added to the end of the circuit ranges from zero to three.

To account for noise in the final measurement, the built-in readout error mitigation routine in Qiskit [93] is applied to each measurement outcome. Because of the small size of the systems we study, for N qubits we carry out full calibration on all 2^N initial states. Application of the inverse of the calibration matrix to the raw measurement counts is performed by the default least-square fitting method.

We assess the effectiveness of applying post-selection and readout error mitigation at every imaginary step of QITE by simulating the finite-temperature energy of two-site and four-site TFIMs using full trace evaluation with measurement sampling and the noise model from *ibmq_rome*. In both panels of Fig. 5.5, QITE is applied with Pauli strings reduced and circuits optimized. In particular, four-site QITE unitaries are of domain size $D = 2$ and recompiled with three rounds of gates. From Fig. 5.5 we can see that both readout error mitigation and post-selection shift the raw data toward the exact data, confirming the effectiveness of both schemes in reducing the effect of noise. Furthermore, a combination of readout error mitigation and post-selection is observed to be most effective in mitigating the errors, which is not apparent on two sites in Fig. 5.5a presumably because of the small size of the system but clearly evident on four sites in Fig. 5.5b.

In calculations of finite-temperature dynamical correlation functions, the ancilla qubit is in the state $|+\rangle$ before entangling with the system qubits. When there is a long sequence of gates in the real time propagator $e^{-i\hat{H}t}$, decoherence of the ancilla

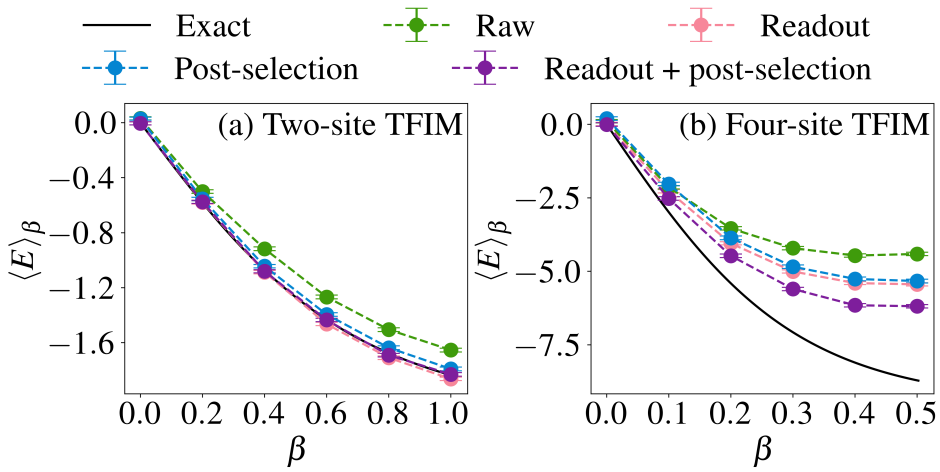

Figure 5.5: Finite-temperature energy $\langle E \rangle_\beta$ of (a) the two-site TFIM with $J = h = 1$ and (b) the four-site TFIM with $J = 3$, $h = 1$, simulated with measurement sampling and the noise model from *ibmq_rome*. The imaginary time step size in QITE is $\Delta\tau = 0.1$ for two-site TFIM and $\Delta\tau = 0.05$ for four-site TFIM. Raw data are post-processed at each imaginary time step with either readout error mitigation, or post-selection, or both. Employing both readout error mitigation and post-selection is observed to be most effective in mitigating the errors.

qubit such as amplitude damping to the qubit ground state $|0\rangle$ and depolarization will significantly affect the X and Y measurement results on the ancilla. To mitigate the effect of ancilla decoherence, we apply phase-and-scale correction [30, 31] as a single-step post-processing to the result at the end of the calculation. The only finite-temperature dynamical correlation function considered in this work is $\langle Z_0(t)Z_0 \rangle_\beta$, which is equal to 1 analytically at $t = 0$. Hence, we apply phase-and-scale correction by dividing the raw hardware $\langle Z_0(t)Z_0 \rangle_\beta$ at each t by the raw hardware $\langle Z_0(t = 0)Z_0 \rangle_\beta$ to enforce the condition $\langle Z_0(t = 0)Z_0 \rangle_\beta = 1$.

In addition, Richardson extrapolation on the noise parameters [55] as recently implemented in QITE has been attempted in the current project. However, it did not improve the results on top of the error mitigation methods we already have, and hence are not applied in our calculations. has been proposed as a promising method in extrapolating out gate errors. However, in our two-site calculations, the three error mitigation methods above already produced results good enough on the constant-depth circuits and thus eliminate the necessity of applying Richardson extrapolation. In our four-site calculations, where the circuits are not of constant depth, the main source of the error is likely to be qubit decoherence resulting from deep circuit rather than gate errors. Moreover, applying Richardson extrapolation by repeating gates [71] result in circuits with more than 200 layers of gates, which

are too deep to yield meaningful results on near-term devices. Consequently, we do not apply Richardson extrapolation in our calculations.

5.4 Results

Experiments of computing finite-temperature observables were conducted on IBM Quantum devices *ibmq_bogota* and *ibmq_rome* [94], both of which consist of five qubits arranged on a chain with nearest-neighbor interactions and similar error rates. IBM's open-source library Qiskit [95] was used to implement our algorithms on the devices. In each calculation, the N system qubits $0, \ldots, N-1$ are arranged adjacent to each other and the ancilla is closest to system qubit 0.

The systems we study are sufficiently small that we apply QITE to approximate the full imaginary time propagator $e^{-\Delta\tau\hat{H}}$ at each imaginary time step, which is equivalent to setting $L = 1$ and $\hat{H}[1] = \hat{H}$ in Eq. 5.1. The QITE linear systems in Eq. 5.5 are solved by a conjugate gradient method. Because hardware noise and measurement sampling lead to ill-conditioned $\boldsymbol{A}$ matrices in the QITE linear systems, we add a regularizer of 0.2 to the diagonal elements of each $\boldsymbol{A}$ matrix in the four-site calculations.

Each calibration circuit used for readout error mitigation is repeated 1000 times; each Pauli string measurement circuit used to construct the QITE linear systems is repeated 8000 times. Error bars from full trace evaluation result only from measurement sampling and are the size of the markers in most figures; error bars from stochastic trace evaluation originate from both measurement sampling and initial state sampling. A detailed description of error bars in full and stochastic trace evaluation is given in Appendix B.

Two-site calculations

We study the two-site TFIM defined in Eq. 5.17 by setting $h = 1$ and varying J. The finite-temperature energy $\langle E\rangle_\beta$ and static correlation function $\langle X_0X_1\rangle_\beta$ are calculated on the Hamiltonians with $J = \pm 1, \pm 3$, while the finite-temperature dynamical correlation function $\langle Z_0(t)Z_0\rangle_\beta$ and excitation spectra are calculated on the Hamiltonian with $J = 3$. In all calculations, finite-temperature observables are calculated by full trace evaluation and the circuits are optimized according to the circuit optimization procedures in Sec. 5.3.

Figure 5.6 shows the finite-temperature energy $\langle E\rangle_\beta$ and static correlation function $\langle X_0X_1\rangle_\beta$ of the two-site TFIM with $J = \pm 1, \pm 3$ from $\beta = 0$ to $\beta = 2$. In both 5.6a

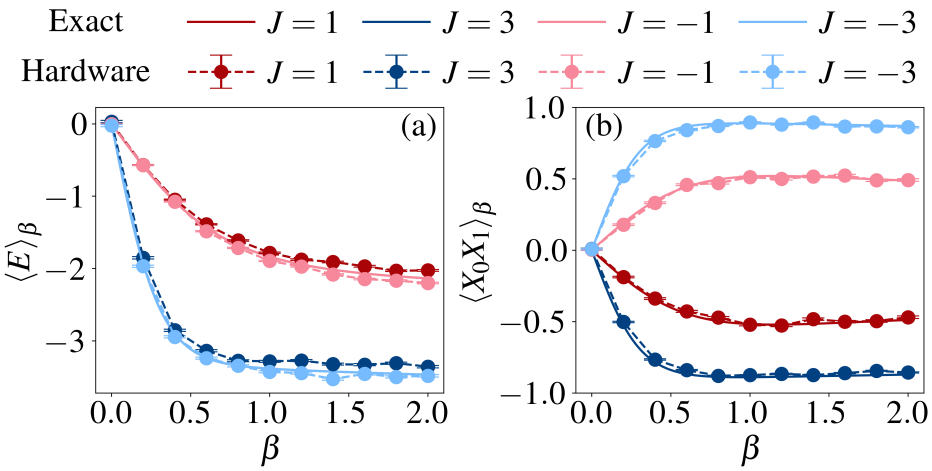

Figure 5.6: (a) Finite-temperature energy $\langle E\rangle_\beta$ and (b) static correlation function $\langle X_0X_1\rangle_\beta$ of the two-site TFIM with $J = \pm 1, \pm 3$ and $h = 1$ versus inverse temperature β. The imaginary time step size in QITE is $\Delta\tau = 0.1$. The observables obtained on hardware are within 1-4% of the exact values.

and 5.6b the finite-temperature observables obtained on hardware are within 1% to 4% of the exact values. Further, if we regard each finite-temperature variable as a function of J, analytically it can be shown that $\langle E\rangle_\beta(J) = \langle E\rangle_\beta(-J)$ and $\langle X_0X_1\rangle_\beta(J) = -\langle X_0X_1\rangle_\beta(-J)$. This relation is satisfied in the hardware data.

Next, finite-temperature dynamical properties were calculated on the two-site TFIM with $J = 3, h = 1$. The dynamical correlation function $\langle Z_0(t)Z_0\rangle_\beta$ is evaluated from $\beta = 0$ to $\beta = 2$ and at real time from $t = 0$ to $t = 8\pi$. Figures 5.7a and 5.7b show the real and imaginary parts of $\langle Z_0(t)Z_0\rangle_\beta$ at $\beta = 0.2$ and $\beta = 1.8$ up to $t = 4\pi$. From **??** we see that even without phase-and-scale correction, the real and imaginary parts of $\langle Z_0(t)Z_0\rangle_\beta$ agree well with the exact results at both small and large β, presumably due to the constant and shallow depth of the real time evolution circuit.

The spectral density $S(\omega)$ is obtained by a discrete Fourier transform of the dynamical correlation function $\langle Z_0(t)Z_0\rangle_\beta$. Specifically, at each β

$$S(\omega_k) = \frac{1}{n_t}\sum_{m=0}^{n_t-1}\langle Z_0(t_m)Z_0\rangle_\beta\, e^{i\omega_k t_m}, \tag{5.23}$$

where n_t is the total number of points in the time series, $t_m = m\Delta t$, and $\omega_k = 2\pi k/n_t\Delta t$. With this definition of Fourier transform, the peaks at positive (negative) frequencies correspond to emissions (absorptions) of excitations of the system.

To analyze the evolution of the excitation spectra across different temperatures, we plot the amplitudes at the two emission frequencies versus β in Fig. 5.7d.

Analytically, the amplitude of the transition from an initial state $|\Psi_i\rangle$ to a final state $|\Psi_f\rangle$ is $e^{-\beta E_f}|\langle\Psi_i|Z_0|\Psi_f\rangle|^2/\mathcal{Z}$, where E_f is the energy of the final state and $\mathcal{Z}$ is the partition function. In the two-site TFIM, the only allowed transitions are between the two states in each of the two-dimensional eigenspaces of Z_0Z_1 with eigenvalues ±1. The frequency ±7.18 corresponds to a transition in the $+1$ eigenspace, where the ground state lies, and the frequency ±5.94 corresponds to a transition in the -1 eigenspace, where the first excited state lies. As the temperature decreases from infinite temperature (β increases from 0), the populations in the two lowest states first increase until the ground state population dominates

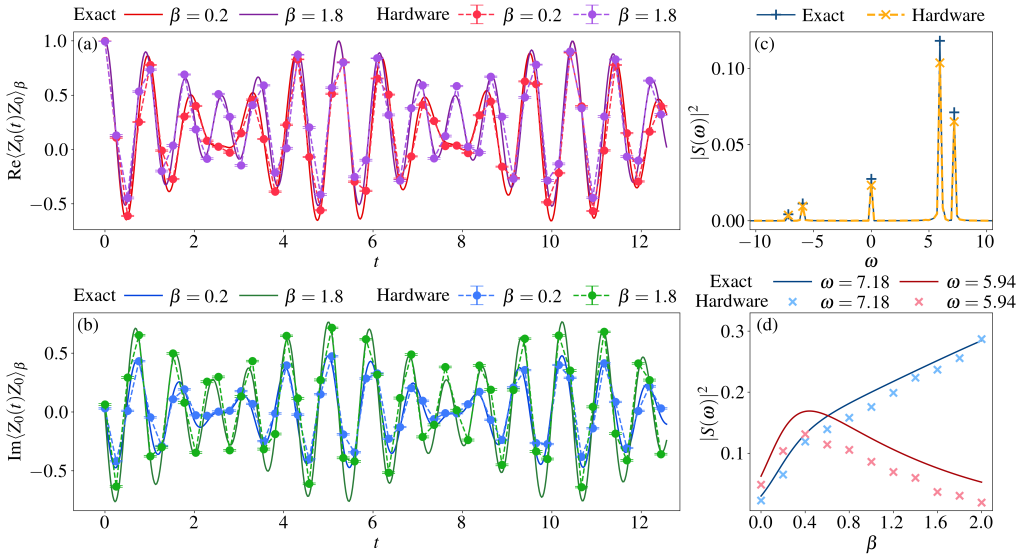

Figure 5.7: Finite-temperature dynamical properties of the two-site TFIM with $J = 3$, $h = 1$. The imaginary time step size in QITE is set to $\Delta\tau = 0.1$. (a) Real and (b) imaginary parts of the finite-temperature dynamical correlation function $\langle Z_0(t)Z_0\rangle_\beta$ at $\beta = 0.2$ and $\beta = 1.8$ versus real time t. (c) Finite-temperature excitation spectra $|S(\omega)|^2$ versus frequency ω. Positive (negative) frequencies correspond to emissions (absorptions). (d) Amplitudes of the two emission peaks at $\omega = 7.18$ and $\omega = 5.94$. The hardware data capture finite-temperature dynamics of two-site TFIM across a wide range of temperatures.

over that of the first excited state at around $\beta = 0.4$, a trend reproduced by the amplitudes obtained from hardware data in 5.7d. Thus, 5.7 shows that quantum hardware accurately captures the finite-temperature dynamics of the two-site TFIM across a wide range of temperatures.

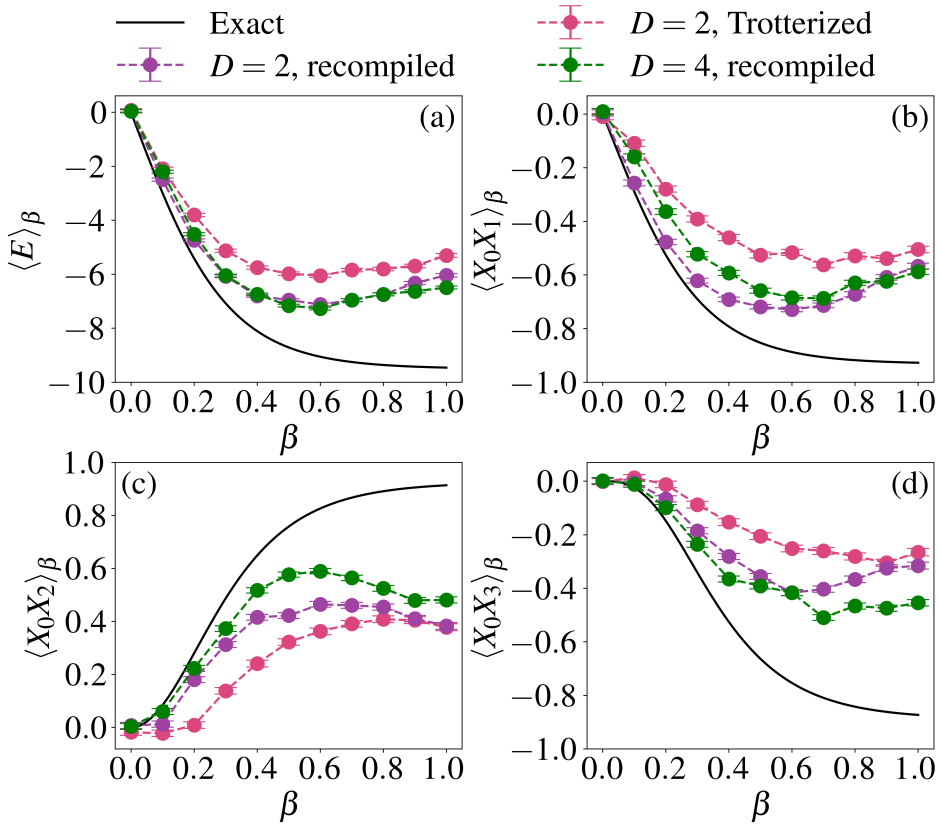

Figure 5.8: (a) Finite-temperature energy $\langle E \rangle_\beta$ and static correlation functions (b) $\langle X_0X_1 \rangle_\beta$ (c) $\langle X_0X_2 \rangle_\beta$ (d) $\langle X_0X_3 \rangle_\beta$ of the four-site TFIM with $J = 3, h = 1$ versus inverse temperature β with different QITE unitaries. The imaginary time step size in QITE is set to $\Delta\tau = 0.05$. The $D = 2$ QITE unitaries are either Trotterized as in 5.4 or recompiled, while all $D = 4$ QITE unitaries are recompiled. The results with recompiled QITE unitaries are closer to exact results than the results with Trotterized QITE unitaries due to circuit depth. Between the calculations with recompiled unitaries, $D = 4$ is not necessarily closer to exact results than $D = 2$ for all observables possibly due to the increased influence of hardware noise in the larger linear systems.

Four-site calculations

We next proceed to four-site spin systems. We study the four-site TFIM defined in Eq. 5.17 with $J = 3, h = 1$. Full trace evaluation is employed unless otherwise specified.

First, let us consider gate counts in the four-site circuits. For the four-site TFIM with $D = 2$, after reduction by the $\mathbb{Z}_2$ symmetry $Z_0Z_1Z_2Z_3$ there are six weight-two Pauli strings, which are the ones given in Eq. 5.19. If we Trotterize the QITE unitaries as in Eq. 5.4, each unitary requires 12 CNOT gates by the standard rotation gate decomposition [32], which becomes unfeasible on near-term quantum hardware

after the first few imaginary time steps. When $D = 4$, even after reduction by one $\mathbb{Z}_2$ symmetry there are still 28 Pauli strings in each QITE unitary. After Trotterization and rotation gate decomposition, each QITE unitary requires more than 50 CNOT gates for a single imaginary time step. Hence, when $D = 2$, we compute finite-temperature observables both by Trotterizing and by recompiling the QITE unitaries with three gate rounds; when $D = 4$, we only recompile the QITE unitaries with three gate rounds. To obtain dynamical correlation functions, we additionally recompile the real time propagator $e^{-i\hat{H}t}$ with five gate rounds. The number of gate rounds is chosen so that the fidelity as defined in 5.22 is at least 0.999 on average in each calculation.

Figure 5.8 shows the finite-temperature energy $\langle E \rangle_\beta$ and static correlation functions $\langle X_0 X_1 \rangle_\beta$, $\langle X_0 X_2 \rangle_\beta$, $\langle X_0 X_3 \rangle_\beta$ of the four-site TFIM. From the figure, we can see that the finite-temperature observables calculated with Trotterized $D = 2$ QITE unitaries deviate from those calculated with $D = 2$ recompiled QITE unitaries or $D = 4$ recompiled QITE unitaries after $\beta = 0.1$. This deviation is due to the deep circuit resulting from 12 layers of CNOT gates per imaginary time step, compared to 3 layers of CNOT gates per imaginary time step in the recompiled circuit. The observables from $D = 2$ recompiled QITE unitaries are in reasonable agreement with those from $D = 4$ recompiled QITE unitaries for all β, which is consistent with the simulator results in the absence of noise or measurement sampling in Fig. 5.3b. However, even the recompiled QITE unitaries are not able to track the exact finite-temperature observables for $\beta \gtrsim 0.4$. In particular, the slope is reversed compared to the exact result for $\beta > 0.5$. QITE up to $\beta = 0.5$ corresponds to 5 imaginary time steps and hence 15 layers of CNOT gates, which is almost at the limit of circuit depth on these quantum devices.

To explore the scalability of our approach, we compare stochastic trace evaluation with full trace evaluation in calculating the finite-temperature energy of the four-site TFIM. Stochastic trace evaluation is performed by uniformly selecting initial states in the full trace evaluation result with recompiled $D = 2$ QITE unitaries. In Fig. 5.9, we plot the stochastic trace evaluation results with 10 and 20 samples along with the full trace evaluation and exact results; the inset shows the running average of $\langle E \rangle_\beta$ versus number of samples n_{samples}. As can be seen from the figure, random sampling with 10 samples already reproduced the results from full sampling on all 16 initial states, indicating that using scalable sampling schemes is a promising approach to studying larger systems.

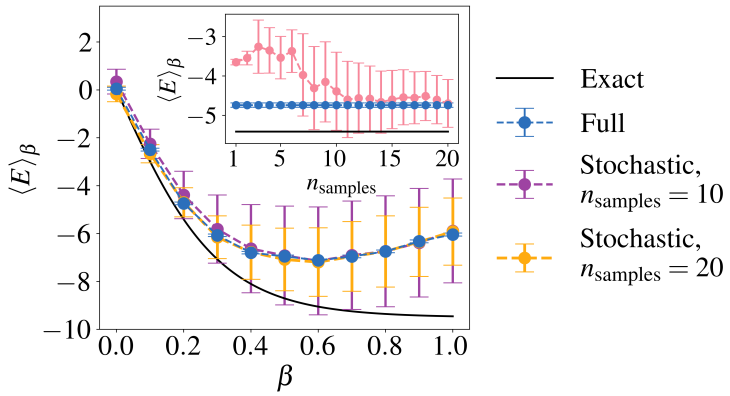

Figure 5.9: Finite-temperature energy $\langle E \rangle_\beta$ of the four-site TFIM with $J = 3, h = 1$ versus inverse temperature β using full and stochastic trace evaluation. QITE is performed with recompiled $D = 2$ unitaries with a time step of $\Delta\tau = 0.05$. Results of stochastic trace evaluation are shown with number of samples n_{samples} set to 10 and 20. Inset shows the running average of $\langle E \rangle_\beta$ versus n_{samples} using stochastic trace evaluation at $\beta = 0.2$ (red symbols), with full trace evaluation (blue symbols) and exact results (black solid line) plotted as constant values. Stochastic trace evaluation with 10 samples is already sufficient to reproduce the results from full trace evaluation across a wide range of β.

Finally, in Fig. 5.10 we show the dynamical properties of the four-site TFIM with $J = 3, h = 1$ at $\beta = 0.2$. The calculation is implemented by recompiling $D = 2$ QITE unitaries with three gate rounds and real time propagation with five gate rounds. Figure 5.10a shows the real and imaginary parts of $\langle Z_0(t)Z_0 \rangle_\beta$ after phase-and-scale correction. With this correction, both the real and the imaginary parts show good agreement with the exact result. Figure 5.10b shows the excitation spectra obtained by Fourier transforming the exact and phase-and-scale-corrected hardware $\langle Z_0(t)Z_0 \rangle_\beta$ at the same points in real time. The excitation spectrum from hardware data accurately reproduces not only the frequencies $\omega = 0, \pm 4.90, \pm 6.37, \pm 7.84$ but also the peak amplitudes.

The favorable agreement of the hardware $\langle Z_0(t)Z_0 \rangle_\beta$ with the exact result is in contrast with the deviation of finite-temperature static observables from the exact values in Fig. 5.8. In fact, the raw hardware $\langle Z_0(t)Z_0 \rangle_\beta$ at $t = 0$ is $0.821 + 0.397i$, which is far from the exact value 1, indicating that the phase-and-scale correction has a significant effect in correcting raw hardware data. Although in Ref. [31] a phase-and-scale correction combined with readout error mitigation was not observed to yield as large an improvement as we see in our hardware data, the use of post-selection before the phase-and-scale correction in our implementation

may be responsible for some of the improvement relative to exact results.

Even though the phase does not enter the static observables we computed, the lack of a scale correction scheme for the static observables may explain their large deviation from the exact values compared to dynamical observables. Moreover, even though the recompiled circuit in Fig. 5.10 includes up to 11 gate rounds with the QITE and real time evolution gates combined, the ancilla is initialized after the QITE circuit and hence only experiences 5 gate rounds prior to measurement. The relatively shallow circuit applied to the ancilla may be another reason for the good performance of the quantum device for calculating the finite-temperature dynamical observable $\langle Z_0(t)Z_0\rangle_\beta$.

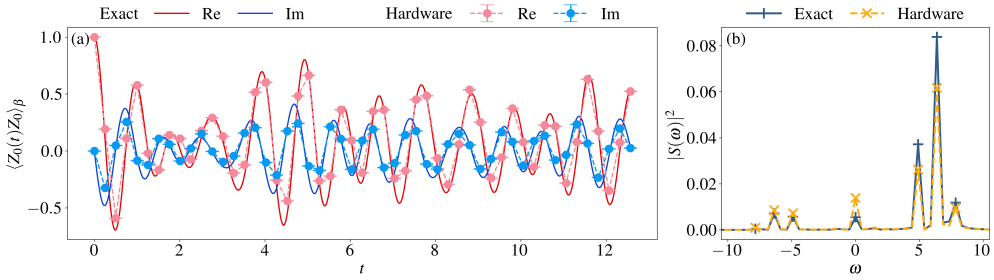

Figure 5.10: Finite-temperature dynamical properties of the four-site TFIM with $J = 3, h = 1$ at $\beta = 0.2$. QITE is performed with a time step of $\Delta\tau = 0.05$ and recompiled $D = 2$ unitaries. (a) Real and imaginary parts of the finite-temperature dynamical correlation function $\langle Z_0(t)Z_0\rangle_\beta$ versus real time t. Raw hardware data are post-processed by phase-and-scale correction. (b) Finite-temperature excitation spectra obtained by Fourier transform of exact and phase-and-scale-corrected hardware $\langle Z_0(t)Z_0\rangle_\beta$ at the same points in real time. The hardware $\langle Z_0(t)Z_0\rangle_\beta$ and excitation spectrum after phase-and-scale correction are in good agreement with the exact results.

5.5 Conclusion and Outlook

Our work demonstrates that finite-temperature physics of quantum spin systems is accessible with near-term quantum hardware and paves the way for further study of finite-temperature phenomena on near-term quantum devices. With methods to reduce required quantum resources and mitigate errors in raw hardware data, QITE enables the practical calculation of finite-temperature energy, static and dynamical correlation functions, and spectral densities of excitations.

On two sites, static and dynamical observables for a wide range of temperatures are accurately captured by quantum hardware. An important factor underlying this

accuracy is the constant depth of the circuit in both QITE and real time evolution. Constant depth in QITE allowed us to extend QITE-based finite-temperature calculations from a single site [17]; constant depth in real time evolution allowed us to reproduce exact finite-temperature dynamical correlation functions on quantum hardware without phase-and-scale correction as compared to previous studies [30, 31].

On four sites, finite-temperature static observables calculated on quantum hardware with circuit recompilation are in reasonable agreement with exact results at $\beta \leq 0.5$. We were also able to accurately reproduce the finite-temperature dynamical correlation function using phase-and-scale correction at a high temperature $\beta \sim 0.2$. However, accurate determination of observables at lower temperatures still appears challenging using the current recompilation scheme where the QITE unitaries are recompiled separately at each imaginary time step. Therefore, simulating quantum systems at low temperature on near-term quantum computers will likely require additional reduction of circuit depth such as recompilation with merged imaginary time steps [73] or lower error rates on quantum devices either from efficient error mitigation for imaginary time or from improvements in hardware.

To simulate larger systems, more qubits, deeper circuits, and a scalable method for performing thermal averages are required. Since the main limitation in our four-site calculations is circuit depth rather than system size, simulation of larger systems will likely require more aggressive recompilation techniques. However, this recompilation is scalable as the fidelity defined in Eq. 5.22 is evaluated on the reduced density matrix. To investigate the scalability of the method to calculate thermal averages, we examined how stochastic trace evaluation performs in calculating finite-temperature observables compared to full trace evaluation. We found that on four sites stochastic trace evaluation reproduced full trace evaluation results accurately in the temperature regime we studied. Compared to the previously proposed QMETTS algorithm, stochastic trace evaluation has zero autocorrelation time. A detailed comparison of QITE-based computation of finite-temperature observables with different sampling schemes is a topic worth exploring. Furthermore, with the availability of more qubits [28, 96], trading increased computational time due to sampling for an increased number of qubits via constructing density matrix purification states [57–59] may be another feasible direction for studying finite-temperature physics on near-term quantum hardware.

Chapter 6

FREQUENCY-DOMAIN RESPONSE PROPERTIES OF DIATOMIC MOLECULES

[1]S.-N. Sun, B. Marinelli, J. M. Koh, Y. Kim, L. B. Nguyen, L. Chen, J. M. Kreikebaum, D. I. Santiago, I. Siddiqi, and A. J. Minnich, "Quantum computation of frequency-domain molecular response properties using a three-qubit iToffoli gate", npj Quantum Inf. **10**, 55 (2024),

6.1 Introduction

A primary goal of emerging quantum computing technologies is to enable the simulation of quantum many-body systems that are challenging for classical computers [1, 39, 40]. Early experimental demonstrations of quantum simulation algorithms have focused on computing ground- and excited-state energies of small molecules or few-site spin and fermionic models [41–44, 97]. More recently, the scale of quantum simulation experiments has increased in terms of numbers of qubits, diversity of gate sets, and complexity of algorithms, as manifested in simulation of models based on real molecules and materials [47, 98], various phases of matter such as thermal [99], topological [100, 101] and many-body localized states [102, 103], as well as holographic quantum simulation using quantum tensor networks [104, 105]. As quantum advantages in random sampling have been established on quantum hardware [28, 106], focus has turned to the experimental demonstration of quantum advantages in problems of physical significance [107].

For applications in chemistry and physics, the calculation of the response properties of molecules and materials is of substantial interest [51]. Investigating response properties in the electronic structure theory framework involves calculating quantities such as the one-particle Green's function [108] and density-density response functions [109], which provide insight into interpreting experimental spectroscopic measurements [110]. Response properties of molecules and materials can be determined either in time domain or in frequency domain. Due to the natural ability of quantum computers to simulate time evolution [1, 39], near-term algorithms to compute time-domain response properties have been carried out on quantum hardware [30, 31, 111]. However, computing the frequency-domain response from the time-domain response using the typical gate set requires a time duration that exceeds

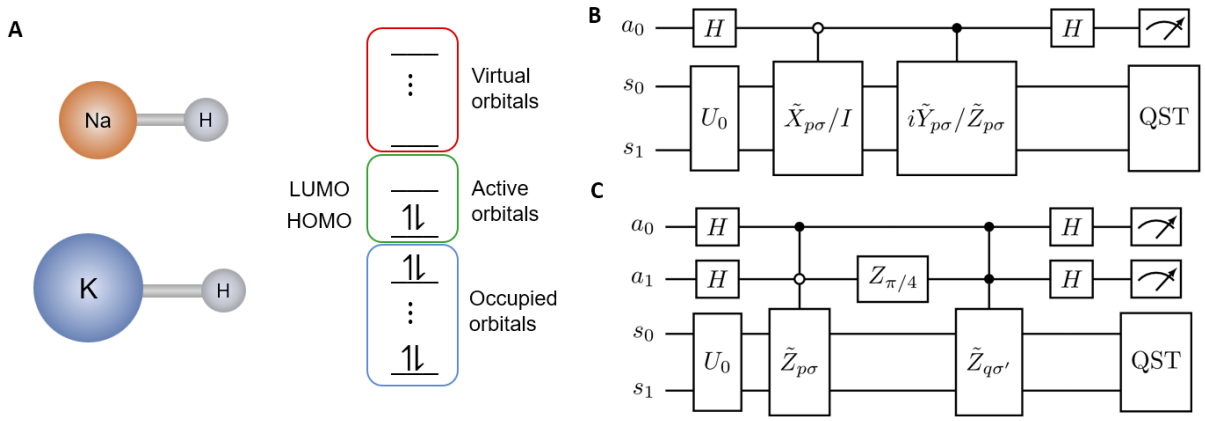

Figure 6.1: **Schematic of the diatomic molecules and diagrams of the LCU circuits for computing transition amplitudes.** (**A**) Schematic of the diatomic molecules NaH and KH. The active space consists of only the highest occupied molecular orbital (HOMO) and the lowest unoccupied molecular orbital (LUMO). (**B**) The circuits to calculate diagonal transition amplitudes, where a_0 is the ancilla qubit and s_0 and s_1 are the system qubits. For the spectral functions the target unitaries are $\tilde{X}_{p\sigma}$ and $i\tilde{Y}_{p\sigma}$, while for the response function the target unitaries are I and $\tilde{Z}_{p\sigma}$. (**C**) The circuit to calculate off-diagonal transition amplitudes in the response functions, where a_0 and a_1 are the ancilla qubits, and s_0 and s_1 are the system qubits. The double-controlled-$\tilde{Z}$ gates are decomposed with either iToffoli gates or CZ gates. In both (B) and (C), quantum state tomography (QST) is performed on the system qubits.

the circuit depth limitations of near-term quantum computers.

An alternative approach to determine these response properties is by computing them directly in the frequency domain. Frequency-domain algorithms generally involve obtaining the ground- and excited-state energies as well as the transition amplitudes between the ground state and the excited states. Although there are established methods to obtain ground- and excited-state energies on quantum computers [33, 112, 113], calculating transition amplitudes is less straightforward. Various schemes including variational quantum simulation [114–116], quantum subspace expansion [117] and quantum linear algebra [118] to determine frequency-domain response properties have been proposed. While variational quantum methods to compute frequency-domain response properties have been demonstrated [119], the accuracy of variational methods generally depends on the quality of the ansatz. Moreover, quantum subspace expansion is susceptible to numerical instabilities from basis linear dependence, and quantum linear algebra is out of reach for near-term quantum hardware. Recently, a non-variational scheme amenable to near-term hardware

implementation has been proposed [21, 22]. This scheme constructs the electron-added and electron-removed states simultaneously by exploiting the probabilistic nature of the linear combination of unitaries (LCU) algorithm [20]. Nevertheless, this LCU-based algorithm has not yet been demonstrated on quantum hardware in part due to the lack of efficient implementations of the multi-qubit gates.

In this work, we experimentally demonstrate the application of a high-fidelity three-qubit iToffoli gate [19] on a superconducting quantum processor to the calculation of frequency-domain response properties of diatomic molecules using LCU circuits. The use of the iToffoli gate leads to substantial reductions in the circuit depth by $\sim$ 50% and in the circuit execution time by $\sim$ 40%. The transition amplitudes between the ground state and the N-electron or $(N \pm 1)$-electron states of NaH and KH molecules are computed on the quantum hardware and used to construct spectral functions and density-density response functions. We apply error mitigation techniques including randomized compiling (RC) [120, 121] during circuit construction, and McWeeny purification [122] during postprocessing, both of which result in marked improvement of the experimental observables. The molecular response properties obtained from the reduced-depth circuits with iToffoli decomposition show comparable or better agreement with theory compared to those from circuits with CZ decomposition, despite incomplete Pauli twirling in the RC procedure applied to the iToffoli gate. Although the particular calculation of this work would require modifications to scale to larger systems, our results advance the general application of multi-qubit gates to quantum chemistry and related quantum simulation applications on near-term quantum hardware.

6.2 Materials and Methods

Calculation of Transition Amplitudes

In this section, we give the equations used to calculate transition amplitudes in the spectral function and density-density response function from quantities measured on hardware. We use the same notation as in the main text, where $|\Psi_0\rangle$ is the N-electron ground state, $|\Psi_\lambda^{N\pm1}\rangle$ are the $(N \pm 1)$-electron states, and $|\Psi_\lambda^N\rangle$ are the N-electron excited states. The transition amplitudes follow the same notation as in Ref. [22], where the transition amplitudes from the ground state to the $(N \pm 1)$-electron eigenstates in the calculation of spectral functions are

$$B^{(e)}_{\lambda,p\sigma,q\sigma'} = \langle\Psi_0|\hat{a}_{p\sigma}|\Psi^{N+1}_\lambda\rangle\langle\Psi^{N+1}_\lambda|\hat{a}^\dagger_{q\sigma'}|\Psi_0\rangle, \tag{6.1}$$

$$B^{(h)}_{\lambda,p\sigma,q\sigma'} = \langle\Psi_0|\hat{a}^\dagger_{p\sigma}|\Psi^{N-1}_\lambda\rangle\langle\Psi^{N-1}_\lambda|\hat{a}_{q\sigma'}|\Psi_0\rangle. \tag{6.2}$$

The spectral function only requires the diagonal transition amplitudes. Theoretically the (unnormalized) states after restraining the ancilla to $|0\rangle$ or $|1\rangle$ is $\frac{1}{2}(\tilde{X}_{p\sigma} \pm i\tilde{Y}_{p\sigma})\,|\Psi_0\rangle$. Let the tomographed density matrices corresponding to these states be $\rho^{\pm}_{p\sigma}$. The diagonal transition amplitudes are calculated as the overlap between the $(N \pm 1)$-electron eigenstates $|\Psi^{N\pm1}_\lambda\rangle$ and the tomographed density matrices $\rho^{\pm}_{p\sigma}$:

$$B^{(e)}_{\lambda,p\sigma,p\sigma} = \langle\Psi^{N+1}_\lambda|\rho^{-}_{\rho\sigma}|\Psi^{N+1}_\lambda\rangle, \tag{6.3}$$

$$B^{(h)}_{\lambda,p\sigma,p\sigma} = \langle\Psi^{N-1}_\lambda|\rho^{+}_{\rho\sigma}|\Psi^{N-1}_\lambda\rangle \tag{6.4}$$

Similarly, in the calculation of density-density response functions, we follow the notation in Ref. [21] and define the transition amplitudes from the ground state to N-electron eigenstates as

$$N_{\lambda,p\sigma,p\sigma} = \langle\Psi_0|\hat{n}_{p\sigma}|\Psi^{N}_\lambda\rangle\langle\Psi^{N}_\lambda|\hat{n}_{q\sigma'}|\Psi_0\rangle \tag{6.5}$$

In the diagonal circuits, theoretically the (unnormalized) state after restraining the ancilla qubit to $|1\rangle$ is $\frac{1}{2}(I - \tilde{Z}_{p\sigma})\,|\Psi_0\rangle$. Let the corresponding tomographed density matrix obtained from experiments be $\rho^{-}_{p\sigma}$. The diagonal transition amplitudes are calculated by taking the overlap of the N-electron eigenstates $|\Psi^{N}_\lambda\rangle$ and the tomographed density matrix $\rho^{-}_{p\sigma}$:

$$N_{\lambda,p\sigma,p\sigma} = \langle\Psi^{N}_\lambda|\rho^{-}_{p\sigma}|\Psi^{N}_\lambda\rangle \tag{6.6}$$

In the off-diagonal circuits, theoretically the (unnormalized) states after restraining the ancilla qubits to $ket10$ or $|11\rangle$ are $\frac{1}{4}[(I - \tilde{Z}_{p\sigma}) \pm (I - \tilde{Z}_{q\sigma'})]\,|\Psi_0\rangle$. Let the corresponding tomographed states obtained from experiments be $\rho^{\pm}_{p\sigma,q\sigma'}$. The intermediate transition amplitudes obtained directly from $\left|\Psi^{N}_\lambda\right\rangle$ are defined as

$$T^{\pm}_{\lambda,p\sigma,q\sigma'} = \langle\Psi^{N}_\lambda|\rho^{\pm}_{p\sigma,q\sigma'}|\Psi^{N}_\lambda\rangle, \tag{6.7}$$

from which the off-diagonal transition amplitude is determined by Eq. 25 in Ref. [21] (or equivalently Eq. 18 in Ref. [22]) as

$$N_{\lambda,p\sigma,q\sigma'} = e^{-i\pi/4}(T^{+}_{\lambda,p\sigma,q\sigma'} - T^{-}_{\lambda,p\sigma,q\sigma'}) + e^{i\pi/4}(T^{+}_{\lambda,q\sigma',p\sigma} - T^{-}_{\lambda,q\sigma',p\sigma}). \tag{6.8}$$

The transition amplitudes $B^{(e)}_{\lambda}$, $B^{(h)}_{\lambda}$ calculated from Eqs. 6.3 and 6.4 or N_{λ} calculated from Eqs. 6.6 and 6.8 are then combined with the ground-state energy E_0 as well as the excited-state energies $E^{N\pm1}_{\lambda}$ or E^{N}_{λ} to construct the spectral functions or density-density response functions.

Molecular Models

The molecular models studied in this work are HOMO-LUMO models of NaH at bond distance 3.7 Å and KH molecule at bond distance 3.9 Å in the STO-3G basis. The bond distances are chosen to ensure sufficient population in the excited states to facilitate comparisons of the spectral peaks. Molecular integrals are determined from PySCF [123]. Since our work focuses on comparing the transition amplitudes, the ground- and excited-state energies are determined classically, as has been performed in other quantum simulation demonstrations [64]. OpenFermion [124] is used to map the second-quantized Hamiltonians to qubit operators.

Quantum Circuit Construction

The ground-state preparation gate on the system qubits is determined classically by constructing a unitary that maps the all-zero initial states to the ground state and then decomposed into three CZ gates and single-qubit gates using the KAK decomposition [80]. The LCU circuits are then constructed by applying the gates shown in Figs. 6.1b and 6.1c, where the SWAP gates are decomposed according to the scheme in Ref. [125] and the circuits are transpiled by the functions `MergeInteractions`, `MergeSingleQubitGates` and `DropEmptyMoments` in Cirq [34]. The transition amplitudes are combined with the classically determined ground- and excited-state energies to calculate the spectral functions and response functions (see Supplementary Sec. II).

$\mathbb{Z}_2$ symmetry transformations on operators and qubit states

In this section, we describe the $\mathbb{Z}_2$ symmetry transformations applied to the qubit operators and ancilla qubit subspaces in the linear combination of unitaries (LCU) algorithm. This transformation converts the four-qubit operators and qubit subspaces into two-qubit ones, which are used in constructing the circuits for hardware runs.

There are four spin orbitals in the diatomic molecules we study in this work. We order them as $0\uparrow, 0\downarrow, 1\uparrow, 1\downarrow$ from left to right, corresponding to the qubit indices 0, 1, 2, 3, in the Pauli strings and qubit state bitstrings. The HOMO-LUMO molecular Hamiltonians of NaH and KH have the same number of up-spin and down-spin electrons. After Jordan-Wigner transformation, the parity of up-spin and down-spin electrons correspond to the qubit operators $ZIZI$ and $IZIZ$, which are $\mathbb{Z}_2$ symmetries of the Hamiltonian. The mean-field ground state $|\Phi_0\rangle = |1100\rangle$ has the expectation values $\langle ZIZI\rangle = \langle IZIZ\rangle = -1$, as does the exact ground state $|\Psi_0\rangle$.

We can define three types of states in our calculation based on $\mathbb{Z}_2$ symmetries: the "up-spin" states are the states that have symmetries $\langle ZIZI\rangle = 1, \langle IZIZ\rangle = -1$, which are obtained by applying $\hat{a}_{p\uparrow}$ or $\hat{a}^\dagger_{p\uparrow}$ on the ground state; the "down-spin" states are the states that have symmetries $\langle ZIZI\rangle = -1, \langle IZIZ\rangle = 1$, which are obtained by applying $\hat{a}_{p\downarrow}$ or $\hat{a}^\dagger_{p\downarrow}$ on the ground state; the "spin-balanced" states are the states that have the symmetries $\langle ZIZI\rangle = -1, \langle IZIZ\rangle = -1$, which are obtained by applying the number operators on the ground state and have the same symmetries as the ground state. Note that the up-spin and down-spin states here are defined from the expectation values of the $\mathbb{Z}_2$ symmetry operators but not from the spin-z components of the corresponding molecular states. For example, the qubit computational state $|0100\rangle$ represents the molecular state with a single electron in the $0\downarrow$ orbital, which has total spin-z expectation value of $-1/2$, but in our definition it is classified as an up-spin state.

For each type of state, we aim to find a $\mathbb{Z}_2$ transformation that generates the minimum number of gates in the circuits that apply the creation or annihilation operators $\hat{a}^{(\dagger)}_{p\sigma}$ or the number operators $\hat{n}_{p\sigma}$. Recall from the main text that in the Jordan-Wigner transformation, the creation or annihilation operators $\hat{a}^{(\dagger)}_{p\sigma}$ have the decomposition $\bar{X}_{p\sigma} \pm i\bar{Y}_{p\sigma}$, where $\bar{X}_{p\sigma}$ and $\bar{Y}_{p\sigma}$ are the Jordan-Wigner transformed Pauli X and Y operators on orbital p with spin σ, and the number operators $\hat{n}_{p\sigma}$ have the decomposition $I - Z_{p\sigma}$. The transition amplitudes under the $\mathbb{Z}_2$ transformation $U_{\mathbb{Z}_2}$ can be expressed as

$$\langle\Psi^{N\pm1}_\lambda|\hat{a}^{(\dagger)}_{p\sigma}|\Psi_0\rangle = \langle\Psi^{N\pm1}_\lambda|U^\dagger_{\mathbb{Z}_2}U_{\mathbb{Z}_2}\hat{a}^{(\dagger)}_{p\sigma}U^\dagger_{\mathbb{Z}_2}U_{\mathbb{Z}_2}|\Psi_0\rangle = \left(\langle\Psi^{N\pm1}_\lambda|U^\dagger_{\mathbb{Z}_2}\right)\left[U_{\mathbb{Z}_2}(\bar{X}_{p\sigma} \pm i\bar{Y}_{p\sigma})U^\dagger_{\mathbb{Z}_2}\right]\left(U_{\mathbb{Z}_2}|\Psi_0\rangle\right), \tag{6.9}$$

$$\langle\Psi^{N}_\lambda|\hat{n}_{p\sigma}|\Psi_0\rangle = \langle\Psi^{N}_\lambda|U^\dagger_{\mathbb{Z}_2}U_{\mathbb{Z}_2}\hat{n}_{p\sigma}U^\dagger_{\mathbb{Z}_2}U_{\mathbb{Z}_2}|\Psi_0\rangle = \left(\langle\Psi^{N}_\lambda|U^\dagger_{\mathbb{Z}_2}\right)\left[U_{\mathbb{Z}_2}(I - \bar{Z}_{p\sigma})U^\dagger_{\mathbb{Z}_2}\right]\left(U_{\mathbb{Z}_2}|\Psi_0\rangle\right), \tag{6.10}$$

where the transformed bra state, ket state and operator are grouped in brackets

at the end of each equation. On the up-spin states, we use the transformation $U_{\mathbb{Z}_2} = \text{CNOT}(3,1)\text{CNOT}(2,0)$; on the down-spin states, we use the transformation $U_{\mathbb{Z}_2} = \text{SWAP}(2,3)\text{CNOT}(3,1)\text{CNOT}(2,0)$, followed by multiplying all the operators by -1; on the spin-balanced states, we use the transformation $U_{\mathbb{Z}_2} = \text{CNOT}(2,3)\text{CNOT}(3,1)\text{CNOT}(2,0)$. After the $\mathbb{Z}_2$ transformation, the first two qubits on the operators and the states are then truncated.

As an example, consider the transformation of the Pauli string $\bar{X}_{1\uparrow} = ZZXI$. After we apply the transformation CNOT(3, 1)CNOT(2, 0), the operator becomes $-YZYZ$. To truncate qubit 0 and qubit 1, we need to find the constant factor after the transformed Pauli string acts on the first two qubits of the ground state. The constant factor for $\tilde{X}_{1\uparrow}$ is $\langle 01|YZ|11\rangle = i$, where $\langle 01|$ are the bit values on the first two qubits of the transformed up-spin states $\langle \Psi_\lambda^{N\pm1}|U_{\mathbb{Z}_2}^\dagger$ and $|11\rangle$ are the bit values on the first two qubits of the transformed ground state $U_{\mathbb{Z}_2}|\Psi_0\rangle$. The factor of i is then combined with the rest of the Pauli string $-YZ$ to give the final truncated form of the Pauli string $\tilde{X}_{1\uparrow} = -iYZ$. The Pauli strings and qubit state bitstrings before and after the $\mathbb{Z}_2$ symmetry transformations and truncations are given in Table 6.1.

Quantum Device

The quantum device used in this work is a superconducting quantum processor with eight transmon qubits [121, 126]. The algorithm is performed on a four-qubit subset of the device with linear connectivity. Single-qubit gates are performed with resonant microwave pulses. Multiplexed dispersive readout allows for simultaneous state discrimination on all four qubits. CZ gates between all nearest neighbors are performed according to the method in Ref. [127]. The same method allows for a native CS gate on a particular pair of qubits according to the requirements of the algorithm. While single-qubit gates are applied simultaneously, microwave crosstalk requires that all two- and three-qubit gates are applied in separate cycles from each other as well as from any single-qubit gates. TrueQ [128] is used for circuit manipulations in the implementation of RC as well as gate benchmarking. Internal software is used to map the circuits to hardware pulses for implementing the native gate set.

Calibration of the iToffoli Gate

This work employs the recently developed C-iX-C iToffoli gate [19]. In this section we outline the procedure for eliminating spectator errors during the gate application. Since the gate acts on a three-qubit subset of the full four-qubit subsystem we need

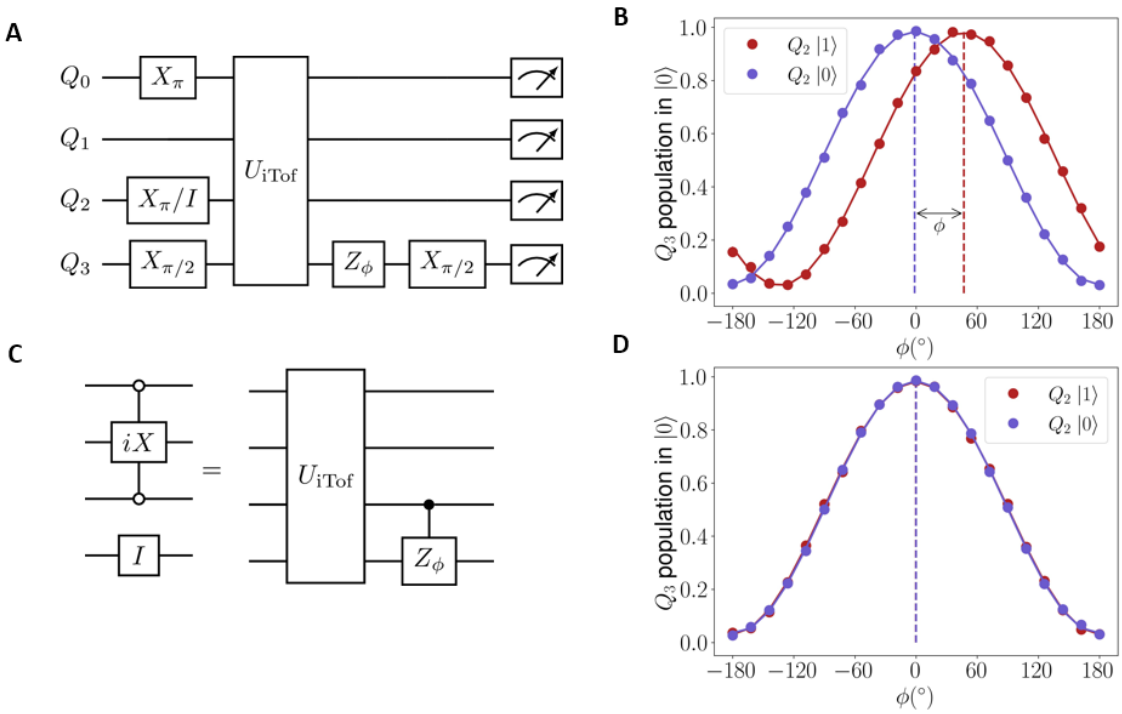

Figure 6.2: **Cancellation of spectator error during iToffoli gate.** (**A**) Ramsey protocol for detecting spurious ZZ error between Q_2 and spectator Q_3 during the application of the iToffoli gate. (**B**) $|0\rangle$ population for Q_3 after application of the Ramsey sequence in (A) conditional on the state of Q_2. The relative phase shift between the sinusoidal curves gives the unwanted conditional phase ϕ, which must be corrected. (**C**) A pure iToffoli gate on Q_0-Q_2 is achieved by applying the iToffoli drive from Ref. [19] followed by a CZ_ϕ gate. (**D**) Same as (B) except now the CZ_ϕ correction gate is applied immediately after the iToffoli drive, correcting the unwanted ZZ error.

to understand and correct the spectator error on the fourth qubit. For concreteness we label qubits Q_i for $i = 0, \ldots, 3$ where the iToffoli gate acts on Q_0, Q_1 and Q_2 with Q_3 as the spectator qubit. States on the four qubits are denoted in the form $|Q_0Q_1Q_2Q_3\rangle$. We run a simple circuit that prepares the system in either $|100{+}\rangle$ or $|101{+}\rangle$ (where $|+\rangle = (|0\rangle + |1\rangle)/\sqrt{2}$) and apply the iToffoli gate in a Ramsey-like sequence to determine the Z rotation on Q_3 conditional on the state of its nearest neighbor Q_2 (see Fig. 6.2a for circuit diagram). We observe an unwanted conditional phase interaction between Q_2 and Q_3 with a conditional phase $\phi = 48.4°$ (see Fig. 6.2b). This interaction results from the conditional Stark shift between Q_2 and Q_3 when a strong off-resonant drive is applied to Q_2 at the frequency of Q_1 to implement the iToffoli gate [127]. We can use the same effect to undo the conditional phase by applying simultaneous off-resonant drives to Q_2 and Q_3 for a period of

121 ns following the iToffoli drive sequence, which explains why the iToffoli gate duration in our work is longer than that in Ref. [19]. The full pulse sequence and characterization of the residual conditional rotation with the cancellation applied are shown in Figs. 6.2c and 6.2d. We benchmark the resulting gate implementation using cycle benchmarking [129]. With this correction, we measure a gate fidelity of 97.8% when isolated to the cycle that only involve qubits Q_0, Q_1 and Q_2, and a small reduction to 96.6% when including the idling spectator qubit Q_3.

Two-qubit CZ and CS/CS† gates are calibrated according to Ref. [127]. Gate fidelities and durations are listed in Table 6.2. Qubit coherence times are listed in Table 6.3 for completeness.

Randomized Compiling for Non-Clifford Gates

In this section we outline a modified version of randomized compiling (RC) [120, 121] that is applied to the circuits used to compute the observables in the main text. RC is expected to mitigate errors and improve algorithm performance. A broad native entangling gate set is used, consisting of both Clifford gates (CZ) and non-Clifford gates (CS, CS†, iToffoli). RC is typically used with hard cycles of n-qubit Cliffords where the twirling group $\mathcal{T}$ is chosen to be the group of tensor products of n single-qubit Paulis. By the definition of Clifford gates, for any Clifford C and twirling gate $T \in \mathcal{T}$ there is some $T^c \in \mathcal{T}$ such that $C = TCT^c$. When RC is applied to the hard cycle C_k consisting of Clifford gates, it proceeds by choosing some T_k and T_k^c such that $C_k \rightarrow T_k C_k T_k^c$. The single-qubit Paulis T_k and T_k^c are compiled into the easy cycles of single-qubit gates before and after the Clifford cycle C_k, thus keeping the total circuit depth unchanged.

In order to generalize the method to the non-Clifford gates employed in this work we first find the subsets $\mathcal{T}_X \subset \mathcal{T}$ for $X = \mathrm{CS}, \mathrm{CS}^\dagger, \mathrm{iToffoli}$ where for all $T \in \mathcal{T}_X$ there is some $T^c \in \mathcal{T}_X$ such that $X = TXT^c$. RC proceeds in the same way as above except that the twirling gates for hard cycles consisting of gate X are simply chosen from the subset $\mathcal{T}_X$ of Pauli strings that stabilize gate X. Both the CS and CS† are stabilized by 4 of the possible 16 two-qubit Pauli strings and the iToffoli is stabilized by 8 of the possible 64 three-qubit Pauli strings. For all these non-Clifford gates the twirling and inversion gates are the same, $T = T^c$. Results "with RC" in the main text involve averaging the experimental bitstring output distributions over 100 equivalent circuit randomizations generated according to the process outlined here, with each circuit measured for 500 shots. These are compared to results "without

RC" in which the bare circuit is measured for 50000 shots such that the total number of shots is maintained between the two implementations.

All error processes can be described by a superoperator acting on the density matrix of the full qubit register. Written in the n-qubit Pauli basis this error process matrix is referred to as a Pauli transfer matrix (PTM) with diagonal elements giving Pauli fidelities and off-diagonal elements characterizing the unitary (coherent) and non-unitary (incoherent) errors. As discussed in Refs. [120, 121], applying RC tailors coherent errors into stochastic Pauli noise, which suppresses the off-diagonal elements of the PTM resulting from coherent errors. This holds for the PTM describing errors during the CZ cycles, since these undergo perfect Pauli twirling (in the limit of infinite randomizations). However, in the case of the non-Clifford gate cycles, the twirling is imperfect (since we only twirl over a subset of the n-qubit Pauli strings). As a result, some, but not all, of the off-diagonal elements in the corresponding PTMs are suppressed. In other words, not all coherent errors are tailored to stochastic Pauli noise. This imperfect noise tailoring is the main limitation of our approach to generalizing RC to non-Clifford gates.

We observe a small improvement in the state fidelities when using RC without purification but a much larger improvement when using RC with purification. The improvement in the state fidelities can be explained by the suppression of off-diagonal components of the PTM due to coherent errors, which lowers the overall error rate slightly. As discussed in the main text, if the stochastic Pauli error rates are similar after noise tailoring then the errors are approximately depolarizing and can be largely corrected by McWeeny purification. The deviation of the noise from purely depolarizing is responsible (along with the finite number of randomizations) for the remaining infidelity after RC and purification are applied. Conversely, without RC a larger fraction of the error is a coherent over/under-rotation of the two-qubit Bloch vector which cannot be corrected by purification.

6.3 Results

Quantum Algorithm for Transition Amplitudes of Diatomic Molecules

We consider the HOMO-LUMO models of the diatomic molecules NaH and KH as shown in Fig. 6.1a (see Methods for parameters of the molecular models). Such molecular models with reduced active space have been used in benchmarking quantum chemistry methods on quantum computers [131]. The HOMO-LUMO model generates two spatial orbitals or equivalently four spin orbitals, which correspond

to four qubits after Jordan-Wigner transformation [38]. To reduce quantum resources, we exploit the number symmetry in each spin sector to reduce the number of qubits from four to two using a qubit-tapering technique [77] (details given in Supplementary Sec. I).

The observables we aim to determine are the spectral function and density-density response function. Suppose that the molecular Hamiltonian with reduced active space has ground state $|\Psi_0\rangle$ with energy E_0, and $(N\pm1)$-electron eigenstates $\left|\Psi_\lambda^{N\pm1}\right\rangle$ with energies $E_\lambda^{N\pm1}$. Let $\hat{a}_{p\sigma}^\dagger$ and $\hat{a}_{p\sigma}$ be the creation and annihilation operators on orbital p with spin σ, respectively. The one-particle Green's function has the expression [108]:

$$\begin{aligned} G_{pq}(\omega) = &\sum_{\lambda\sigma} \frac{\langle\Psi_0|\hat{a}_{p\sigma}|\Psi_\lambda^{N+1}\rangle\langle\Psi_\lambda^{N+1}|\hat{a}_{q\sigma}^\dagger|\Psi_0\rangle}{\omega + E_0 - E_\lambda^{N+1} + i\eta} \\ &+ \sum_{\lambda\sigma} \frac{\langle\Psi_0|\hat{a}_{q\sigma}^\dagger|\Psi_\lambda^{N-1}\rangle\langle\Psi_\lambda^{N-1}|\hat{a}_{p\sigma}|\Psi_0\rangle}{\omega - E_0 + E_\lambda^{N-1} + i\eta} \end{aligned} \tag{6.11}$$

where ω is the frequency and η is a small broadening factor. The spectral function $A(\omega)$ is related to the Green's function by $A(\omega) = -\pi^{-1}\,\mathrm{Im\ Tr}\ G(\omega)$.

For the density-density response function, we consider the charge-neutral N-electron excited states $\left|\Psi_\lambda^N\right\rangle$ with energies E_λ^N and the number operator $\hat{n}_{p\sigma}$ on the orbital p with spin σ. The density-density response function has the expression [109]:

$$R_{pq}(\omega) = \sum_\lambda \frac{\sum_{\sigma\sigma'}\langle\Psi_0|\hat{n}_{p\sigma}|\Psi_\lambda^N\rangle\langle\Psi_\lambda^N|\hat{n}_{q\sigma'}|\Psi_0\rangle}{\omega + E_0 - E_\lambda^N + i\eta}. \tag{6.12}$$

The operators $\hat{a}_{p\sigma}^\dagger, \hat{a}_{p\sigma}$ and $\hat{n}_{p\sigma}$ are not unitary, but they can be written as linear combination of unitary operators as

$$\hat{a}_{p\sigma}^\dagger = (\bar{X}_{p\sigma} - i\bar{Y}_{p\sigma})/2, \tag{6.13}$$

$$\hat{a}_{p\sigma} = (\bar{X}_{p\sigma} + i\bar{Y}_{p\sigma})/2, \tag{6.14}$$

$$\hat{n}_{p\sigma} = (I - Z_{p\sigma})/2, \tag{6.15}$$

where I is the identity operator, $Z_{p\sigma}$ is the Pauli Z operator on orbital p with spin σ, and $\bar{X}_{p\sigma}$ and $\bar{Y}_{p\sigma}$ are the Jordan-Wigner transformed Pauli X and Y operators on orbital p with spin σ with a string of Z operators included to account for the anticommutation relation [38]. The Pauli strings $\bar{X}_{p\sigma}, \bar{Y}_{p\sigma}$ and $Z_{p\sigma}$ undergo the

same transformation and qubit tapering process as the Hamiltonian (details given in Supplementary Sec. I). Except for the identity operator which does not change under the transformation, we label the transformed $\bar{X}_{p\sigma}, \bar{Y}_{p\sigma}, Z_{p\sigma}$ as $\tilde{X}_{p\sigma}, \tilde{Y}_{p\sigma}$ and $\tilde{Z}_{p\sigma}$.

The LCU circuits to calculate diagonal and off-diagonal transition amplitudes are given in Figs. 6.1b and 6.1c, respectively. Each circuit has two system qubits s_0 and s_1, and one ancilla qubit a_0 or two ancilla qubits a_0 and a_1. The unitary U_0 prepares the ground state $|\Psi_0\rangle$ on the system qubits from the all-zero initial state. The operators $\tilde{X}_{p\sigma}$ and $\tilde{Y}_{p\sigma}$ are only present in the diagonal circuit in Fig. 6.1b since the calculation of the spectral function only requires diagonal transition amplitudes. The operators I and $\tilde{Z}_{p\sigma}$ are present in both the diagonal circuit in Fig. 6.1b and in the off-diagonal circuit in Fig. 6.1c, since the density-density response function requires both the diagonal and off-diagonal transition amplitudes. The remaining two double-controlled identity gates that would complete the LCU circuit, which correspond to the first double-controlled gate (controlled on $|0\rangle$ of both a_0 and a_1) and the third double-controlled gate (controlled on $|0\rangle$ of a_0 and $|1\rangle$ of a_1) in Fig. 3 of Ref. [22], are not shown because they are equivalent to identity gates on the whole circuit. We note that the original algorithm [22] proposed performing quantum phase estimation on the system qubits, but due to quantum resource constraints we instead apply quantum state tomography [132] to the system qubits while measuring the ancilla qubits in the Z basis.

In the diagonal circuits, we obtain the (unnormalized) system-qubit states $\frac{1}{2}(\tilde{X}_{p\sigma} \pm i\tilde{Y}_{p\sigma})|\Psi_0\rangle$ or $\frac{1}{2}(I \pm \tilde{Z}_{p\sigma})|\Psi_0\rangle$ with probabilities $p_\pm$, where the probabilities are specified by the ancilla measurement outcome as $p_+ = p_{a_0=0}$ and $p_- = p_{a_0=1}$; in the off-diagonal circuits, we obtain the (unnormalized) system-qubit states $\frac{1}{4}[(I - \tilde{Z}_{p\sigma}) \pm e^{i\pi/4}(I - \tilde{Z}_{q\sigma'})]|\Psi_0\rangle$ with probabilities $p_\pm$, where $p_+ = p_{(a_0,a_1)=(1,0)}$ and $p_- = p_{(a_0,a_1)=(1,1)}$. We take the overlap of the tomographed system-qubit states with the exact eigenstates, which are then postprocessed according to Eq. 18 in Ref. [22] or Eq. 25 in Ref. [21] to yield the transition amplitudes (see Supplementary Sec. II). The transition amplitudes are then used to construct the spectral function and density-density response function according to Eqs. 6.11 and 6.12.

In the following sections, for simplicity, we will denote the diagonal circuit that applies the operator $\hat{a}^{(\dagger)}_{p\sigma}$ or $\hat{n}_{p\sigma}$ as the $p\sigma$-circuit, and the off-diagonal circuit that applies the operators $\hat{n}_{p\sigma}$ and $\hat{n}_{q\sigma'}$ as the $(p\sigma, q\sigma')$-circuit.

iToffoli versus CZ Decompositions in LCU Circuits

The transformed and tapered operators are two-qubit Pauli strings with multiplicative factors of ± 1 or $\pm i$. To apply the single- or double-controlled gates, we follow the standard multi-qubit Pauli gate decomposition [29] with the base gate as CZ or CCZ and use CNOT gate equivalents, which consist of native CZ gates dressed by Hadamard gates, to extend the weights of the Pauli strings. The multiplicative factor -1 or $\pm i$ can be applied as a single-qubit phase gate on the ancilla in the diagonal circuits, or as the native CZ, CS, or $\mathrm{CS}^\dagger$ on the two ancillae in the off-diagonal circuits. Additionally, X gates are wrapped around the ancilla qubits controlled on $|0\rangle$. Figure 6.3a shows how a double-controlled gate with ancilla a_0 controlled on $|1\rangle$, ancilla a_1 controlled on $|0\rangle$, and a target operator $-ZZ$ is applied on the device.

We decompose the CCZ gate either with the three-qubit iToffoli gate as shown in Fig. 6.3b or with the native CZ gates. The iToffoli decomposition starts with a double-controlled iZ component, followed by a long-range $\mathrm{CS}^\dagger$ gate to cancel the phase factor i. The SWAP gates in the long-range $\mathrm{CS}^\dagger$ part of the circuit are further simplified in the transpilation stage or decomposed into three CZ gates and additional single-qubit gates according to a recent work on the same quantum device [125]. For the CZ decomposition of CCZ, we use the topology-aware quantum circuit synthesis package BQskit [133] to obtain the optimal decomposition as eight CZs under linear qubit connectivity, as opposed to the six-CZ decomposition that requires all-to-all qubit connectivity [134].

The spectral function only requires the four diagonal circuits $0\uparrow, 0\downarrow, 1\uparrow, 1\downarrow$. The density-density response function requires four diagonal circuits $0\uparrow, 0\downarrow, 1\uparrow, 1\downarrow$ and six off-diagonal circuits $(0\uparrow, 0\downarrow), (0\uparrow, 1\uparrow), (0\uparrow, 1\downarrow), (0\downarrow, 1\uparrow), (0\downarrow, 1\downarrow), (1\uparrow, 1\downarrow)$. We use the same transpilation procedure to optimize the circuits constructed from iToffoli decomposition and CZ decomposition (details given in Methods).

The diagonal circuits after transpilation are relatively shallow circuits with maximum circuit depth (excluding virtual Z gates) of 19, maximum two-qubit gate count of 7 and no iToffoli gates. In the off-diagonal circuits, the circuit depths range from 24 to 29 for iToffoli decomposition and from 54 to 59 for CZ decomposition. As for the two- and multi-qubit gate counts, each iToffoli-decomposed circuit contains two iToffoli gates and 9 to 12 native two-qubit gates, while each CZ-decomposed circuit contains 19 to 21 native two-qubit gates. The iToffoli decomposition thus results in $\sim 50\%$ reduction in the circuit depth and the number of two-qubit gates compared

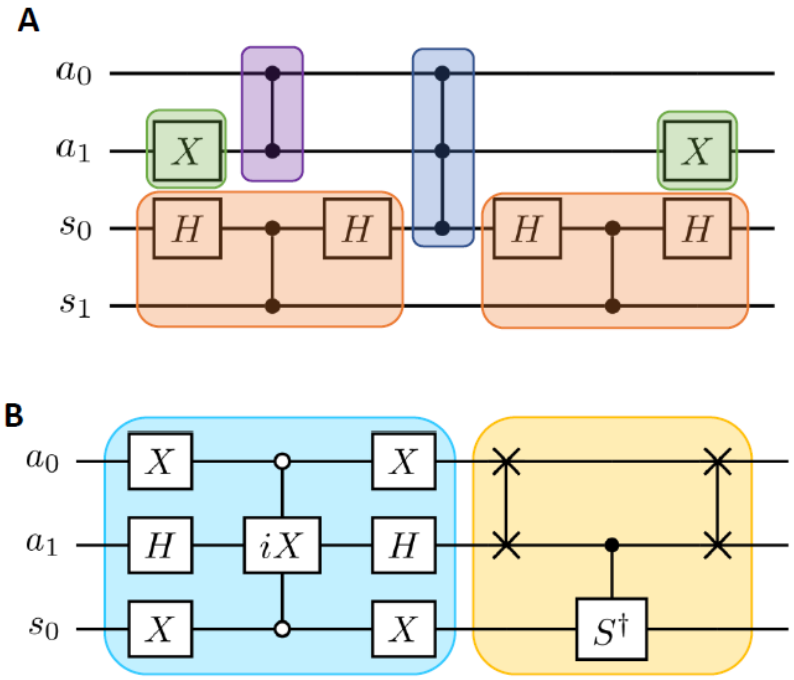

Figure 6.3: **Decomposition of the double-controlled composite gates in the LCU circuits.** (**A**) Example of the decomposition of a double-controlled $-ZZ$ gate, which is controlled on $|1\rangle$ of a_0 and $|0\rangle$ of a_1, into CCZ (blue) along with other single- and two-qubit gates. The X gates (green) are used to adjust the control states; the CZ gate on a_0 and a_1 (purple) is used to adjust the overall multiplicative factor, which is -1 in this case; the CNOT gate equivalents (orange) are used to extend the weights of the Pauli string as in Ref. [29]. (**B**) Decomposition of the CCZ gates with the iToffoli gate, which is a CC-iX gate with both control qubits controlled on $|0\rangle$. The decomposition includes the equivalent of a CC-iZ gate (light blue) and the equivalent of a long-range $\mathrm{CS}^\dagger$ gate (yellow). The SWAP gates are simplified in the transpilation stage or further decomposed with CZ gates according to Ref. [125].

to the CZ decomposition.

We also compare the durations of the circuits that result from the iToffoli decomposition and the CZ decomposition. The duration of each CZ gate is 201 ns [125], while the duration of each iToffoli gate is 413 ns [19]. Combined with other gate execution times, the durations of the iToffoli- (CZ)-decomposed circuits range from 2.9 – 3.6 μs (4.9 – 5.5 μs), corresponding to a reduction in circuit execution time of approximately 40% from using iToffoli gates. This reduction in duration is expected to have a more pronounced effect on deeper circuits with execution times comparable to qubit coherence times, which are on the order of 30 – 50 μs [125]. A complete

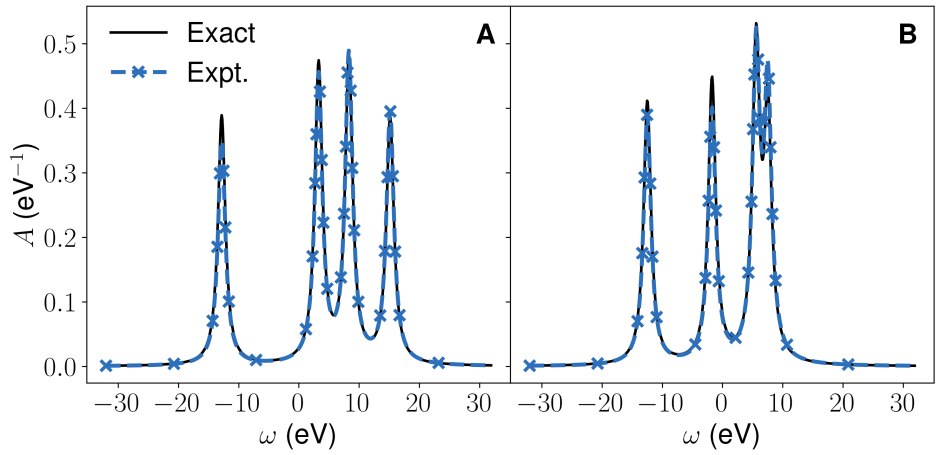

Figure 6.4: **Spectral function of diatomic molecules.** Spectral function of (**A**) NaH, (**B**) KH. The circuits to obtain the spectral function are shallow three-qubit circuits that do not require the iToffoli gates. A broadening factor of $\eta = 0.75$ eV is used to produce both the exact and the experimental spectra. The experimental spectral functions are in quantitative agreement with the exact ones, with maximum peak height deviation of 10.6%.

set of gate durations and qubit coherence times are given in Supplementary Sec. III.

Spectral Function and Response Function on Quantum Hardware

The spectral functions of NaH and KH are shown in Fig. 6.4. The density matrices are obtained from quantum state tomography and postprocessed with McWeeny purification. Randomized compiling is not employed in constructing the circuits for obtaining these results. A broadening factor of $\eta = 0.75$ eV is used to produce both the exact and experimental spectra. As the peak frequencies are determined classically, the primary metric for comparison of spectral functions is the peak height. The experimental spectral functions show very good agreement with the exact ones, with maximum peak height deviation of 10.6%.

We next turn to the density-density response function, which is more challenging to compute than the spectral function because it requires the deeper off-diagonal circuits containing three-qubit iToffoli gates. We begin by considering a specific off-diagonal circuit needed for the density-density response function, the $(0\uparrow, 0\downarrow)$ -circuit. To understand the influence of the iToffoli gate on the accuracy of the executed circuit, we compute the fidelity of the whole qubit register obtained by quantum state tomography versus circuit depth. The same quantity was computed for a circuit using only CZ gates to decompose the double-controlled gates. The results are shown in Fig. 6.5. Although the iToffoli decomposition shows a steeper

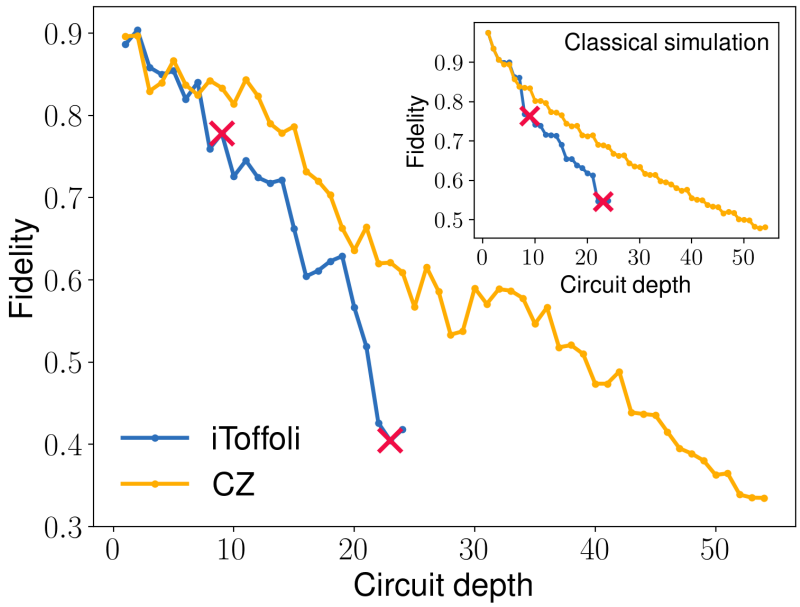

Figure 6.5: **Fidelity versus circuit depth of the $(0\uparrow, 0\downarrow)$-circuit for NaH.** Fidelity for the iToffoli decomposition (blue), which has a circuit depth of 24, and the CZ decomposition (yellow), which has a circuit depth of 54. The locations of the iToffoli gates are marked by red crosses. The CZ decomposition results in lower overall fidelity compared to iToffoli decomposition due to higher circuit depth. The inset is the corresponding data from noisy simulation and shows a similar trend. All results in this figure are raw experimental or simulated data without any error mitigation.

decrease in fidelity compared to the CZ decomposition, the fidelity at the end of the circuit is higher due to lower circuit depth. The noisy simulation in the inset of Fig. 6.5 shows a similar trend. The iToffoli gate reported in Ref. [19] does not consider spectator errors on neighboring qubits, which are cancelled out in the gate calibration in this work (details given in Supplementary Sec. III). The cycle benchmarking fidelity of the iToffoli gate accounting for the spectator qubit is 96.6%, lower than the single-qubit gate fidelities which are above 99.5% and the two-qubit gate fidelities which are between 98.0% and 98.7%, which may explain the steeper decay in fidelity with circuit depth in the iToffoli circuit compared to the CZ circuit.

Next, we examine the fidelity of the final state in each iToffoli-decomposed circuit used in the calculation of response functions. Figure 6.6 shows the system-qubit state fidelities on each response function circuit for NaH, where McWeeny purification is applied to the system-qubit density matrix after restricting the full density matrix to each ancilla bitstring sector. Comparing the values in Fig. 6.6a with those in

Fig. 6.6b, we can see that RC itself only results in a moderate improvement in the fidelities, with the average diagonal fidelities changing from 84.6% to 85.5% and average off-diagonal fidelities changing from 45.2% to 54.8%. However, the results between Fig. 6.6b and Fig. 6.6d show that RC combined with purification yields an average diagonal fidelity of 99.9% and an average off-diagonal fidelity of 96.0%, even though purification without RC only leads to a limited improvement in the average diagonal fidelity from 85.6% to 95.7%, and in the average off-diagonal fidelity from 45.2% to 67.4% in Figs. 6.6a and 6.6c.

We now show the imaginary parts of the density-density response functions χ_{00} and χ_{01} of NaH in Fig. 6.7. Here χ_{00} is obtained from two diagonal circuits $0\uparrow, 0\downarrow$ and one off-diagonal circuit $(0\uparrow, 0\downarrow)$, while χ_{01} is obtained from four off-diagonal circuits $(0\uparrow, 1\uparrow), (0\uparrow, 1\downarrow), (0\downarrow, 1\uparrow), (0\downarrow, 1\downarrow)$. All experimental results are postprocessed with purification after constraining the ancilla qubits to each bitstring subspace. A broadening factor of $\eta = 1.5$ eV is used to produce the response functions.

Overall, the iToffoli decomposition yields better results compared to the CZ decomposition in the absence of RC, while both decompositions yield comparable results when RC is applied. Examining the spectral functions in Figs. 6.7a and 6.7c, we observe that the peak at 24.0 eV is not present in χ_{00} and has the wrong sign in χ_{01} under the CZ decomposition. Although the iToffoli decomposition also produces the peak at 24.0 eV with the wrong sign in χ_{01}, it produces a peak with a deviation of 6.1% from the exact peak in χ_{00}. The same trend occurs for the peak at 1.4 eV. Both decompositions result in similar deviations of the peak height at 1.4 eV in χ_{01}, where the deviation is 45.3% for the CZ decomposition and 52.5% for the iToffoli decomposition. However, in χ_{00}, the iToffoli decomposition yields a 26.6% deviation from the exact peak in χ_{00}, whereas the CZ decomposition produces the peak more than twice the theoretical value.

The results for circuits constructed with RC are shown in Figs. 6.7b and 6.7d. In χ_{00}, deviations from the exact peak height at 24.0 eV and 1.4 eV are 34.8% and 4.7% for the CZ decomposition, and are 11.8% and 24.0% for the iToffoli decomposition. In χ_{01}, deviations from the exact peak at 24.0 eV and 1.4 eV are 5.7% and 28.2% for the CZ decomposition, but are 39.2% and 32.2% for the iToffoli decomposition. Since the iToffoli gate is non-Clifford, our implementation of RC results in incomplete Pauli twirling compared to applying RC to the CZ-decomposed circuits (see Supplementary Sec. IV). The incompleteness of RC on

the iToffoli-decomposed circuits may explain why the two decompositions have comparable peak height deviations with RC despite the initial advantage for the iToffoli decomposition without RC due to its lower circuit depth.

This section presents the system-qubit state fidelities and density-density response functions of the KH molecule. Figure 6.8 shows the system-qubit state fidelities in the response function calculations of KH. In the case of RC without purification, the average off-diagonal fidelity improves from 49.2% in Fig. 6.8a to 61.3% in Fig. 6.8b, whereas the average diagonal fidelity slightly decreases from 91.5% in Fig. 6.8a to 90.5% in Fig. 6.8b. Purification without RC shows a unified improvement across both diagonal and off-diagonal fidelities, which change to 97.1% and 66.9% from 91.5% and 49.2% respectively when comparing Fig. 6.8c to Fig. 6.8a. The most significant improvement again comes from applying both purification and RC, with the average diagonal fidelity 99.8% and average off-diagonal fidelity 95.9% in Fig. 6.8d.

Figure 6.9 shows the density-density response functions of KH with all data post-processed with McWeeny purification. Similar to the case of NaH, the iToffoli decomposition exhibits a better agreement with exact results in the absence of RC. For χ_{00} without RC in Fig. 6.9a, the deviations from exact peak heights are 1.0% and 13.9% for the iToffoli decomposition, but are 41.6% and 17.1% for the CZ decomposition. For χ_{01} without RC in Fig. 6.9c, although both decompositions fail to capture the peak at 24 eV, the iToffoli decomposition reproduces the exact peak with an 8.2% deviation while the CZ decomposition results in only around half of the peak height for the peak at 1.4 eV. When RC is used to construct the circuits, the results are comparable between the two decompositions. For χ_{00} with RC in Fig. 6.9b, the peak height deviations in the two peaks are 17.0% and 10.7% for the iToffoli decomposition, which are slightly better than the CZ decomposition results of 21.6% and 20.8%. For χ_{01} with RC in Fig. 6.9d, the CZ decomposition exhibits a better agreement, with peak height deviations of 4.2% and 7.7%, compared to the values from the iToffoli decomposition of 26.6% and 45.5%.

6.4 Discussion

We have carried out an LCU-based algorithm to compute the spectral functions and density-density response functions of diatomic molecules from the transition amplitudes determined on a superconducting quantum processor. Using a native high-fidelity iToffoli gate [19] has enabled the required circuit depth to be reduced

by $\sim$ 50% and the circuit execution time to be reduced by $\sim$ 40%. These resulting circuits produced better agreement with the exact results compared to the circuits constructed only from single- and two-qubit gates when RC is not employed in circuit construction. We also developed an RC protocol for the non-Clifford iToffoli gate, and have shown that in the absence of complete Pauli twirling on the iToffoli gate, the circuits constructed from iToffoli gates gave comparable results as the circuits constructed only from single- and two-qubit gates with RC.

The quality of the computed observables was greatly improved by the use of several error mitigation techniques. Specifically, our results highlight the significance of RC [120, 121] combined with McWeeny purification [122] for quantum simulation. McWeeny purification has been widely used in quantum chemistry [135] and started to be exploited in quantum computing for constraining the purity of the output state [47, 136]. Our results have shown that RC or McWeeny purification individually only improves the experimental results to a limited extent, as observed in the change of the average off-diagonal fidelities from 45.8% to 54.2% with only RC, and to 67.4% with only purification in Fig. 6.6. However, the combination of RC and purification results in a substantial improvement in the quality of the results with the system-qubit state fidelities being 96.0% on average.The larger improvement with purification is explained by the fact that RC tailors coherent errors into stochastic Pauli errors. If the rates of various stochastic Pauli errors are similar, the errors are largely depolarizing and can be corrected by the purification procedure, yielding the high fidelities in Fig. 6.6d (see Supplementary Sec. IV for further discussion). Moreover, previous works applied purification to the whole qubit register, but we have shown here that the purification scheme can be applied when there is purity constraint on a subset of qubits. Additionally, our work is the first to apply RC to the non-Clifford iToffoli gate. As more native non-Clifford two-qubit and multi-qubit gates become available, our findings may guide future application of RC to non-Clifford gates.

Our work is also among the first to demonstrate the practical use of a native multi-qubit gate in quantum simulation. Although the particular problem in this work would require modification to scale efficiently to larger system sizes, other quantum algorithms for computing molecular spectra with potentially improved scalability have been developed [114–119] and could benefit from the use of multipartite gates. Further, LCU as a general algorithmic framework is not limited to determining transition amplitudes in frequency-domain response properties but has broader ap-

plications in areas such as solving linear systems [137], simulating non-Hermitian dynamics [138], and preparing quantum Gibbs states [139]. Besides the LCU algorithm, quantum algorithms such as Shor's algorithm [140] and Grover's search algorithm [141] can benefit from native three-qubit gates with reduction in circuit depths and gate counts. Quantum algorithm design and implementation thus far have been mostly restricted to single- and two-qubit gates due to their ease of implementation and demonstrated high fidelities. Meanwhile, early implementations of three-qubit gates [142–144] were generally slower and more prone to leakage and decoherence compared to the iToffoli gate employed here due to populating higher levels outside the qubit computational space. However, more recent implementations of three-qubit gates [19, 145–148] have begun to address these challenges yielding fidelities approaching those achieved with two-qubit gates. Further, they have been carried out on quantum devices with tens of qubits, suggesting their utility for larger-scale quantum devices. As such native multi-qubit gates become more prevalent, our work paves the way for using them as native gate components in future quantum algorithm design and implementation.

	Pauli string transformation	Original Pauli strings	Transformed Pauli strings	Original qubit state bitstrings	Transformed qubit state bitstrings
Up-spin	$\bar{X}_{0\uparrow} \rightarrow \tilde{X}_{0\uparrow}$	$XIII$	II	$(N+1)$-electron:	$(N+1)$-electron:
	$\bar{Y}_{0\uparrow} \rightarrow \tilde{Y}_{0\uparrow}$	$iYIII$	ZI	1110, 1011,	10, 11,
	$\bar{X}_{1\uparrow} \rightarrow \tilde{X}_{1\uparrow}$	$ZZXI$	$-iYZ$	$(N-1)$-electron:	$(N-1)$-electron:
	$\bar{Y}_{1\uparrow} \rightarrow \tilde{Y}_{1\uparrow}$	$iZZYI$	$-XZ$	0100, 0001.	00, 01.
Down-spin	$\bar{X}_{0\downarrow} \rightarrow \tilde{X}_{0\downarrow}$	$ZXII$	IZ	$(N+1)$-electron:	$(N+1)$-electron:
	$\bar{Y}_{0\downarrow} \rightarrow \tilde{Y}_{0\downarrow}$	$iZYII$	ZZ	1101, 0111.	10, 11.
	$\bar{X}_{1\downarrow} \rightarrow \tilde{X}_{1\downarrow}$	$ZZZX$	iYI	$(N-1)$-electron:	$(N-1)$-electron:
	$\bar{Y}_{1\downarrow} \rightarrow \tilde{Y}_{1\downarrow}$	$iZZZY$	XI	1000, 0010	00, 01.
Spin-balanced	$Z_{0\uparrow} \rightarrow \tilde{Z}_{0\uparrow}$	$ZIII$	$-ZI$	1100,	00,
	$Z_{0\downarrow} \rightarrow \tilde{Z}_{0\downarrow}$	$IZII$	$-ZZ$	1001,	01,
	$Z_{1\uparrow} \rightarrow \tilde{Z}_{1\uparrow}$	$IIZI$	ZI	0110,	10,
	$Z_{1\downarrow} \rightarrow \tilde{Z}_{1\downarrow}$	$IIIZ$	ZZ	0011.	11.

Table 6.1: Pauli strings and qubit state bitstrings under $\mathbb{Z}_2$ transformations and truncations. Each Pauli string is characterized as up-spin or down-spin depending on whether it originates from a creation or annihilation operator applied on an up-spin or a down-spin orbital of the ground state, and is characterized as spin-balanced if it originates from a number operator applied on the ground state. The qubit state bitstrings are similarly characterized as up-spin, down-spin or spin-balanced by the type of operator that yields the state after applying on the mean-field ground state $|1100\rangle$, which are consistent with the classification based on the expectation values of the $\mathbb{Z}_2$ symmetry operators $ZIZI$ and $IZIZ$ given in the text.

Gate	Qubit(s)	Fidelity	Duration (ns)
1Q Cliffords	Q_0	0.9959	60
	Q_1	0.9949	
	Q_2	0.9956	
	Q_3	0.9973	
CZ	(Q_0, Q_1)	0.983	201
	(Q_1, Q_2)	0.987	
	(Q_2, Q_3)	0.980	
CS	(Q_1, Q_2)	0.982	151
iToffoli	(Q_0, Q_1, Q_2)	0.966	413

Table 6.2: **Gate fidelities and durations.** Single-qubit Clifford gate fidelities are measured using simultaneous randomized benchmarking [130]. Arbitrary single-qubit gates are decomposed into two real $X_{\pi/2}$ gates (duration 30 ns) and three virtual Z_ϕ gates (duration 0 ns) according to the $ZXZXZ$ decomposition. Two-qubit CZ and CS and three-qubit iToffoli gate fidelities are measured using cycle benchmarking (CB) [129]. All CB fidelities are cycle fidelities including spectator errors on idling qubits.

	Q_0	Q_1	Q_2	Q_3
T_1 (μs)	66	58	65	59
T_{2r} (μs)	38	24	39	47
T_{2e} (μs)	71	77	86	61

Table 6.3: **Qubit coherence times.** T_1 (energy decay time), T_{2r} (Ramsey dephasing time) and T_{2e} (spin echo dephasing time) for the qubits used in this work as reported in Ref. [121].

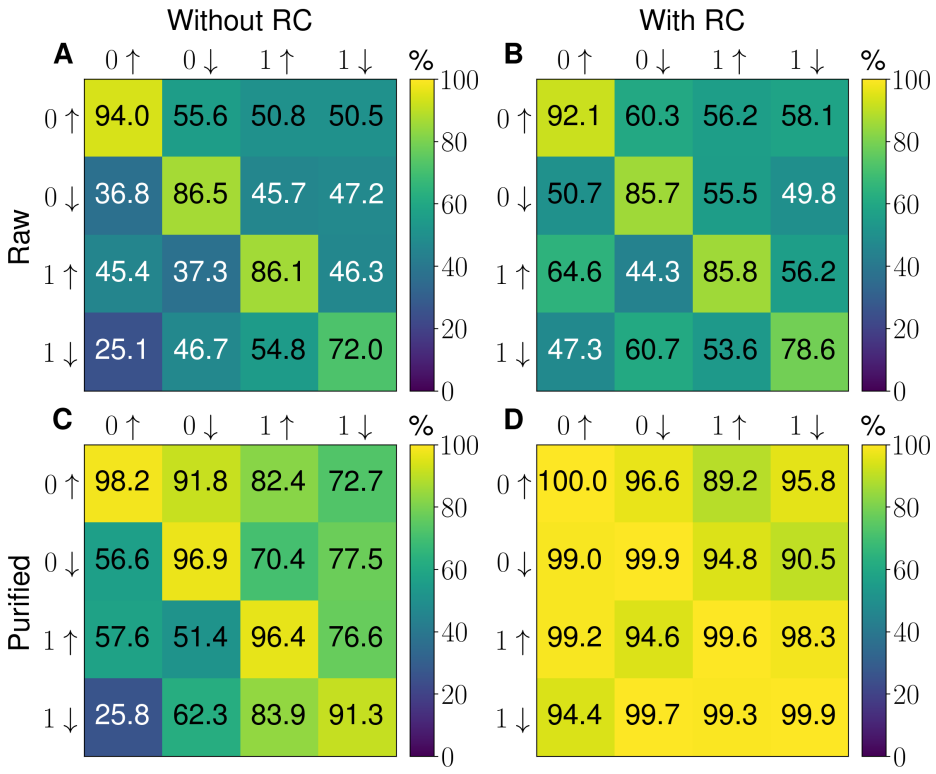

Figure 6.6: **System-qubit state fidelities in the response function calculation of NaH.** (**A** to **B**) Fidelities between the raw experimental and exact system-qubit density matrices without (A) and with RC (B). The diagonal elements correspond to system-qubit density matrices in the diagonal circuits after taking the ancilla state $a_0 = 1$, and the off-diagonal elements correspond to the system-qubit density matrices in the off-diagonal circuits after taking the ancilla states either as $(a_0, a_1) = (1, 0)$ (upper diagonal) or as $(a_0, a_1) = (1, 1)$ (lower diagonal). (**C** to **D**) Fidelities between the purified experimental and exact system-qubit density matrices without (C) and with RC (D). Layout of the tiles are the same as in panels (A) and (B). Without RC, purification raises the average off-diagonal fidelity from 45.2% to 67.4%, but with both RC and purification the average off-diagonal fidelity increases to 96.0%.

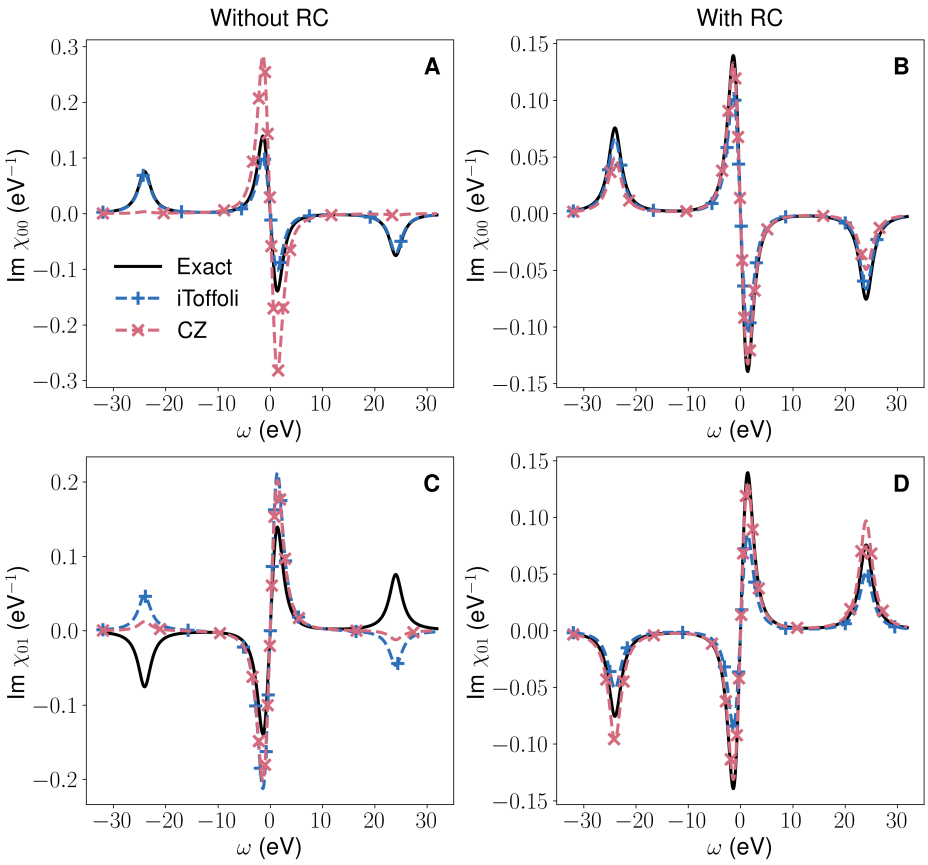

Figure 6.7: **Density-density response function of NaH**. (A) Im χ_{00} without RC. (B) Im χ_{00} with RC. (C) Im χ_{01} without RC. (D) Im χ_{01} with RC. All experimental results are postprocessed with McWeeny purification on the system-qubit states after constraining to the ancilla bitstring subspace. A broadening factor of $\eta = 1.5$ eV is used to produce the spectra. Without RC, the iToffoli decomposition yields qualitatively better results compared to the CZ decomposition. After RC is applied, the two decompositions yield comparable results.

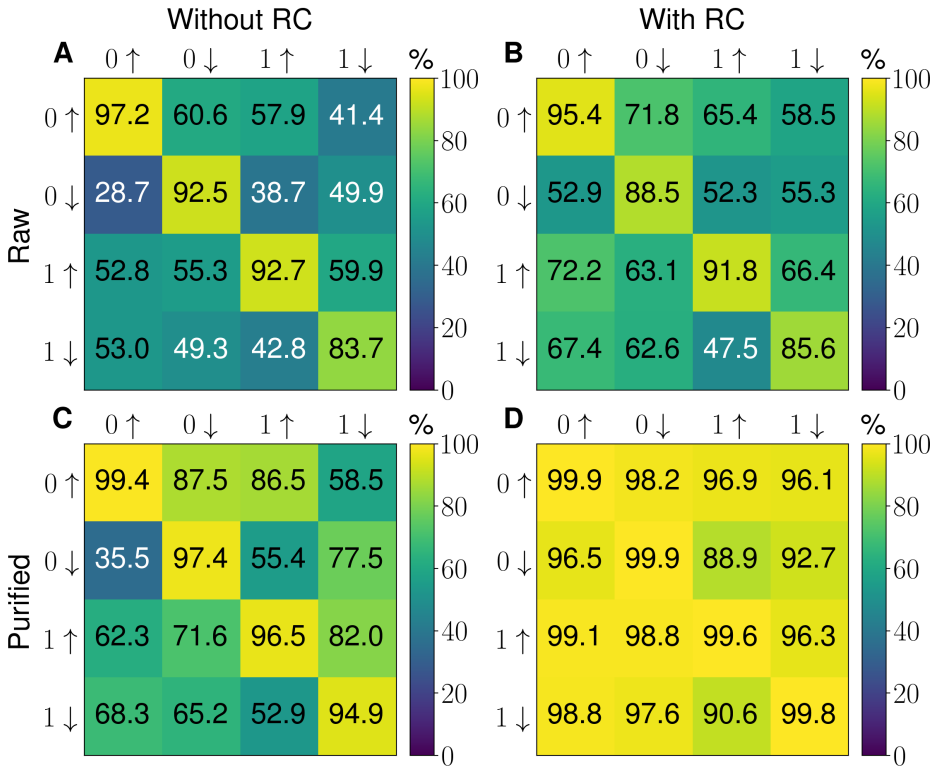

Figure 6.8: **System-qubit state fidelities for the response function calculation of KH.** (**A** to **B**) Fidelities between the raw experimental and exact system-qubit density matrices without (A) and with RC (B). (**C** to **D**) Fidelities between the purified experimental and exact system-qubit density matrices without (C) and with RC (D). Layout of the tiles in each panel is the same as in Fig. 5 in the main text. Similar to NaH, without RC, purification raises the average off-diagonal fidelity from 49.2% to 66.9%, but with both RC and purification the average off-diagonal fidelity increases to 95.9%.

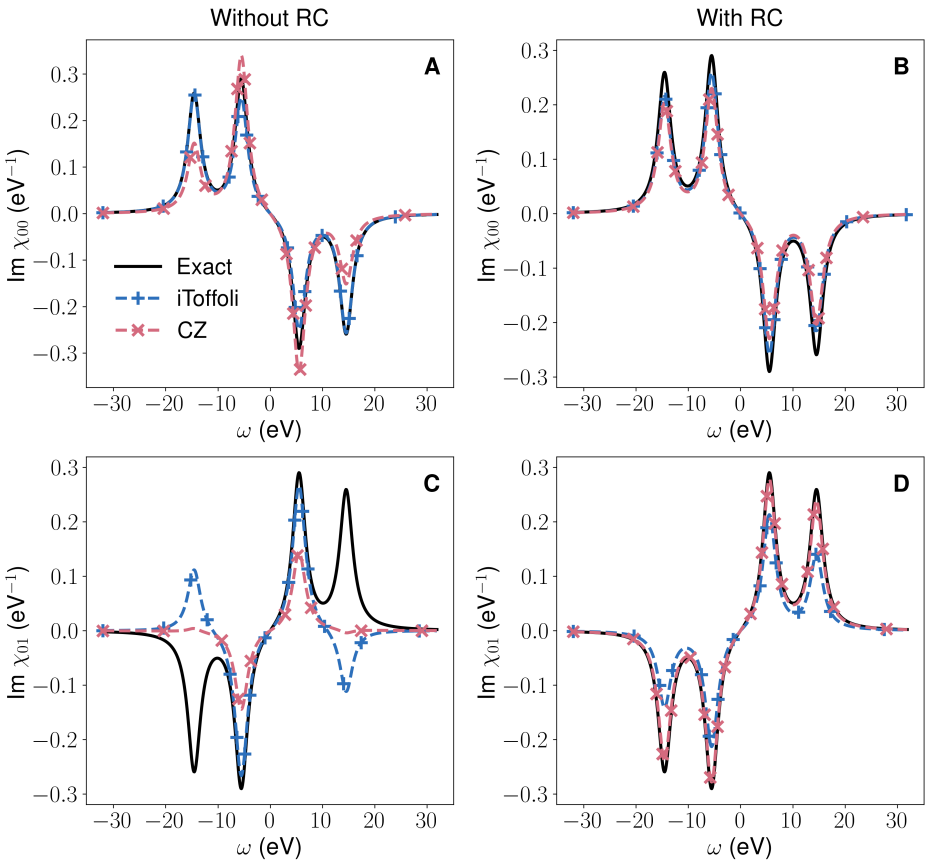

Figure 6.9: **Density-density response function of KH**. (A) Im χ_{00} without RC. (B) Im χ_{00} with RC. (C) Im χ_{01} without RC. (D) Im χ_{01} with RC. All experimental results are postprocessed with McWeeny purification on the system-qubit states after constraining to the ancilla bitstring subspace. A broadening factor of $\eta = 1.5$ eV is used to produce the spectra. Similar to NaH, the iToffoli decomposition yields qualitatively better results compared to the CZ decomposition in the absence of RC. After RC is applied, results from the two decompositions are comparable.

Chapter 7

MEASUREMENT-INDUCED STATE PREPARATION

7.1 Introduction

Recently, there has been a renewed interest in measurement-based quantum computation [149–152]. Compared to the traditional approach of performing unitary evolution on an initial quantum state, measurement-based quantum computation processes quantum information by adaptive measurements on highly entangled states, where the state to be measured is called the resource state [153]. Compared to the conventional approach where time evolution is applied on a quantum computer, measurement-based quantum computation has the benefit of circumventing deep quantum circuits. Measurement on cluster states has been shown to generate states with long-range entanglement such as the Greenberg-Horne-Zeilinger (GHZ) state or states with certain topological orders [154–157].

Meanwhile, the limitations of existing quantum hardware have spurred a surge of interest in the development of software for quantum circuit simulation. There are two main approaches to simulating quantum circuits: state vector simulation, which represents the quantum state in its full state-vector form, and tensor network simulation, which constructs the quantum state approximately with tensor networks. Recently developed high-performance simulators for the state-vector approach include the Intel Quantum Simulator [158], the qsim simulator [159], and the cuStateVec library in cuQuantum [24]. However, the state-vector approach requires exponential storage space for the quantum state and thus suffers from memory issues. On the other hand, tensor networks have been demonstrated to efficiently simulate quantum circuits without exponential memory requirements [11]. A series of software packages for tensor network simulations have been developed in recent years, including Quimb [85], TensorNetwork [160], ExaTN [161], TensorCircuit [162] and the cuTensorNet library in cuQuantum [24]. In particular, the cuTensorNet library leverages the power of graphical processing units (GPUs), which has been an indispensable component in the recent advancements in fields such as machine learning [163].

Here, we use tensor network methods to carry out a quantum simulation protocol [23] that reproduces phase transition in random-bond Ising models (RBIMs) [164]

from cluster states [153]. Although a similar protocol has been formulated [165] and implemented [166] on quantum hardware, the insight of the current protocol in Ref. [23] is that we can perform decoding instead of post-selection on the measured bitstrings to uncover hidden phases in the quantum state. Equipped with the high-performance simulation library cuTensorNet [24] on GPUs, we perform simulation on the bipartite Lieb lattice on up to 176 qubits. In one dimension (1D), we compute the correlation functions and extract the correlation lengths; in two dimensions (2D), we compute the ferromagnetic susceptibilities and observe the phase transition from the ferromagnetic phase to the paramagnetic phase along the Nishimori line [164].

This chapter proceeds as follows. In Sec. 7.2, we present the quantum simulation protocol for observing phase transition in RBIM from Ref. [23] and the tensor network implementation details. Next, we show the results on 1D and 2D cluster states in Sec. 7.3, focusing on correlation lengths in 1D and ferromagnetic susceptibilities in 2D. In Sec. 7.4, we discuss the broader context and implication of this work with regards to tensor network-based simulation of quantum computation protocols.

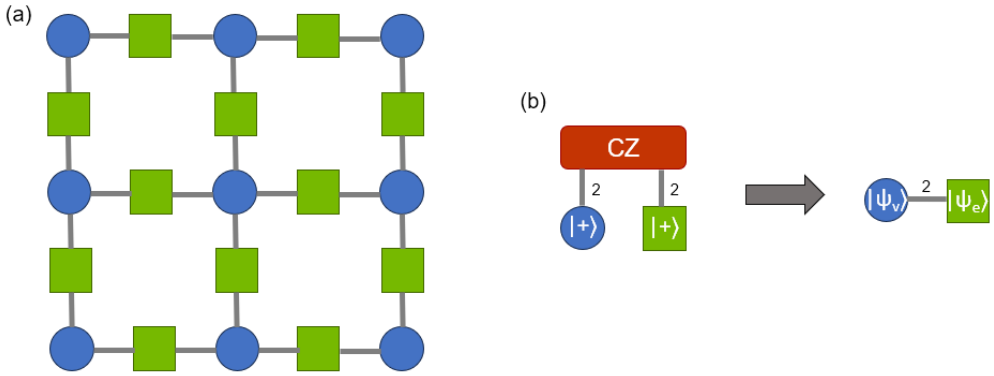

Figure 7.3: (a) 2D Lieb lattice where each vertex (blue circle) or edge (green square) represents a qubit. The gray lines connecting a vertex qubit with an adjacent edge qubit represent the bond between two qubits, which is at most dimension 2 in the cluster state. The edge qubits are measured with angle θ away from the X-basis while the vertex qubits are measured in the Z-basis. The measured bitstrings are decoded according to the protocol introduced in Ref. [23] before computing physical observables. (b) Application of the entangling CZ gates to adjacent qubits initialized in the $|+\rangle$ state. Initially there is no bond between a vertex qubit and its adjacent edge qubit. After CZ gates are applied on all qubits, the maximum bond dimension is 2 without any truncation error.

7.2 Methods

Quantum Protocol

The simulations in this work follow the protocol introduced in Ref. [23]. We first build a cluster state on a 1D or 2D Lieb lattice as in Fig. 7.1, where the 1D lattice is divided into the sublattice on all odd sites and the sublattice on all even sites, and the 2D lattice is divided into the sublattice on all vertex sites and the sublattice on all edge sites. For simplicity of notation, we will denote the sublattice of odd or vertex sites as $\mathcal{V}$ and the sublattice of even or edge sites as $\mathcal{E}$. The measurement results on the $\mathcal{V}$ sublattice are denoted as $\{\sigma_v\}_{v\in\mathcal{V}}$, and those on the $\mathcal{E}$ sublattice are denoted as $\{s_e\}_{e\in\mathcal{E}}$. We will use the notation $v \in e$ to indicate that the vertex v is part of the edge e and hence the qubit at v is adjacent to the qubit at e.

Initially, a Hadamard gate is applied to convert each qubit in $\mathcal{V}$ and $\mathcal{E}$ to the $|+\rangle$ state. CZ gates are then applied to all adjacent v-e qubit pairs to create the cluster state. To measure qubits of the $\mathcal{E}$ sublattice in the basis tilted by θ from the X-basis, an $R_y(\pi/2-\theta)$ gate is applied to each qubit of the $\mathcal{E}$ sublattice so that when $\theta = 0$, the qubits are measured in the X-basis, and when $\theta = \pi/2$, the qubits are meausred in the Z-basis.

In the parameter regime under study, the measurement angle range of $\theta = 0$ to $\theta = \pi/2$ corresponds to an antiferromagnetic bond probability of $p_- < 1/2$. However, the output state in the quantum simulation protocol exhibits no preference of ferromagnetic bonds over antiferromagnetic bonds. In order to recover the hidden ferromagnetic order in RBIM from the quantum state, we need to convert each obtained measurement outcome to the one with the least number of ferromagnetic bonds, while preserving fluxes m_p around each plaquette defined as

$$m_p = \prod_{e\in p} s_e, \tag{7.1}$$

where p is a plaquette or a non-contractible loop (in 1D, the loop corresponds to the line extending through all the $\mathcal{E}$ sublattice). The flux configurations are preserved by attaching gauges to the $\mathcal{V}$ sublattice such that

$$\sigma_v \to \tilde{\sigma}_v = t_v\sigma_v, \quad s_e \to \tilde{s}_e = \left(\prod_{v\in e} t_v\right) s_e. \tag{7.2}$$

The problem of finding the equivalent configuration with the smallest number of ferromagnetic bonds can be mapped to the error syndrome decoding problem in quantum error correcting codes [167], where we can use the minimum weight perfect matching (MWPM) algorithm [168] for efficient decoding without exponential computational resources.

After the decoding process which produces the gauges $\{t_i\}$, the observables can be computed with the decoded values $\{\tilde{\sigma}_v\}$ in the corresponding formulas. Although phase transition is not present in 1D RBIM, we can compute the ZZ-correlation function $C_n \equiv \langle Z_1 Z_{2n+1} \rangle$ on the even sites and extract the correlation length ξ. The correlation function C_n has the expression:

$$C_n \equiv \langle Z_1 Z_{2n+1} \rangle = \frac{\prod_{m=1}^{n} s_{2m} (\cos\theta)^n + \prod_{m=n+1}^{N} s_{2m} (\cos\theta)^{N-n}}{1 + \left(\prod_{m=1}^{N} s_{2m} \right) (\cos\theta)^N} \longrightarrow e^{-n/\xi}, \tag{7.3}$$

$$\xi = -\ln \cos\theta. \tag{7.4}$$

In 2D RBIM, there is a phase transition from the ferromagnetic phase to the paramagnetic phase. Along the Nishimori line [164], the antiferromagnetic bond probability at the transtion point p^* was determined numerically to be 0.109 [169], which corresponds to a measurement angle $\theta^* = 38.6^\circ$ in the quantum computation protocol. We use the ferromagnetic susceptibility χ as the order parameter for the phase transition:

$$\langle \chi \rangle = \frac{1}{N_v} \sum_{v,v' \in \mathcal{V}} \langle Z_v Z_{v'} \rangle. \tag{7.5}$$

To compute the variance of χ, we need the quantities $\langle \chi \rangle$ and $\langle \chi^2 \rangle$. In practice, we only compute the unique vertex pairs $i \leftrightarrow j$. The equations for $\langle \chi \rangle$ and $\langle \chi^2 \rangle$ are thus given by

$$\langle \chi \rangle = \frac{1}{N_v} \sum_{\boldsymbol{\sigma}} P(\boldsymbol{\sigma}) \sum_{ij} (Z_i Z_j)_{\boldsymbol{\sigma}} \tag{7.6}$$

$$= \sum_{\boldsymbol{\sigma}} P(\boldsymbol{\sigma}) \left(1 + \frac{2}{N_v} \sum_{i \leftrightarrow j} (Z_i Z_j)_{\sigma} \right), \tag{7.7}$$

$$\langle \chi^2 \rangle = \frac{1}{N_v^2} \sum_{\boldsymbol{\sigma}} P(\boldsymbol{\sigma}) \sum_{ijkl} (Z_i Z_j Z_k Z_l)_{\boldsymbol{\sigma}} \tag{7.8}$$

$$= \sum_{\boldsymbol{\sigma}} P(\boldsymbol{\sigma}) \left[1 + \frac{2}{N_v} \sum_{i \leftrightarrow j} (Z_i Z_j)_{\sigma} \right] \left[1 + \frac{2}{N_v} \sum_{k \leftrightarrow l} (Z_k Z_l)_{\sigma} \right] \tag{7.9}$$

$$= \sum_{\boldsymbol{\sigma}} P(\boldsymbol{\sigma}) \left[1 + \frac{2}{N_v} \sum_{i \leftrightarrow j} (Z_i Z_j)_{\sigma} \right]^2 \tag{7.10}$$

Implementation Details

We use tensor network methods to carry out the present quantum simulation protocol. The tensor network is constructed with a 2D Lieb lattice structure where each lattice site contains a tensor (the 1D lattice is simply obtained by setting one of the two dimensions to 1). The total number of tensor elements increases after the application of entangling CZ gates, in which case the composite tensor need to be decomposed with singular value decomposition (SVD) where the middle bond can be truncated, as illustrated in Fig. 7.2. The bond dimension is maintained at 2 throughout the construction of the cluster state and the application of R_y gates before measurements.

Measurement on the quantum state is implemented with the standard numerical simulation procedure of computing the marginal distribution on a subset of qubits, sampling bitstrings on the subset of qubits, and fixing these qubits to the sampled bitstrings before proceeding to sample the next subset of qubits, until all qubits have been sampled [85]. The number of qubits in the subset during the sampling iterations, which is a parameter called the group size, is set to 4 in our simulations. Each circuit is sampled 1000 times to obtain the bitstrings. Additionally, as the norm of the intermediate tensor networks under study experiences super-exponential decreases, we multiply a factor to all tensors in the network in order to avoid underflow in the probabilities when sampling each subset of qubits.

The simulations are executed on NVIDIA H100 GPUs hosted at Caltech's High-Performance Computing Cluster. We use the `GateSplit` algorithm from the cuTensorNet library [24] to perform the combined step of contracting two site tensors (one on a vertex qubit and the other on an edge qubit) and one gate tensor followed by

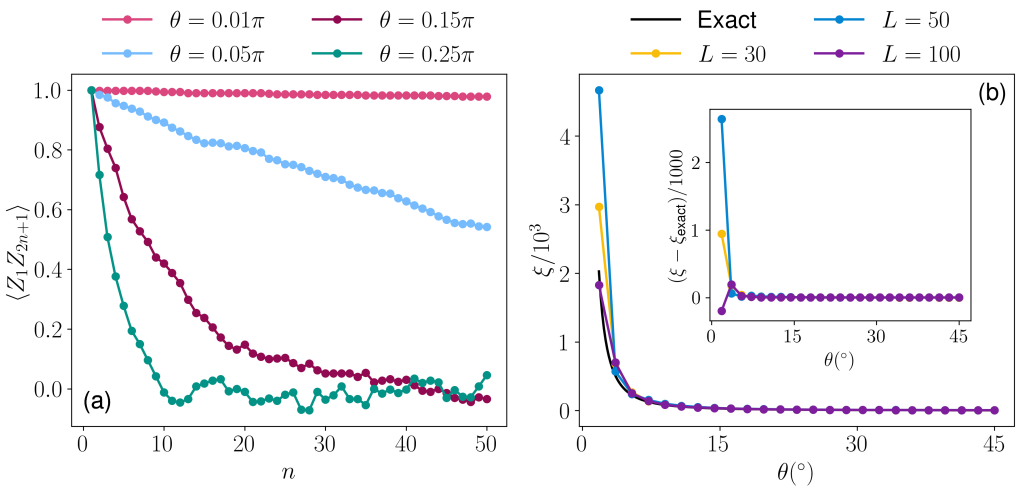

Figure 7.6: (a) Correlation function $\langle Z_1 Z_{2n+1} \rangle$ as a function of site separation n on 1D $L = 50$ lattice. The correlation function is plotted for four angles $\theta = 0.01\pi, 0.05\pi, 0.15\pi, 0.25\pi$. In the thermodynamic limit, the correlation function should follow an exponential decay. The state on the odd sites starts from a GHZ state at $\theta = 0$ to a product state at $\theta = \pi/2$, and therefore we see a more rapid exponential decay as θ increases. (b) Correlation lengths ξ from fitting the correlation function to the analytical result $e^{-n/\xi}$ for $L = 30, 50, 100$. For each L, we use the first 1/5 of site separation in the correlation function $\langle Z_1 Z_{2n+1} \rangle$ data for the nonlinear least-square fit. The exact result reflects the analytical expression of the correlation length $\xi = -\ln \cos \theta$ from the protocol. The inset displays the difference between the simulated and exact correlation lengths. Although the simulated correlation lengths are expected to match better with the exact correlation lengths when L increases, we observe the best agreement with the exact result at $L = 100$ but $L = 50$ has worse agreement compared to $L = 30$.

decomposition and truncation of the middle bond. In the bitstring sampling process, contraction of the full tensor network to marginal tensor networks is also performed through the cuTensorNet library. Data in the tensors are managed through the NumPy library [170] on CPU and through the CuPy library [171] on GPU. We use the PyMatching library [172] to decode the measured bitstrings with the MWPM algorithm.

7.3 Results

1D Cluster States

In Fig. 7.4, we present the correlation function $\langle Z_1 Z_{2n+1} \rangle$ as a function of site separation n on a 1D lattice with a size of $L = 50$. The correlation function is displayed at four distinct angles: $\theta = 0.01\pi, 0.05\pi, 0.15\pi, 0.25\pi$. In the thermodynamic

limit, the correlation function is expected to exhibit an exponential decay, with a more rapid decay for larger measurement angle θ since the state evolves from an maximally entangled GHZ state at $\theta = 0$ to a completely unentangled product state at $\theta = 0.5\pi$. Indeed, we observe an almost constant value when $\theta = 0.01\pi$ and sequentially more rapid decay as θ proceeds to $0.05\pi, 0.15\pi$ and 0.25π. The trend we see in the correlation function agrees with the theoretical prediction.

Figure 7.5 shows the correlation lengths ξ obtained through non-linear least-square fit of the correlation function to the analytical result $e^{-n/\xi}$ for lattice sizes $L = 30, 50, 100$. To minimize finite-size effect, we utilize only the first 1/5 of site separation in the correlation function $\langle Z_1 Z_{2n+1} \rangle$ data for each L to avoid the parameter regime where n is close to L. The exact correlation length, derived from the analytical expression $\xi = -\ln \cos \theta$ inherent in the protocol, serves as a benchmark for comparison. The inset of the figure illustrates the disparity between the simulated and exact correlation lengths. While an overall improvement in agreement is anticipated as L increases, we first observe the best agreement for $L = 100$, showing a convergence towards the exact result. However, the agreement for $L = 50$ is less accurate compared to $L = 30$. This discrepancy prompts further investigation into the interplay between lattice size, correlation length, and the protocol parameters.

2D Cluster States

Moving to two dimensions, Fig. 7.7 illustrates the ferromagnetic susceptibility χ as a function of the measurement angle θ on a 2D lattice with $L = 4, 5, 6, 7, 8$. The χ values are normalized by dividing by L^2 to facilitate comparisons across different Ls. The dashed black line represents the theoretically predicted phase transition angle of 38.6° in RBIM. The data exhibits the expected behavior as $\chi/L^2 = 1$ on the GHZ state at $\theta = 0$ and progresses to $\chi/L^2 = 0$ on the product state at $\theta = 90°$. This alignment with theoretical predictions underscores the qualitative accuracy of our simulated results.

Continuing our exploration of the 2D model, Fig. 7.8 shows the normalized variance of the ferromagnetic susceptibility as a function of the measurement angle θ for various lattice sizes, specifically $L = 4, 5, 6, 7, 8$. The dashed black line corresponds to the theoretically predicted phase transition angle of $\theta^* = 38.6°$ in the 2D RBIM [169]. The variance of χ is expected to exhibit a divergence at the critical point as predicted by theoretical analysis and numerical simulations. While the peaks of $\mathrm{Var}(\chi)$ show slight deviations from the exact transition angle θ^* at $L = 4$ and

5, for simulated data with $L = 6, 7, 8$, all peaks align precisely at θ^*, with peak height increasing alongside the lattice size L. This convergence towards the exact transition angle suggests a scaling behavior indicative of the critical phenomena.

7.4 Discussion

In this study, we employed tensor network methods to explore the measurement-induced preparation of quantum states corresponding to phase transition along the Nishimori line in RBIM. Our investigation marked an initial stride in the exploration of measurement-induced state preparation from cluster states using tensor network simulators on GPUs.

While our study successfully employed tensor network methods to reproduce phase transition along the Nishimori line in 2D RBIM, it is crucial to acknowledge inherent inefficiencies in the current tensor network implementation. These inefficiencies highlight the need for future refinements and optimizations in the algorithm. Additionally, our exploration does not extend to multi-GPU configurations, representing an unexplored direction in our approach. The potential of multi-GPU architectures could significantly enhance computational efficiency, addressing existing concerns and paving the way for more scalable simulations of quantum systems. Future research endeavors should investigate both the optimization of tensor network implementation and the exploration of multi-GPU configurations to further improve the robustness and efficiency of the methodology in studying complex quantum phenomena.

Furthermore, we should note a significant aspect that has not been addressed in our study: the incorporation of noise into the simulation. As real-world quantum systems are inevitably subject to various sources of noise, the incorporation of noise into the simulation is crucial for a more accurate representation of experimental conditions and have implications on whether the phase transition can be accurately reproduced on real quantum hardware. Future research should aim to integrate noise modeling into the simulation framework, providing a more realistic portrayal of the quantum protocols when executed on quantum hardware and enriching the insights derived from our study.

In conclusion, our investigation into phase transition phenomena in RBIM prepared from cluster states through tensor network methods lays the groundwork for future explorations in measurement-induced state preparation. While we acknowledge the limitations in the current implementation, including inefficiencies in the ten-

sor network method, the unexplored realm of multi-GPU configurations, and the absence of noise in our simulations, these aspects present avenues for refinement and expansion in future work. Importantly, the applicability of our tensor network simulation approach extends beyond the scope of this study, as it can be harnessed to explore other measurement-induced protocols in the future. As the field of measurement-based quantum computation continues to evolve, these avenues offer prospects for further advancements in quantum research and the exploration of novel measurement-induced protocols using tensor network simulations.

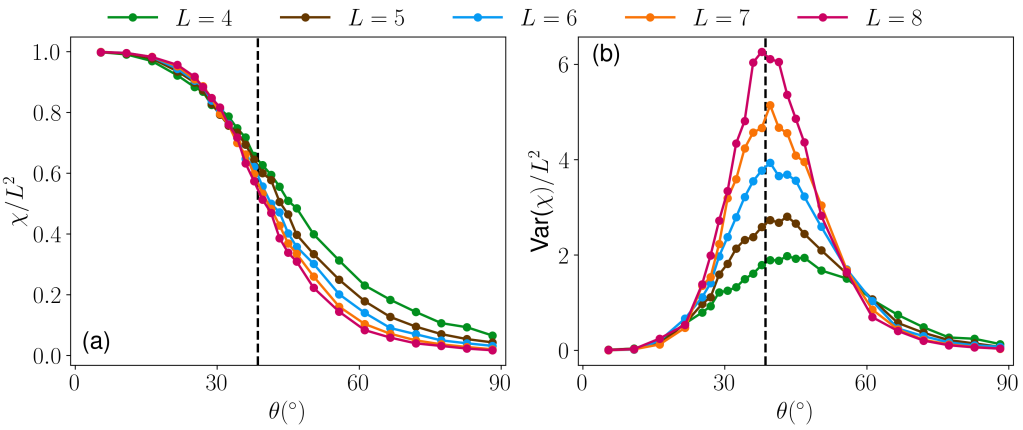

Figure 7.9: (a) Ferromagnetic susceptibility χ normalized by L^2 as a function of the measurement angle θ on the 2D lattice with $L = 4, 5, 6, 7, 8$. The dashed black line corresponds to the theoretical RBIM phase transition angle 38.6°. In theory, $\chi/L^2 = 1$ on the maximally entangled GHZ state when $\theta = 0$ and $\chi/L^2 = 0$ on the completely disentangled product state when $\theta = 90°$, which is what we observe from the simulated data. (b) Variance of the ferromagnetic susceptibility Var(χ) divided by L^2 as a function of measurmeent angle θ on the 2D lattice with $L = 4, 5, 6, 7, 8$. The dashed black line corresponds to the theoretical RBIM phase transition angle 38.6°. Variance of χ is expected to diverge at the critical point. Although the peaks of Var(χ) exhibit small deviations from the exact transition angle θ^*, the simulated data with $L = 6, 7, 8$ all peak at θ^* with peak height increasing with the lattice size L.

Chapter 8

CONCLUSION AND OUTLOOK

This thesis delved into leveraging near-term quantum computers for simulating properties of quantum many-body systems especially within the linear response framework. Through two experimental demonstrations of quantum simulation on current quantum hardware, one on the finite-temperature properties of spin models and the other on the frequency-domain response properties of molecular models, we showed the current capabilities of superconducting quantum devices in simulating many-body physics and how error mitigation techniques can further improve the computed physical observables. Additionally, we used tensor network methods to carry out a protocol for preparing quantum states and observed the phase transition in the random-bond Ising model (RBIM). We found that with the latest tensor network simulation libraries targeting graphical processing units (GPUs), we can execute simulations on a scale that was not possible previously.

Our first work showed that finite-temperature properties of few-site spin systems, in particular finite-temperature dynamical properties that require both real and imaginary time evolutions, are accessible on current quantum hardware. The quantum imaginary time evolution (QITE) algorithm, improved by strategies to mitigate errors and reduce quantum resources, is demonstrated to have the capability of computing finite-temperature properties such as energy, correlation functions, and spectral densities. Accurate simulations on two sites are achieved by maintaining constant-depth circuits in both QITE and real-time evolution. On four sites, we observed reasonable agreement in finite-temperature observables at high temperature using circuit recompilation techniques. However, as we enter the regime of low temperature, which corresponds to long imaginary time, the observables determined from quantum hardware exhibit relatively large discrepancies with the exact results, indicating the need for more effective quantum resource reduction schemes. The evaluation of thermal properties on reduced density matrices and the use of stochastic trace evaluation as an alternative to full trace evaluation solidified the scalability of our approach. With the availability of more qubits on quantum hardware, our work lays the foundation for future scalable implementation of the QITE algorithm for computing finite-temperature observables.

Our second investigation harnessed a high-fidelity iToffoli gate to implement an algorithm based on linear combination of unitaries (LCU) to compute Green's functions and density-density response functions of diatomic molecules on a superconducting quantum processor. This work is among the first to demonstrate the practical use of a native multi-qubit gate in quantum simulation. The iToffoli gate enabled the reduction of circuit depths by $\sim 50\%$ and circuit execution times by $\sim 40\%$. Our results highlighted the importance of error-mitigation techniques in the LCU-based algorithm. In particular, randomized compilation (RC) and McWeeny purification when applied separately only improved the raw experimental data to a limited extent. However, the combination of RC and McWeeny purification resulted in a substantial improvement, with system-qubit state fidelities averaging over 96.0%. The versatility of the LCU algorithm extends beyond computing transition amplitudes in response functions, with potential applications to solving linear systems, simulating non-Hermitian dynamics, and preparing quantum Gibbs states. As native multi-qubit gates become more available on quantum hardware, our study anticipates their incorporation as native gate components into future design and implementation of quantum algorithms.

In the third study, tensor network methods were employed to investigate the measurement-induced preparation of states corresponding to certain phases of the RBIM. In one dimension, we computed the correlation function and observed the transition from the ferromagnetic phase to the paramagnetic phase where the correlation length determined from the non-linear least-square fit approaches the exact value as the number of sites increases. In two dimensions, we computed the ferromagnetic susceptibility and observed the transition from the ferromagnetic phase to the paramagnetic phase where the critical phase transition angle agrees with the value determined from theoretical analysis. This exploration represents an initial foray into understanding measurement-induced state preparation from cluster states. However, inherent inefficiencies in the current tensor network implementation and the unexplored dimension of multi-GPU configurations underscore the need for future refinements and optimizations. The absence of noise modeling in our investigation emphasizes a crucial avenue for future research to bridge the gap between theoretical simulations and real-world quantum systems. Despite these limitations, our study lays the groundwork for future explorations in measurement-based quantum computation, showing the versatility of tensor network simulations and their potential applications in understanding measurement-induced protocols in quantum information processing and computation.

In conclusion, this thesis explored the potential of near-term quantum computers to simulate properties of quantum many-body systems within the linear response framework. Through experimental demonstrations on current quantum hardware, we investigated finite-temperature properties of spin models and frequency-domain response properties of molecular models. These studies highlighted the capabilities and limitations of superconducting quantum devices and the significant role of error mitigation techniques in improving physical observables. The application of tensor network methods enabled the preparation and analysis of quantum states, revealing critical phase transitions in the RBIM and demonstrating the scalability of these methods using GPU-based libraries. Collectively, these investigations pave the way for future research in quantum simulations, emphasizing the importance of continuous advancements in hardware capabilities, error mitigation strategies, and algorithmic innovations to realize the full potential of quantum computing in studying complex quantum systems.

BIBLIOGRAPHY

[1]R. P. Feynman, "Simulating physics with computers", Int. J. Theor. Phys. **21**, 467–488 (1982).

[2]M. Kjaergaard, M. E. Schwartz, J. Braumüller, P. Krantz, J. I.-J. Wang, S. Gustavsson, and W. D. Oliver, "Superconducting Qubits: Current State of Play", Annual Review of Condensed Matter Physics **11**, 369–395 (2020).

[3]C. D. Bruzewicz, J. Chiaverini, R. McConnell, and J. M. Sage, "Trapped-ion quantum computing: Progress and challenges", Applied Physics Reviews **6**, 021314 (2019).

[4]M. Cerezo, A. Arrasmith, R. Babbush, S. C. Benjamin, S. Endo, K. Fujii, J. R. McClean, K. Mitarai, X. Yuan, L. Cincio, and P. J. Coles, "Variational quantum algorithms", Nat Rev Phys **3**, 625–644 (2021).

[5]K. Bharti, A. Cervera-Lierta, T. H. Kyaw, T. Haug, S. Alperin-Lea, A. Anand, M. Degroote, H. Heimonen, J. S. Kottmann, T. Menke, W.-K. Mok, S. Sim, L.-C. Kwek, and A. Aspuru-Guzik, "Noisy intermediate-scale quantum algorithms", Rev. Mod. Phys. **94**, 015004 (2022).

[6]D. Herman, C. Googin, X. Liu, Y. Sun, A. Galda, I. Safro, M. Pistoia, and Y. Alexeev, "Quantum computing for finance", Nat Rev Phys **5**, 450–465 (2023).

[7]K. Wintersperger, F. Dommert, T. Ehmer, A. Hoursanov, J. Klepsch, W. Mauerer, G. Reuber, T. Strohm, M. Yin, and S. Luber, "Neutral atom quantum computing hardware: performance and end-user perspective", EPJ Quantum Technol. **10**, 32 (2023).

[8]S. McArdle, S. Endo, A. Aspuru-Guzik, S. C. Benjamin, and X. Yuan, "Quantum computational chemistry", Rev. Mod. Phys. **92**, 015003 (2020).

[9]E. Farhi, J. Goldstone, and S. Gutmann, *A Quantum Approximate Optimization Algorithm*, Nov. 2014.

[10]A. W. Harrow, A. Hassidim, and S. Lloyd, "Quantum algorithm for linear systems of equations", Phys. Rev. Lett. **103**, 150502 (2009).

[11]I. L. Markov and Y. Shi, "Simulating quantum computation by contracting tensor networks", SIAM Journal on Computing **38**, 963–981 (2008).

[12]X. Yuan, J. Sun, J. Liu, Q. Zhao, and Y. Zhou, "Quantum Simulation with Hybrid Tensor Networks", Phys. Rev. Lett. **127**, 040501 (2021).

[13]A. L. Fetter and J. D. Walecka, *Quantum theory of many-particle systems* (Dover Publications, Mineola, N.Y, 2003).

[14]L. S. Cederbaum, "One-body Green's function for atoms and molecules: theory and application", J. Phys. B: At. Mol. Phys. **8**, 290–303 (1975).

[15]G. Ortiz, J. E. Gubernatis, E. Knill, and R. Laflamme, "Quantum algorithms for fermionic simulations", Phys. Rev. A **64**, 022319 (2001).

[16]R. Somma, G. Ortiz, J. E. Gubernatis, E. Knill, and R. Laflamme, "Simulating physical phenomena by quantum networks", Phys. Rev. A **65**, 042323 (2002).

[17]M. Motta, C. Sun, A. T. K. Tan, M. J. O'Rourke, E. Ye, A. J. Minnich, F. G. S. L. Brandão, and G. K.-L. Chan, "Determining eigenstates and thermal states on a quantum computer using quantum imaginary time evolution", Nat. Phys., 10.1038/s41567-019-0704-4 (2019).

[18]D. Gottesman, "Theory of fault-tolerant quantum computation", Phys. Rev. A **57**, 127–137 (1998).

[19]Y. Kim, A. Morvan, L. B. Nguyen, R. K. Naik, C. Jünger, L. Chen, J. M. Kreikebaum, D. I. Santiago, and I. Siddiqi, "High-fidelity three-qubit iToffoli gate for fixed-frequency superconducting qubits", Nat. Phys. **18**, 783–788 (2022).

[20]A. M. Childs and N. Wiebe, "Hamiltonian simulation using linear combinations of unitary operations", Quantum Inf. Comput. **12**, 901–924 (2012).

[21]T. Kosugi and Y.-i. Matsushita, "Linear-response functions of molecules on a quantum computer: Charge and spin responses and optical absorption", Phys. Rev. Res. **2**, 033043 (2020).

[22]T. Kosugi and Y.-i. Matsushita, "Construction of Green's functions on a quantum computer: Quasiparticle spectra of molecules", Phys. Rev. A **101**, 012330 (2020).

[23]J. Y. Lee, W. Ji, Z. Bi, and M. P. A. Fisher, *Decoding measurement-prepared quantum phases and transitions: from ising model to gauge theory, and beyond*, 2022.

[24]H. Bayraktar, A. Charara, D. Clark, S. Cohen, T. Costa, Y.-L. L. Fang, Y. Gao, J. Guan, J. Gunnels, A. Haidar, A. Hehn, M. Hohnerbach, M. Jones, T. Lubowe, D. Lyakh, S. Morino, P. Springer, S. Stanwyck, I. Terentyev, S. Varadhan, J. Wong, and T. Yamaguchi, *cuQuantum SDK: A High-Performance Library for Accelerating Quantum Science*, arXiv:2308.01999 [quant-ph], Aug. 2023.

[25]https://qiskit.org/documentation/stubs/qiskit.circuit.library.U3Gate.html.

[26]D. C. McKay, C. J. Wood, S. Sheldon, J. M. Chow, and J. M. Gambetta, "Efficient Z gates for quantum computing", Phys. Rev. A **96**, 022330 (2017).

[27]https://cirq.readthedocs.io/en/stable/generated/cirq.PhasedXZGate.html.

[28]F. Arute, K. Arya, R. Babbush, D. Bacon, J. C. Bardin, R. Barends, R. Biswas, S. Boixo, F. G. S. L. Brandao, D. A. Buell, B. Burkett, Y. Chen, Z. Chen, B. Chiaro, R. Collins, W. Courtney, A. Dunsworth, E. Farhi, B. Foxen, A. Fowler, C. Gidney, M. Giustina, R. Graff, K. Guerin, S. Habegger, M. P. Harrigan, M. J. Hartmann, A. Ho, M. Hoffmann, T. Huang, T. S. Humble, S. V. Isakov, E. Jeffrey, Z. Jiang, D.

Kafri, K. Kechedzhi, J. Kelly, P. V. Klimov, S. Knysh, A. Korotkov, F. Kostritsa, D. Landhuis, M. Lindmark, E. Lucero, D. Lyakh, S. Mandrà, J. R. McClean, M. McEwen, A. Megrant, X. Mi, K. Michielsen, M. Mohseni, J. Mutus, O. Naaman, M. Neeley, C. Neill, M. Y. Niu, E. Ostby, A. Petukhov, J. C. Platt, C. Quintana, E. G. Rieffel, P. Roushan, N. C. Rubin, D. Sank, K. J. Satzinger, V. Smelyanskiy, K. J. Sung, M. D. Trevithick, A. Vainsencher, B. Villalonga, T. White, Z. J. Yao, P. Yeh, A. Zalcman, H. Neven, and J. M. Martinis, "Quantum supremacy using a programmable superconducting processor", Nature **574**, 505–510 (2019).

[29]J. D. Whitfield, J. Biamonte, and A. Aspuru-Guzik, "Simulation of electronic structure Hamiltonians using quantum computers", Mol. Phys. **109**, 735–750 (2011).

[30]A. Chiesa, F. Tacchino, M. Grossi, P. Santini, I. Tavernelli, D. Gerace, and S. Carretta, "Quantum hardware simulating four-dimensional inelastic neutron scattering", Nat. Phys. **15**, 455–459 (2019).

[31]A. Francis, J. K. Freericks, and A. F. Kemper, "Quantum computation of magnon spectra", Phys. Rev. B **101**, 014411 (2020).

[32]M. A. Nielsen and I. L. Chuang, *Quantum computation and quantum information* (Cambridge University Press, Cambridge, England, 2010).

[33]J. R. McClean, M. E. Kimchi-Schwartz, J. Carter, and W. A. de Jong, "Hybrid quantum-classical hierarchy for mitigation of decoherence and determination of excited states", Phys. Rev. A **95**, 042308 (2017).

[34]Cirq Developers, *Cirq*, version v0.14.1, Apr. 2022.

[35]T. E. O'Brien, B. Tarasinski, and L. DiCarlo, "Density-matrix simulation of small surface codes under current and projected experimental noise", npj Quantum Inf **3**, 39 (2017).

[36]W. Dür, G. Vidal, and J. I. Cirac, "Three qubits can be entangled in two inequivalent ways", Phys. Rev. A **62**, 062314 (2000).

[37]M. Kardar, *Statistical Physics of Fields*, 1st ed. (Cambridge University Press, June 2007).

[38]P. Jordan and E. Wigner, "Über das Paulische äquivalenzverbot", Z. Physik **47**, 631–651 (1928).

[39]S. Lloyd, "Universal Quantum Simulators", Science **273**, 1073–1078 (1996).

[40]I. M. Georgescu, S. Ashhab, and F. Nori, "Quantum simulation", Rev. Mod. Phys. **86**, 153–185 (2014).

[41]A. Peruzzo, J. McClean, P. Shadbolt, M.-H. Yung, X.-Q. Zhou, P. J. Love, A. Aspuru-Guzik, and J. L. O'Brien, "A variational eigenvalue solver on a photonic quantum processor", Nat. Commun. **5**, 4213 (2014).

[42]P. O'Malley, R. Babbush, I. Kivlichan, J. Romero, J. McClean, R. Barends, J. Kelly, P. Roushan, A. Tranter, N. Ding, B. Campbell, Y. Chen, Z. Chen, B. Chiaro, A. Dunsworth, A. Fowler, E. Jeffrey, E. Lucero, A. Megrant, J. Mutus, M. Neeley, C. Neill, C. Quintana, D. Sank, A. Vainsencher, J. Wenner, T. White, P. Coveney, P. Love, H. Neven, A. Aspuru-Guzik, and J. Martinis, "Scalable Quantum Simulation of Molecular Energies", Phys. Rev. X **6**, 031007 (2016).

[43]A. Kandala, A. Mezzacapo, K. Temme, M. Takita, M. Brink, J. M. Chow, and J. M. Gambetta, "Hardware-efficient variational quantum eigensolver for small molecules and quantum magnets", Nature **549**, 242–246 (2017).

[44]J. I. Colless, V. V. Ramasesh, D. Dahlen, M. S. Blok, M. E. Kimchi-Schwartz, J. R. McClean, J. Carter, W. A. de Jong, and I. Siddiqi, "Computation of Molecular Spectra on a Quantum Processor with an Error-Resilient Algorithm", Phys. Rev. X **8**, 011021 (2018).

[45]A. Kandala, K. Temme, A. D. Córcoles, A. Mezzacapo, J. M. Chow, and J. M. Gambetta, "Error mitigation extends the computational reach of a noisy quantum processor", Nature **567**, 491–495 (2019).

[46]H. Ma, M. Govoni, and G. Galli, "Quantum simulations of materials on near-term quantum computers", npj Computational Materials **6**, 85 (2020).

[47]F. Arute, K. Arya, R. Babbush, D. Bacon, J. C. Bardin, R. Barends, S. Boixo, M. Broughton, B. B. Buckley, D. A. Buell, B. Burkett, N. Bushnell, Y. Chen, Z. Chen, B. Chiaro, R. Collins, W. Courtney, S. Demura, A. Dunsworth, D. Eppens, E. Farhi, A. Fowler, B. Foxen, C. Gidney, M. Giustina, R. Graff, S. Habegger, M. P. Harrigan, A. Ho, S. Hong, T. Huang, W. J. Huggins, L. Ioffe, S. V. Isakov, E. Jeffrey, Z. Jiang, C. Jones, D. Kafri, K. Kechedzhi, J. Kelly, S. Kim, P. V. Klimov, A. Korotkov, F. Kostritsa, D. Landhuis, P. Laptev, M. Lindmark, E. Lucero, O. Martin, J. M. Martinis, J. R. McClean, M. McEwen, A. Megrant, X. Mi, M. Mohseni, W. Mruczkiewicz, J. Mutus, O. Naaman, M. Neeley, C. Neill, H. Neven, M. Y. Niu, T. E. O'Brien, E. Ostby, A. Petukhov, H. Putterman, C. Quintana, P. Roushan, N. C. Rubin, D. Sank, K. J. Satzinger, V. Smelyanskiy, D. Strain, K. J. Sung, M. Szalay, T. Y. Takeshita, A. Vainsencher, T. White, N. Wiebe, Z. J. Yao, P. Yeh, and A. Zalcman, "Hartree-Fock on a superconducting qubit quantum computer", Science **369**, 1084–1089 (2020).

[48]R. Islam, C. Senko, W. C. Campbell, S. Korenblit, J. Smith, A. Lee, E. E. Edwards, C.-C. J. Wang, J. K. Freericks, and C. Monroe, "Emergence and Frustration of Magnetism with Variable-Range Interactions in a Quantum Simulator", Science **340**, 583–587 (2013).

[49]J. Zhang, G. Pagano, P. W. Hess, A. Kyprianidis, P. Becker, H. Kaplan, A. V. Gorshkov, Z.-X. Gong, and C. Monroe, "Observation of a many-body dynamical phase transition with a 53-qubit quantum simulator", Nature **551**, 601–604 (2017).

[50]A. Smith, M. S. Kim, F. Pollmann, and J. Knolle, "Simulating quantum many-body dynamics on a current digital quantum computer", npj Quantum Inf. **5**, 106 (2019).

[51]B. Bauer, S. Bravyi, M. Motta, and G. K.-L. Chan, "Quantum Algorithms for Quantum Chemistry and Quantum Materials Science", Chem. Rev. **120**, 12685–12717 (2020).

[52]B. M. Terhal and D. P. DiVincenzo, "Problem of equilibration and the computation of correlation functions on a quantum computer", Phys. Rev. A **61**, 022301 (2000).

[53]D. Poulin and P. Wocjan, "Sampling from the Thermal Quantum Gibbs State and Evaluating Partition Functions with a Quantum Computer", Phys. Rev. Lett. **103**, 220502 (2009).

[54]A. Riera, C. Gogolin, and J. Eisert, "Thermalization in nature and on a quantum computer", Phys. Rev. Lett. **108**, 080402 (2012).

[55]K. Temme, T. J. Osborne, K. G. Vollbrecht, D. Poulin, and F. Verstraete, "Quantum Metropolis sampling", Nature **471**, 87 (2011).

[56]M.-H. Yung and A. Aspuru-Guzik, "A quantum–quantum Metropolis algorithm", Proc. Natl. Acad. Sci. **109**, 754–759 (2012).

[57]J. Martyn and B. Swingle, "Product spectrum ansatz and the simplicity of thermal states", Phys. Rev. A **100**, 032107 (2019).

[58]J. Wu and T. H. Hsieh, "Variational Thermal Quantum Simulation via Thermofield Double States", Phys. Rev. Lett. **123**, 220502 (2019).

[59]D. Zhu, S. Johri, N. M. Linke, K. A. Landsman, C. Huerta Alderete, N. H. Nguyen, A. Y. Matsuura, T. H. Hsieh, and C. Monroe, "Generation of thermofield double states and critical ground states with a quantum computer", Proc. Natl. Acad. Sci. **117**, 25402–25406 (2020).

[60]J.-G. Liu, L. Mao, P. Zhang, and L. Wang, *Solving Quantum Statistical Mechanics with Variational Autoregressive Networks and Quantum Circuits*.

[61]G. Verdon, J. Marks, S. Nanda, S. Leichenauer, and J. Hidary, *Quantum Hamiltonian-Based Models and the Variational Quantum Thermalizer Algorithm*.

[62]A. N. Chowdhury, G. H. Low, and N. Wiebe, *A Variational Quantum Algorithm for Preparing Quantum Gibbs States*.

[63]C. Zoufal, A. Lucchi, and S. Woerner, *Variational Quantum Boltzmann Machines*, 2020.

[64]C. S. Wang, J. C. Curtis, B. J. Lester, Y. Zhang, Y. Y. Gao, J. Freeze, V. S. Batista, P. H. Vaccaro, I. L. Chuang, L. Frunzio, L. Jiang, S. Girvin, and R. J. Schoelkopf, "Efficient Multiphoton Sampling of Molecular Vibronic Spectra on a Superconducting Bosonic Processor", Phys. Rev. X **10**, 021060 (2020).

[65]J. Cohn, F. Yang, K. Najafi, B. Jones, and J. K. Freericks, "Minimal effective Gibbs ansatz: A simple protocol for extracting an accurate thermal representation for quantum simulation", Phys. Rev. A **102**, 022622 (2020).

[66]S. McArdle, T. Jones, S. Endo, Y. Li, S. C. Benjamin, and X. Yuan, "Variational ansatz-based quantum simulation of imaginary time evolution", npj Quantum Inf. **5**, 75 (2019).

[67]X. Yuan, S. Endo, Q. Zhao, Y. Li, and S. C. Benjamin, "Theory of variational quantum simulation", Quantum **3**, 191 (2019).

[68]M. J. S. Beach, R. G. Melko, T. Grover, and T. H. Hsieh, "Making trotters sprint: A variational imaginary time ansatz for quantum many-body systems", Phys. Rev. B **100**, 094434 (2019).

[69]S. R. White, "Minimally Entangled Typical Quantum States at Finite Temperature", Phys. Rev. Lett. **102**, 190601 (2009).

[70]E. M. Stoudenmire and S. R. White, "Minimally entangled typical thermal state algorithms", New J. Phys. **12**, 055026 (2010).

[71]K. Yeter-Aydeniz, R. C. Pooser, and G. Siopsis, "Practical quantum computation of chemical and nuclear energy levels using quantum imaginary time evolution and Lanczos algorithms", npj Quantum Inf. **6**, 63 (2020).

[72]H. Nishi, T. Kosugi, and Y.-i. Matsushita, *Implementation of quantum imaginary-time evolution method on nisq devices: nonlocal approximation*.

[73]N. Gomes, F. Zhang, N. F. Berthusen, C.-Z. Wang, K.-M. Ho, P. P. Orth, and Y. Yao, *Efficient step-merged quantum imaginary time evolution algorithm for quantum chemistry*.

[74]K. Yeter-Aydeniz, G. Siopsis, and R. C. Pooser, "Scattering in the ising model with the quantum lanczos algorithm*", New Journal of Physics **23**, 043033 (2021).

[75]G. Vidal, "Efficient Simulation of One-Dimensional Quantum Many-Body Systems", Phys. Rev. Lett. **93**, 040502 (2004).

[76]H. F. Trotter, "On the product of semi-groups of operators", Proc. Am. Math. Soc. **10**, 545–551 (1959).

[77]S. Bravyi, J. M. Gambetta, A. Mezzacapo, and K. Temme, *Tapering off qubits to simulate fermionic hamiltonians*.

[78]N. Khaneja, R. Brockett, and S. J. Glaser, "Time optimal control in spin systems", Phys. Rev. A **63**, 032308 (2001).

[79]B. Kraus and J. I. Cirac, "Optimal creation of entanglement using a two-qubit gate", Phys. Rev. A **63**, 062309 (2001).

[80]F. Vatan and C. Williams, "Optimal quantum circuits for general two-qubit gates", Phys. Rev. A **69**, 032315 (2004).

[81]G. Vidal and C. M. Dawson, "Universal quantum circuit for two-qubit transformations with three controlled-NOT gates", Phys. Rev. A **69**, 010301 (2004).

[82]S. Khatri, R. LaRose, A. Poremba, L. Cincio, A. T. Sornborger, and P. J. Coles, "Quantum-assisted quantum compiling", Quantum **3**, 140 (2019).

[83]T. Jones and S. C. Benjamin, *Quantum compilation and circuit optimisation via energy dissipation*.

[84]K. Heya, Y. Suzuki, Y. Nakamura, and K. Fujii, *Variational Quantum Gate Optimization*.

[85]J. Gray, "Quimb: A python package for quantum information and many-body calculations", J. Open Source Softw. **3**, 819 (2018).

[86]K. Temme, S. Bravyi, and J. M. Gambetta, "Error mitigation for short-depth quantum circuits", Phys. Rev. Lett. **119**, 180509 (2017).

[87]X. Bonet-Monroig, R. Sagastizabal, M. Singh, and T. E. O'Brien, "Low-cost error mitigation by symmetry verification", Phys. Rev. A **98**, 062339 (2018).

[88]S. McArdle, X. Yuan, and S. Benjamin, "Error-Mitigated Digital Quantum Simulation", Phys. Rev. Lett. **122**, 180501 (2019).

[89]P. Gokhale, O. Angiuli, Y. Ding, K. Gui, T. Tomesh, M. Suchara, M. Martonosi, and F. T. Chong, *Minimizing state preparations in variational quantum eigensolver by partitioning into commuting families*.

[90]O. Crawford, B. van Straaten, D. Wang, T. Parks, E. Campbell, and S. Brierley, *Efficient quantum measurement of pauli operators in the presence of finite sampling error*.

[91]T.-C. Yen, V. Verteletskyi, and A. F. Izmaylov, "Measuring All Compatible Operators in One Series of Single-Qubit Measurements Using Unitary Transformations", J. Chem. Theory Comput. **16**, 2400–2409 (2020).

[92]I. Hamamura and T. Imamichi, "Efficient evaluation of quantum observables using entangled measurements", npj Quantum Inf. **6**, 56 (2020).

[93]A. Asfaw, L. Bello, Y. Ben-Haim, S. Bravyi, N. Bronn, L. Capelluto, A. C. Vazquez, J. Ceroni, R. Chen, A. Frisch, J. Gambetta, S. Garion, L. Gil, S. D. L. P. Gonzalez, F. Harkins, T. Imamichi, D. McKay, A. Mezzacapo, Z. Minev, R. Movassagh, G. Nannicni, P. Nation, A. Phan, M. Pistoia, A. Rattew, J. Schaefer, J. Shabani, J. Smolin, K. Temme, M. Tod, S. Wood, and J. Wootton., *Learn Quantum Computation using Qiskit*, http://community.qiskit.org/textbook.

[94]J. Gambetta and D. McClure, *Hitting a Quantum Volume Chord: IBM Quantum adds six new systems with Quantum Volume 32*, https://www.ibm.com/blogs/research/2020/07/qv32-performance/.

[95]G. Aleksandrowicz, T. Alexander, P. Barkoutsos, L. Bello, Y. Ben-Haim, D. Bucher, F. J. Cabrera-Hernández, J. Carballo-Franquis, A. Chen, C.-F. Chen, J. M. Chow, A. D. Córcoles-Gonzales, A. J. Cross, A. Cross, J. Cruz-Benito, C. Culver, S. D. L. P. González, E. D. L. Torre, D. Ding, E. Dumitrescu, I. Duran, P. Eendebak, M. Everitt, I. F. Sertage, A. Frisch, A. Fuhrer, J. Gambetta, B. G. Gago, J. Gomez-Mosquera, D. Greenberg, I. Hamamura, V. Havlicek, J. Hellmers, Ł. Herok, H. Horii, S. Hu, T. Imamichi, T. Itoko, A. Javadi-Abhari, N. Kanazawa, A. Karazeev, K. Krsulich, P. Liu, Y. Luh, Y. Maeng, M. Marques, F. J. Martín-Fernández, D. T. McClure, D. McKay, S. Meesala, A. Mezzacapo, N. Moll, D. M. Rodríguez, G. Nannicini, P. Nation, P. Ollitrault, L. J. O'Riordan, H. Paik, J. Pérez, A. Phan, M. Pistoia, V. Prutyanov, M. Reuter, J. Rice, A. R. Davila, R. H. P. Rudy, M. Ryu, N. Sathaye, C. Schnabel, E. Schoute, K. Setia, Y. Shi, A. Silva, Y. Siraichi, S. Sivarajah, J. A. Smolin, M. Soeken, H. Takahashi, I. Tavernelli, C. Taylor, P. Taylour, K. Trabing, M. Treinish, W. Turner, D. Vogt-Lee, C. Vuillot, J. A. Wildstrom, J. Wilson, E. Winston, C. Wood, S. Wood, S. Wörner, I. Y. Akhalwaya, and C. Zoufal, "Qiskit: An Open-source Framework for Quantum Computing", 10.5281/ZENODO.2562111 (2019).

[96]P. Jurcevic, A. Javadi-Abhari, L. S. Bishop, I. Lauer, D. F. Bogorin, M. Brink, L. Capelluto, O. Günlük, T. Itoko, N. Kanazawa, A. Kandala, G. A. Keefe, K. Krsulich, W. Landers, E. P. Lewandowski, D. T. McClure, G. Nannicini, A. Narasgond, H. M. Nayfeh, E. Pritchett, M. B. Rothwell, S. Srinivasan, N. Sundaresan, C. Wang, K. X. Wei, C. J. Wood, J.-B. Yau, E. J. Zhang, O. E. Dial, J. M. Chow, and J. M. Gambetta, "Demonstration of quantum volume 64 on a superconducting quantum computing system", Quantum Sci. Technol. **6**, 025020 (2021).

[97]R. Barends, L. Lamata, J. Kelly, L. García-Álvarez, A. G. Fowler, A. Megrant, E. Jeffrey, T. C. White, D. Sank, J. Y. Mutus, B. Campbell, Y. Chen, Z. Chen, B. Chiaro, A. Dunsworth, I.-C. Hoi, C. Neill, P. J. J. O'Malley, C. Quintana, P. Roushan, A. Vainsencher, J. Wenner, E. Solano, and J. M. Martinis, "Digital quantum simulation of fermionic models with a superconducting circuit", Nat. Commun. **6**, 7654 (2015).

[98]R. N. Tazhigulov, S.-N. Sun, R. Haghshenas, H. Zhai, A. T. Tan, N. C. Rubin, R. Babbush, A. J. Minnich, and G. K.-L. Chan, "Simulating Models of Challenging Correlated Molecules and Materials on the Sycamore Quantum Processor", PRX Quantum **3**, 040318 (2022),

[99]A. Francis, D. Zhu, C. Huerta Alderete, S. Johri, X. Xiao, J. K. Freericks, C. Monroe, N. M. Linke, and A. F. Kemper, "Many-body thermodynamics on quantum computers via partition function zeros", Sci. Adv. **7**, eabf2447 (2021).

[100]K. J. Satzinger, Y.-J. Liu, A. Smith, C. Knapp, M. Newman, C. Jones, Z. Chen, C. Quintana, X. Mi, A. Dunsworth, C. Gidney, I. Aleiner, F. Arute, K. Arya, J. Atalaya, R. Babbush, J. C. Bardin, R. Barends, J. Basso, A. Bengtsson, A. Bilmes, M. Broughton, B. B. Buckley, D. A. Buell, B. Burkett, N. Bushnell, B. Chiaro, R. Collins, W. Courtney, S. Demura, A. R. Derk, D. Eppens, C. Erickson,

L. Faoro, E. Farhi, A. G. Fowler, B. Foxen, M. Giustina, A. Greene, J. A. Gross, M. P. Harrigan, S. D. Harrington, J. Hilton, S. Hong, T. Huang, W. J. Huggins, L. B. Ioffe, S. V. Isakov, E. Jeffrey, Z. Jiang, D. Kafri, K. Kechedzhi, T. Khattar, S. Kim, P. V. Klimov, A. N. Korotkov, F. Kostritsa, D. Landhuis, P. Laptev, A. Locharla, E. Lucero, O. Martin, J. R. McClean, M. McEwen, K. C. Miao, M. Mohseni, S. Montazeri, W. Mruczkiewicz, J. Mutus, O. Naaman, M. Neeley, C. Neill, M. Y. Niu, T. E. O'Brien, A. Opremcak, B. Pató, A. Petukhov, N. C. Rubin, D. Sank, V. Shvarts, D. Strain, M. Szalay, B. Villalonga, T. C. White, Z. Yao, P. Yeh, J. Yoo, A. Zalcman, H. Neven, S. Boixo, A. Megrant, Y. Chen, J. Kelly, V. Smelyanskiy, A. Kitaev, M. Knap, F. Pollmann, and P. Roushan, "Realizing topologically ordered states on a quantum processor", Science **374**, 1237–1241 (2021).

[101] A. T. K. Tan, S.-N. Sun, R. N. Tazhigulov, G. K.-L. Chan, and A. J. Minnich, "Realizing symmetry-protected topological phases in a spin-1/2 chain with next-nearest-neighbor hopping on superconducting qubits", Phys. Rev. A **107**, 032614 (2023),

[102] K. Xu, J.-J. Chen, Y. Zeng, Y.-R. Zhang, C. Song, W. Liu, Q. Guo, P. Zhang, D. Xu, H. Deng, K. Huang, H. Wang, X. Zhu, D. Zheng, and H. Fan, "Emulating many-body localization with a superconducting quantum processor", Phys. Rev. Lett. **120**, 050507 (2018).

[103] X. Mi, M. Ippoliti, C. Quintana, A. Greene, Z. Chen, J. Gross, F. Arute, K. Arya, J. Atalaya, R. Babbush, J. C. Bardin, J. Basso, A. Bengtsson, A. Bilmes, A. Bourassa, L. Brill, M. Broughton, B. B. Buckley, D. A. Buell, B. Burkett, N. Bushnell, B. Chiaro, R. Collins, W. Courtney, D. Debroy, S. Demura, A. R. Derk, A. Dunsworth, D. Eppens, C. Erickson, E. Farhi, A. G. Fowler, B. Foxen, C. Gidney, M. Giustina, M. P. Harrigan, S. D. Harrington, J. Hilton, A. Ho, S. Hong, T. Huang, A. Huff, W. J. Huggins, L. B. Ioffe, S. V. Isakov, J. Iveland, E. Jeffrey, Z. Jiang, C. Jones, D. Kafri, T. Khattar, S. Kim, A. Kitaev, P. V. Klimov, A. N. Korotkov, F. Kostritsa, D. Landhuis, P. Laptev, J. Lee, K. Lee, A. Locharla, E. Lucero, O. Martin, J. R. McClean, T. McCourt, M. McEwen, K. C. Miao, M. Mohseni, S. Montazeri, W. Mruczkiewicz, O. Naaman, M. Neeley, C. Neill, M. Newman, M. Y. Niu, T. E. O'Brien, A. Opremcak, E. Ostby, B. Pato, A. Petukhov, N. C. Rubin, D. Sank, K. J. Satzinger, V. Shvarts, Y. Su, D. Strain, M. Szalay, M. D. Trevithick, B. Villalonga, T. White, Z. J. Yao, P. Yeh, J. Yoo, A. Zalcman, H. Neven, S. Boixo, V. Smelyanskiy, A. Megrant, J. Kelly, Y. Chen, S. L. Sondhi, R. Moessner, K. Kechedzhi, V. Khemani, and P. Roushan, "Time-crystalline eigenstate order on a quantum processor", Nature **601**, 531–536 (2022).

[104] D. Niu, R. Haghshenas, Y. Zhang, M. Foss-Feig, G. K.-L. Chan, and A. C. Potter, "Holographic Simulation of Correlated Electrons on a Trapped-Ion Quantum Processor", PRX Quantum **3**, 030317 (2022).

[105] J. Gibbs, K. Gili, Z. Holmes, B. Commeau, A. Arrasmith, L. Cincio, P. J. Coles, and A. Sornborger, "Long-time simulations for fixed input states on quantum hardware", npj Quantum Inf. **8**, 135 (2022).

[106]Y. Wu, W.-S. Bao, S. Cao, F. Chen, M.-C. Chen, X. Chen, T.-H. Chung, H. Deng, Y. Du, D. Fan, M. Gong, C. Guo, C. Guo, S. Guo, L. Han, L. Hong, H.-L. Huang, Y.-H. Huo, L. Li, N. Li, S. Li, Y. Li, F. Liang, C. Lin, J. Lin, H. Qian, D. Qiao, H. Rong, H. Su, L. Sun, L. Wang, S. Wang, D. Wu, Y. Xu, K. Yan, W. Yang, Y. Yang, Y. Ye, J. Yin, C. Ying, J. Yu, C. Zha, C. Zhang, H. Zhang, K. Zhang, Y. Zhang, H. Zhao, Y. Zhao, L. Zhou, Q. Zhu, C.-Y. Lu, C.-Z. Peng, X. Zhu, and J.-W. Pan, "Strong Quantum Computational Advantage Using a Superconducting Quantum Processor", Phys. Rev. Lett. **127**, 180501 (2021).

[107]A. J. Daley, I. Bloch, C. Kokail, S. Flannigan, N. Pearson, M. Troyer, and P. Zoller, "Practical quantum advantage in quantum simulation", Nature **607**, 667–676 (2022).

[108]W. von Nissen, J. Schirmer, and L. S. Cederbaum, "Computational Methods for the One-Particle Green's Function", Comput. Phys. Rep. **1**, 57–125 (1984).

[109]C. A. Ullrich, *Time-Dependent Density-Functional Theory : Concepts and Applications*, Oxford graduate texts (Oxford University Press, 2019).

[110]A. Damascelli, Z. Hussain, and Z.-X. Shen, "Angle-resolved photoemission studies of the cuprate superconductors", Rev. Mod. Phys. **75**, 473–541 (2003).

[111]S.-N. Sun, M. Motta, R. N. Tazhigulov, A. T. Tan, G. K.-L. Chan, and A. J. Minnich, "Quantum Computation of Finite-Temperature Static and Dynamical Properties of Spin Systems Using Quantum Imaginary Time Evolution", PRX Quantum **2**, 010317 (2021),

[112]R. M. Parrish, E. G. Hohenstein, P. L. McMahon, and T. J. Martínez, "Quantum Computation of Electronic Transitions Using a Variational Quantum Eigensolver", Phys. Rev. Lett. **122**, 230401 (2019).

[113]T. Jones, S. Endo, S. McArdle, X. Yuan, and S. C. Benjamin, "Variational quantum algorithms for discovering Hamiltonian spectra", Phys. Rev. A **99**, 062304 (2019).

[114]S. Endo, I. Kurata, and Y. O. Nakagawa, "Calculation of the green's function on near-term quantum computers", Phys. Rev. Res. **2**, 033281 (2020).

[115]H. Chen, M. Nusspickel, J. Tilly, and G. H. Booth, "Variational quantum eigensolver for dynamic correlation functions", Phys. Rev. A **104**, 032405 (2021).

[116]A. Kumar, A. Asthana, V. Abraham, T. D. Crawford, N. J. Mayhall, Y. Zhang, L. Cincio, S. Tretiak, and P. A. Dub, *Quantum simulation of molecular response properties*.

[117]F. Jamet, A. Agarwal, and I. Rungger, *Quantum subspace expansion algorithm for Green's functions*.

[118]X. Cai, W.-H. Fang, H. Fan, and Z. Li, "Quantum computation of molecular response properties", Phys. Rev. Res. **2**, 033324 (2020).

[119]K. Huang, X. Cai, H. Li, Z.-Y. Ge, R. Hou, H. Li, T. Liu, Y. Shi, C. Chen, D. Zheng, K. Xu, Z.-B. Liu, Z. Li, H. Fan, and W.-H. Fang, "Variational Quantum Computation of Molecular Linear Response Properties on a Superconducting Quantum Processor", J. Phys. Chem. Lett. **13**, 9114–9121 (2022).

[120]J. J. Wallman and J. Emerson, "Noise tailoring for scalable quantum computation via randomized compiling", Phys. Rev. A **94**, 052325 (2016).

[121]A. Hashim, R. K. Naik, A. Morvan, J.-L. Ville, B. Mitchell, J. M. Kreikebaum, M. Davis, E. Smith, C. Iancu, K. P. O'Brien, I. Hincks, J. J. Wallman, J. Emerson, and I. Siddiqi, "Randomized Compiling for Scalable Quantum Computing on a Noisy Superconducting Quantum Processor", Phys. Rev. X **11**, 041039 (2021).

[122]R. McWeeny, "Some Recent Advances in Density Matrix Theory", Rev. Mod. Phys. **32**, 335–369 (1960).

[123]Q. Sun, X. Zhang, S. Banerjee, P. Bao, M. Barbry, N. S. Blunt, N. A. Bogdanov, G. H. Booth, J. Chen, Z.-H. Cui, J. J. Eriksen, Y. Gao, S. Guo, J. Hermann, M. R. Hermes, K. Koh, P. Koval, S. Lehtola, Z. Li, J. Liu, N. Mardirossian, J. D. McClain, M. Motta, B. Mussard, H. Q. Pham, A. Pulkin, W. Purwanto, P. J. Robinson, E. Ronca, E. R. Sayfutyarova, M. Scheurer, H. F. Schurkus, J. E. T. Smith, C. Sun, S.-N. Sun, S. Upadhyay, L. K. Wagner, X. Wang, A. White, J. D. Whitfield, M. J. Williamson, S. Wouters, J. Yang, J. M. Yu, T. Zhu, T. C. Berkelbach, S. Sharma, A. Y. Sokolov, and G. K.-L. Chan, "Recent developments in the PySCF program package", J. Chem. Phys. **153**, 024109 (2020).

[124]J. R. McClean, N. C. Rubin, K. J. Sung, I. D. Kivlichan, X. Bonet-Monroig, Y. Cao, C. Dai, E. S. Fried, C. Gidney, B. Gimby, P. Gokhale, T. Häner, T. Hardikar, V. Havlíček, O. Higgott, C. Huang, J. Izaac, Z. Jiang, X. Liu, S. McArdle, M. Neeley, T. O'Brien, B. O'Gorman, I. Ozfidan, M. D. Radin, J. Romero, N. P. D. Sawaya, B. Senjean, K. Setia, S. Sim, D. S. Steiger, M. Steudtner, Q. Sun, W. Sun, D. Wang, F. Zhang, and R. Babbush, "OpenFermion: the electronic structure package for quantum computers", Quantum Sci. Technol. **5**, 034014 (2020).

[125]A. Hashim, R. Rines, V. Omole, R. K. Naik, J. M. Kreikebaum, D. I. Santiago, F. T. Chong, I. Siddiqi, and P. Gokhale, "Optimized SWAP networks with equivalent circuit averaging for QAOA", Phys. Rev. Res. **4**, 033028 (2022).

[126]M. S. Blok, V. V. Ramasesh, T. Schuster, K. O'Brien, J. M. Kreikebaum, D. Dahlen, A. Morvan, B. Yoshida, N. Y. Yao, and I. Siddiqi, "Quantum information scrambling on a superconducting qutrit processor", Phys. Rev. X **11**, 021010 (2021).

[127]B. K. Mitchell, R. K. Naik, A. Morvan, A. Hashim, J. M. Kreikebaum, B. Marinelli, W. Lavrijsen, K. Nowrouzi, D. I. Santiago, and I. Siddiqi, "Hardware-efficient microwave-activated tunable coupling between superconducting qubits", Phys. Rev. Lett. **127**, 200502 (2021).

[128]S. J. Beale, K. Boone, A. Carignan-Dugas, A. Chytros, D. Dahlen, H. Dawkins, J. Emerson, S. Ferracin, V. Frey, I. Hincks, D. Hufnagel, P. Iyer, A. Jain, J. Kolbush, E. Ospadov, J. L. Pino, H. Qassim, J. Saunders, J. Skanes-Norman, A. Stasiuk, J. J. Wallman, A. Winick, and E. Wright, *True-Q*, version 2, June 2020.

[129]A. Erhard, J. J. Wallman, L. Postler, M. Meth, R. Stricker, E. A. Martinez, P. Schindler, T. Monz, J. Emerson, and R. Blatt, "Characterizing large-scale quantum computers via cycle benchmarking", Nature Comms. **10**, 5347 (2019).

[130]J. M. Gambetta, A. D. Córcoles, S. T. Merkel, B. R. Johnson, J. A. Smolin, J. M. Chow, C. A. Ryan, C. Rigetti, S. Poletto, T. A. Ohki, M. B. Ketchen, and M. Steffen, "Characterization of addressability by simultaneous randomized benchmarking", Phys. Rev. Lett. **109**, 240504 (2012).

[131]K. Yeter-Aydeniz, B. T. Gard, J. Jakowski, S. Majumder, G. S. Barron, G. Siopsis, T. S. Humble, and R. C. Pooser, "Benchmarking Quantum Chemistry Computations with Variational, Imaginary Time Evolution, and Krylov Space Solver Algorithms", Adv. Quantum Technol. **4**, 2100012 (2021).

[132]M. Christandl and R. Renner, "Reliable Quantum State Tomography", Phys. Rev. Lett. **109**, 120403 (2012).

[133]E. Younis, C. C. Iancu, W. Lavrijsen, M. Davis, and E. Smith, *Berkeley quantum synthesis toolkit (bqskit) v1*, Apr. 2021.

[134]V. Shende and I. Markov, "On the CNOT-cost of TOFFOLI gates", Quantum Inf. Comput. **9**, 461–486 (2009).

[135]S. Goedecker, "Linear scaling electronic structure methods", Rev. Mod. Phys. **71**, 1085–1123 (1999).

[136]J.-L. Ville, A. Morvan, A. Hashim, R. K. Naik, M. Lu, B. Mitchell, J.-M. Kreikebaum, K. P. O'Brien, J. J. Wallman, I. Hincks, J. Emerson, E. Smith, E. Younis, C. Iancu, D. I. Santiago, and I. Siddiqi, "Leveraging randomized compiling for the quantum imaginary-time-evolution algorithm", Phys. Rev. Res. **4**, 033140 (2022).

[137]A. M. Childs, R. Kothari, and R. D. Somma, "Quantum algorithm for systems of linear equations with exponentially improved dependence on precision", SIAM J. Comput. **46**, 1920–1950 (2017).

[138]J. Wen, C. Zheng, X. Kong, S. Wei, T. Xin, and G. Long, "Experimental demonstration of a digital quantum simulation of a general PT -symmetric system", Phys. Rev. A **99**, 062122 (2019).

[139]A. N. Chowdhury and R. D. Somma, "Quantum algorithms for Gibbs sampling and hitting-time estimation", Quantum Inf. Comput. **17**, 41–64 (2017).

[140]P. W. Shor, "Polynomial-Time Algorithms for Prime Factorization and Discrete Logarithms on a Quantum Computer", SIAM J. Comput. **26**, 1484 (1997).

[141]L. K. Grover, "Quantum Mechanics Helps in Searching for a Needle in a Haystack", Phys. Rev. Lett. **79**, 325–328 (1997).

[142]M. Mariantoni, H. Wang, T. Yamamoto, M. Neeley, R. C. Bialczak, Y. Chen, M. Lenander, E. Lucero, A. D. O'Connell, D. Sank, M. Weides, J. Wenner, Y. Yin, J. Zhao, A. N. Korotkov, A. N. Cleland, and J. M. Martinis, "Implementing the Quantum von Neumann Architecture with Superconducting Circuits", Science **334**, 61–65 (2011).

[143]A. Fedorov, L. Steffen, M. Baur, M. P. da Silva, and A. Wallraff, "Implementation of a Toffoli gate with superconducting circuits", Nature **481**, 170–172 (2012).

[144]M. D. Reed, L. DiCarlo, S. E. Nigg, L. Sun, L. Frunzio, S. M. Girvin, and R. J. Schoelkopf, "Realization of three-qubit quantum error correction with superconducting circuits", Nature **482**, 382–385 (2012).

[145]A. D. Hill, M. J. Hodson, N. Didier, and M. J. Reagor, *Realization of arbitrary doubly-controlled quantum phase gates*.

[146]A. Galda, M. Cubeddu, N. Kanazawa, P. Narang, and N. Earnest-Noble, *Implementing a Ternary Decomposition of the Toffoli Gate on Fixed-Frequency Transmon Qutrits*.

[147]C. W. Warren, J. Fernández-Pendás, S. Ahmed, T. Abad, A. Bengtsson, J. Biznárová, K. Debnath, X. Gu, C. Križan, A. Osman, A. Fadavi Roudsari, P. Delsing, G. Johansson, A. Frisk Kockum, G. Tancredi, and J. Bylander, "Extensive characterization and implementation of a family of three-qubit gates at the coherence limit", npj Quantum Inf. **9**, 44 (2023).

[148]J. Chu, X. He, Y. Zhou, J. Yuan, L. Zhang, Q. Guo, Y. Hai, Z. Han, C.-K. Hu, W. Huang, H. Jia, D. Jiao, S. Li, Y. Liu, Z. Ni, L. Nie, X. Pan, J. Qiu, W. Wei, W. Nuerbolati, Z. Yang, J. Zhang, Z. Zhang, W. Zou, Y. Chen, X. Deng, X. Deng, L. Hu, J. Li, S. Liu, Y. Lu, J. Niu, D. Tan, Y. Xu, T. Yan, Y. Zhong, F. Yan, X. Sun, and D. Yu, "Scalable algorithm simplification using quantum AND logic", Nat. Phys. **19**, 126–131 (2023).

[149]R. Raussendorf, D. E. Browne, and H. J. Briegel, "Measurement-based quantum computation on cluster states", Phys. Rev. A **68**, 022312 (2003).

[150]D. W. Leung, "Quantum computation by measurements", Int. J. of Quantum Inform. **02**, 33–43 (2004).

[151]D. Gross and J. Eisert, "Novel schemes for measurement-based quantum computation", Phys. Rev. Lett. **98**, 220503 (2007).

[152]H. J. Briegel, D. E. Browne, W. Dür, R. Raussendorf, and M. Van Den Nest, "Measurement-based quantum computation", Nature Phys **5**, 19–26 (2009).

[153]H. J. Briegel and R. Raussendorf, "Persistent Entanglement in Arrays of Interacting Particles", Phys. Rev. Lett. **86**, 910–913 (2001).

[154]R. Raussendorf, S. Bravyi, and J. Harrington, "Long-range quantum entanglement in noisy cluster states", Phys. Rev. A **71**, 062313 (2005).

[155]A. Bolt, G. Duclos-Cianci, D. Poulin, and T. M. Stace, "Foliated Quantum Error-Correcting Codes", Phys. Rev. Lett. **117**, 070501 (2016).

[156]R. Verresen, N. Tantivasadakarn, and A. Vishwanath, *Efficiently preparing Schr\"odinger's cat, fractons and non-Abelian topological order in quantum devices*, Jan. 2022.

[157]N. Tantivasadakarn, A. Vishwanath, and R. Verresen, "Hierarchy of Topological Order From Finite-Depth Unitaries, Measurement, and Feedforward", PRX Quantum **4**, 020339 (2023).

[158]G. G. Guerreschi, J. Hogaboam, F. Baruffa, and N. P. D. Sawaya, "Intel Quantum Simulator: a cloud-ready high-performance simulator of quantum circuits", Quantum Sci. Technol. **5**, 034007 (2020).

[159]S. V. Isakov, D. Kafri, O. Martin, C. V. Heidweiller, W. Mruczkiewicz, M. P. Harrigan, N. C. Rubin, R. Thomson, M. Broughton, K. Kissell, E. Peters, E. Gustafson, A. C. Y. Li, H. Lamm, G. Perdue, A. K. Ho, D. Strain, and S. Boixo, *Simulations of quantum circuits with approximate noise using qsim and cirq*, 2021.

[160]C. Roberts, A. Milsted, M. Ganahl, A. Zalcman, B. Fontaine, Y. Zou, J. Hidary, G. Vidal, and S. Leichenauer, *TensorNetwork: A Library for Physics and Machine Learning*, arXiv:1905.01330 [cond-mat, physics:hep-th, physics:physics, stat], May 2019.

[161]D. I. Lyakh, T. Nguyen, D. Claudino, E. Dumitrescu, and A. J. McCaskey, "ExaTN: Scalable GPU-Accelerated High-Performance Processing of General Tensor Networks at Exascale", Front. Appl. Math. Stat. **8**, 838601 (2022).

[162]S.-X. Zhang, J. Allcock, Z.-Q. Wan, S. Liu, J. Sun, H. Yu, X.-H. Yang, J. Qiu, Z. Ye, Y.-Q. Chen, C.-K. Lee, Y.-C. Zheng, S.-K. Jian, H. Yao, C.-Y. Hsieh, and S. Zhang, "TensorCircuit: a Quantum Software Framework for the NISQ Era", Quantum **7**, 912 (2023).

[163]D. Steinkraus, I. Buck, and P. Simard, "Using GPUs for machine learning algorithms", in Eighth International Conference on Document Analysis and Recognition (ICDAR'05) (2005), 1115–1120 Vol. 2.

[164]H. Nishimori, "Internal Energy, Specific Heat and Correlation Function of the Bond-Random Ising Model", Progress of Theoretical Physics (1981).

[165]G.-Y. Zhu, N. Tantivasadakarn, A. Vishwanath, S. Trebst, and R. Verresen, "Nishimori's cat: stable long-range entanglement from finite-depth unitaries and weak measurements", Phys. Rev. Lett. **131**, arXiv:2208.11136 [cond-mat, physics:quant-ph], 200201 (2023).

[166]E. H. Chen, G.-Y. Zhu, R. Verresen, A. Seif, E. Bäumer, D. Layden, N. Tantivasadakarn, G. Zhu, S. Sheldon, A. Vishwanath, S. Trebst, and A. Kandala, *Realizing the Nishimori transition across the error threshold for constant-depth quantum circuits*, arXiv:2309.02863 [cond-mat, physics:quant-ph], Dec. 2023.

[167]E. Knill and R. Laflamme, "Theory of quantum error-correcting codes", Phys. Rev. A **55**, 900–911 (1997).

[168]A. G. Fowler, "Minimum weight perfect matching of fault-tolerant topological quantum error correction in average $O(1)$ parallel time", arXiv:1307.1740 [quant-ph], arXiv: 1307.1740 (2014).

[169]C. Wang, J. Harrington, and J. Preskill, "Confinement-Higgs transition in a disordered gauge theory and the accuracy threshold for quantum memory", Annals of Physics **303**, 31–58 (2003).

[170]C. R. Harris, K. J. Millman, S. J. Van Der Walt, R. Gommers, P. Virtanen, D. Cournapeau, E. Wieser, J. Taylor, S. Berg, N. J. Smith, R. Kern, M. Picus, S. Hoyer, M. H. Van Kerkwijk, M. Brett, A. Haldane, J. F. Del Río, M. Wiebe, P. Peterson, P. Gérard-Marchant, K. Sheppard, T. Reddy, W. Weckesser, H. Abbasi, C. Gohlke, and T. E. Oliphant, "Array programming with NumPy", Nature **585**, 357–362 (2020).

[171]R. Okuta, Y. Unno, D. Nishino, S. Hido, and C. Loomis, "Cupy: a numpy-compatible library for nvidia gpu calculations", in Ml systems workshop, conference on neural information processing systems (nips) (2017).

[172]O. Higgott, "PyMatching: a python package for decoding quantum codes with minimum-weight perfect matching", ACM Transactions on Quantum Computing **3**, 1–16 (2022).

Appendix A

PROOF OF PAULI STRING REDUCTION BY $\mathbb{Z}_2$ SYMMETRIES

In 5.3 we introduced a scheme to reduce Pauli strings in the QITE unitaries by $\mathbb{Z}_2$ symmetries. We mentioned that rather than impose $\mathbb{Z}_2$ symmetries when choosing the Pauli strings in the QITE unitries, the original QITE algorithm subsumes the preservation of $\mathbb{Z}_2$ symmetries. We now restate the proposition and present a proof that derives directly from the QITE linear systems in 5.5.

Proposition 13. Suppose QITE is applied to approximate the imaginary time propagator $e^{-\Delta\tau\hat{H}[l]}$ on the state $|\Psi\rangle$. If there exists a stabilizer $\mathcal{S}$ such that every element of $\mathcal{S}$ commutes with $\hat{H}[l]$ and $|\Psi\rangle \in V_{\mathcal{S}}$, then
(a) The action of $e^{-i\Delta\tau\hat{G}[l]}$ on $|\Psi\rangle$ with $\sigma_\mu \in \mathcal{P}_{\hat{H}[l]}$ is equivalent to the action with $\sigma_\mu \in \mathcal{P}_{\hat{H}[l]} \cap \mathcal{N}(\mathcal{S})/\mathcal{S}$,
(b) $e^{-i\Delta\tau\hat{G}[l]}|\Psi\rangle \in V_{\mathcal{S}}$.

Proof. Pick $\sigma_\mu \notin \mathcal{N}(\mathcal{S})$. Since $e^{-\Delta\tau\hat{H}[l]}$ commutes with elements of $\mathcal{S}$ and $|\Psi\rangle \in V_{\mathcal{S}}$, for any $s \in \mathcal{S}$ we have $\langle\Psi| e^{-\Delta\tau\hat{H}[l]}\sigma_\mu s|\Psi\rangle = -\langle\Psi| s\, e^{-\Delta\tau\hat{H}[l]}\sigma_\mu|\Psi\rangle$, which implies $\langle\Psi| e^{-\Delta\tau\hat{H}[l]}\sigma_\mu|\Psi\rangle = 0$. Hence

$$b[l]_\mu = \frac{\mathrm{Im}\langle\Psi|e^{-\Delta\tau\hat{H}[l]}\sigma_\mu|\Psi\rangle}{\Delta\tau c[l]^{1/2}} = 0. \tag{A.1}$$

Now fix the column index ν such that $\sigma_\nu \in \mathcal{N}(\mathcal{S})$, then for any $s \in \mathcal{S}$, $\langle\Psi|\sigma_\mu\sigma_\nu s|\Psi\rangle = -\langle\Psi| s\,\sigma_\mu\sigma_\nu|\Psi\rangle$, which implies $\langle\Psi|\sigma_\mu\sigma_\nu|\Psi\rangle = 0$. Hence

$$A_{\mu\nu} = \mathrm{Re}(\langle\Psi|\sigma_\mu\sigma_\nu|\Psi\rangle) = 0 \tag{A.2}$$

Since $\boldsymbol{A}$ is Hermitian and real, $A_{\nu\mu} = A^*_{\mu\nu} = A_{\mu\nu} = 0$. Thus the linear system has the block-diagonal form

$$\begin{pmatrix} \boldsymbol{A}[l]' & \boldsymbol{0} \\ \boldsymbol{0} & \boldsymbol{A}[l]'' \end{pmatrix} \begin{pmatrix} \boldsymbol{x}[l]' \\ \boldsymbol{x}[l]'' \end{pmatrix} = \begin{pmatrix} \boldsymbol{b}[l]' \\ \boldsymbol{0} \end{pmatrix}, \tag{A.3}$$

where the quantities with single primes are indexed by $\boldsymbol{\mu}$ such that $\sigma_\mu \in \mathcal{N}(\mathcal{S})$ and those with double primes are indexed by $\boldsymbol{\mu}$ such that $\sigma_\mu \notin \mathcal{N}(\mathcal{S})$. By setting $\boldsymbol{x}[l]''$ to $\boldsymbol{0}$, the linear system is reduced to $\boldsymbol{A}[l]'\boldsymbol{x}[l]' = \boldsymbol{b}[l]'$.

To show that the set of σ_μ can be reduced from $\mathcal{N}(\mathcal{S})$ to $\mathcal{N}(\mathcal{S})/\mathcal{S}$, suppose σ_μ and $\sigma_{\mu'}$ belong to the same coset in $\mathcal{N}(\mathcal{S})/\mathcal{S}$, then $\sigma_{\mu'} = \pm\sigma_\mu s$ for some $s \in \mathcal{S}$. In the QITE unitary $e^{-i\Delta\tau\hat{G}[l]} = \sum_{k=0}^{\infty}(-i\Delta\tau)^k(\sum_\mu x[l]_\mu\sigma_\mu)^k$, each term in the sum is a power of $-i\Delta\tau$ times a product of the form $\prod_\nu(x[l]_\nu\sigma_\nu)$. If a product term contains $x[l]_{\mu'}\sigma_{\mu'}$, the action of this term on $|\Psi\rangle$ is proportional to

$$\left(\prod_{\nu''} x[l]_{\nu''}\sigma_{\nu''}\right)(x[l]_{\mu'}\sigma_{\mu'})\left(\prod_{\nu'} x[l]_{\nu'}\sigma_{\nu'}\right)|\Psi\rangle \tag{A.4}$$

In the product over $\boldsymbol{\nu'}$, each $\sigma_{\nu'} \in \mathcal{N}(\mathcal{S})$, so $\prod_{\nu'}(x[l]_{\nu'}\sigma_{\nu'})\,|\Psi\rangle \in V_\mathcal{S}$. Then A.4 is equivalent to

$$\left(\prod_{\nu''} x[l]_{\nu''}\sigma_{\nu''}\right)(\pm x[l]_{\mu'}\sigma_\mu)\left(\prod_{\nu'} x[l]_{\nu'}\sigma_{\nu'}\right)|\Psi\rangle \tag{A.5}$$

Since this applies to every pair of Pauli strings in the same coset, $\hat{G}[l]$ can be written as

$$\hat{G}[l] = \sum_{\boldsymbol{\mu}} \widetilde{x[l]}_\mu\sigma_\mu, \tag{A.6}$$

where $\boldsymbol{\mu}$ is chosen such that $\sigma_\mu \in \mathcal{P}_{\hat{H}[l]} \cap \mathcal{N}(\mathcal{S})/\mathcal{S}$, $\widetilde{x[l]}_\mu = \sum_{\mu'}\eta_{\mu'}x[l]_{\mu'}$, $\eta_{\mu'} = \pm 1$ and $\boldsymbol{\mu'}$ is chosen such that $\sigma_{\mu'} \in \sigma_\mu\mathcal{S}$.

Since all Pauli strings on the exponent of $e^{-i\Delta\tau\hat{G}[l]}$ commute with elements of $\mathcal{S}$, $e^{-i\Delta\tau\hat{G}[l]}$ commutes with elements of $\mathcal{S}$ and hence $e^{-i\Delta\tau\hat{G}[l]}\,|\Psi\rangle \in V_\mathcal{S}$. □

Our Pauli string reduction scheme is related to the qubit encoding scheme that removes redundant qubits by exploiting $\mathbb{Z}_2$ symmetries reported in Ref. [77]. In the qubit encoding scheme, a Hamiltonian over some number of qubits is transformed to another Hamiltonian over a smaller number of qubits by a series of Clifford gates. Our Pauli string reduction scheme coincides with the qubit encoding scheme when the domain size D equals the total number of qubits N, in the sense that the reduced set of Pauli strings in our scheme exactly corresponds to all Pauli strings in the encoded Hamiltonian with redundant qubits removed in the qubit encoding scheme.

However, because the weight of a Pauli string can change during the Clifford transformation, the two schemes differ when $D < N$. On the one hand, some Pauli strings can decrease in weight after encoding. If we include all Pauli strings with domain size D in the encoded Hamiltonian, these Pauli strings might include those with domain size $D' > D$ in the original Hamiltonian, thus increasing the total number

of Pauli strings. On the other hand, some Pauli strings can increase in weight after encoding and result in an increased cost of the QITE algorithm. As an example, consider performing QITE on a Hamiltonian with periodic boundary condition and the $\mathbb{Z}_2$ symmetry $Z_0Z_1Z_2Z_3$. One of the $D = 2$ Pauli strings is X_0Y_3. In the qubit encoding scheme, the symmetry operator $Z_0Z_1Z_2Z_3$ is transformed to Z_3 so that qubit 3 can be eliminated, but the weight-two Pauli string X_0Y_3 is transformed to the higher-weight Pauli string $X_0X_1Y_2$, thus requiring a larger QITE domain and increasing the overall cost of the algorithm. Therefore, in the present work, we use $\mathbb{Z}_2$ symmetries to reduce the number of Pauli strings in the QITE unitaries rather than eliminate redundant qubits.

Appendix B

ERROR BARS IN TRACE EVALUATION

We describe calculation of error bars of finite-temperature observables in full and stochastic trace evaluation. Here we use $E(Q)$ and $\mathrm{Var}(Q)$ to denote the mean and variance of a quantity Q. The error in Q is the square root of its variance.

A finite-temperature observable $\langle \hat{O} \rangle_\beta \equiv O$ has the expression $O = \sum_i P_i O_i / \sum_i P_i$, where $P_i = || \, |\Psi_i(\beta/2)\rangle \, ||^2$ is the (unnormalized) probability and $O_i = \langle \Psi_i(\beta/2) | \hat{O} | \Psi_i(\beta/2) \rangle$ is the expectation value of the observable after imaginary time evolution on the ith basis state $|\Psi_i\rangle$. On quantum computers, each probability P_i is built up from the energy expectation value at each imaginary time step:

$$P_i = \prod_{k=0}^{n_{\beta/2}-1} e^{-2\Delta\tau E_{i,k}}, \tag{B.1}$$

where $E_{i,k} = \langle \Phi_i(k\Delta\tau/2) | \hat{H} | \Phi_i(k\Delta\tau/2) \rangle$ and $n_{\beta/2} = \beta/2\Delta\tau$; each O_i is the expectation value of the observable on the QITE-evolved state $|\Phi_i(\beta/2)\rangle$. Note that here both the exact imaginary-time-evolved state $|\Phi_i(\beta/2)\rangle$ and the QITE-evolved state $|\Psi_i(\beta/2)\rangle$ are consistent with the definitions in 5.2.

In full trace evaluation O is regarded a function of the P_i and O_i, which are random variables because of measurement sampling on quantum computers. $\mathrm{Var}(O)$ can be evaluated by expanding O to first order in all P_i and O_i and assuming all P_i and O_i are independent, which then gives

$$\mathrm{Var}(O) = \frac{\sum_{i=1}^{2^N} [\mathrm{E}(P_i)^2 \mathrm{Var}(O_i) + (\mathrm{E}(O_i) - \mathrm{E}(O))^2 \, \mathrm{Var}(P_i)]}{\left(\sum_{i=1}^{2^N} \mathrm{E}(P_i) \right)^2} \tag{B.2}$$

In stochastic trace evaluation, we need to consider initial state sampling on top of measurement sampling. Define the numerator $R = n_{\text{samples}}^{-1} \sum_{i=1}^{n_{\text{samples}}} P_i O_i$ and the denominator $S = n_{\text{samples}}^{-1} \sum_{i=1}^{n_{\text{samples}}} P_i$ so that $O = R/S$. By first-order expansion of O in R and S and assuming R and S are independent,

$$\mathrm{Var}(O) = \frac{\mathrm{E}(R)^2 \mathrm{Var}(S) + \mathrm{E}(S)^2 \mathrm{Var}(R)}{\mathrm{E}(S)^4}. \tag{B.3}$$

Now expanding R and S to first order in all variables and assuming all variables are independent, we have

$$\begin{aligned}\mathrm{Var}(R) = \frac{1}{n_{\text{samples}}^2} \sum_{i=1}^{n_{\text{samples}}} &[(\mathrm{E}(P_i)\mathrm{E}(O_i) - \mathrm{E}(R))^2 + \\ &+ \mathrm{E}(P_i)^2\mathrm{Var}(O_i) + \mathrm{E}(O_i)^2\mathrm{Var}(P_i)], \end{aligned} \tag{B.4}$$

$$\mathrm{Var}(S) = \frac{1}{n_{\text{samples}}^2} \sum_{i=1}^{n_{\text{samples}}} [(\mathrm{E}(P_i) - \mathrm{E}(S))^2 + \mathrm{Var}(P_i)]. \tag{B.5}$$